**Republic of Iraq**
**Ministry of Higher Education and Scientific Research**
**University of Babylon - College of Science For Women**
**Dep. of Laser Physics**

# Thermo-Plasmonic Properties of Hybrid Nanostructures

A Thesis

Submitted to the College of Science for Women at the

University of Babylon in Partial Fulfillment of the Requirements for the

degree of Master Science in Laser Physics

By:

**Nada Abbas Mohammed**

Supervised by:

**Prof. Dr. Wajeha Abdl Daim** **Dr. Ahmed Kadem Kodeary**

2022 A.D 1444 A.H


آية الكرسي سورة البقرة آية ٢٥٥

# DEDICATION

TO...

MY DEAR FAMILY; FATHER,

MOTHER,

SISTER & BROTHERS

MY DEAR HUSBAND,

AND MY SONS

TO MY TEACHERS...

WHO PROVIDE ME WITH THE KEYS TO SUCCESS

MY BELOVED COUNTRY IRAQ...

THE MARTYRS OF IRAQ...

WITH ALL THE LOVE AND APPRECIATION

NADA

# ACKNOWLEDGMENTS

Thankfulness, praise be to Allah, the grace that befits his holy self, and peace and blessings be upon our Messenger, Muhammad Bin Abd Allah, May Allah's prayers and peace be upon him and his family and companions After completing this work, it is my pleasure to extend my sincere thanks and appreciation to the owners of the generous hands, who contributed with their abundance knowledge, their valuable time and their sincere help in helping me to traduce this research, Professor Dr. Wjeha , Dr. Ahmed and Dr. Maher Thanks to the Deanery of the College of science for women / University of Babylon and the Department of laser Physics for offering me the opportunity to complete my research. I also would like to express my thanks to all teachers, instructors and students of the Department of laser Physics for their assistance. Many thanks go to those who support me and alleviate difficulties I have faced during my experimental work, and to everyone who helped me in a way or another during my preparation of this thesis. Apologize for whom I miss mentioning. I wish success to all.

**NADA**

# Abstract

The present experimental study focused to synthesize and evaluate the thermo-plasmonic properties based on the core/shell nanoparticles and the core/multi-shell nanoparticles prepared by laser ablation in liquids with nanosecond laser pulses at 1064 nm, to introduce a new type of hybrid nanostructures usable in biomedicine and optical photonics applications. For these hybrid nanostructures, Gold (Au) and Silver (Ag) as a partner of Silicon (Si) were used in thermo-plasmonic part, the hybrid multi-shell nanostructures consist of gold-silver and silver-gold sandwich with silicon shell in between.

The optical absorption was measured using a UV–Vis spectrophotometer for the samples, and the intensity and position of the plasmon were monitored depending on the dielectric properties of the samples. In addition, the thermo-plasmonic properties are studied by monitoring the local temperature increase of the samples experimentally by infrared camera, when the samples are illuminated by lasers of different wavelengths (532, 405 nm). As well as the core/multi-shell NPs were tested to inhibit the activity of the E-coli bacteria under laser radiation.

In addition, the optical properties, the thermo-plasmonic effect, and the surface electric-field distribution of the samples are investigated theoretically with different core size and different shell thickness by the

finite element method of the COMSOL multi-physics program under laser irradiation with different wavelengths (532, 405 nm).

The results revealed to a clear tunable and adjustable optical and thermo-plasmonic properties by controlling the structure of the core/shell NPs.

In addition, the results show that not only an extreme tunability in the surface plasmon resonances can be obtained, but also considerably enhanced photo-thermal effects in terms of temperature rise, that depends on the laser effect. The results show that the core/multi-shell samples produce more heat than the core/shell NPs samples, and also more heat than the individual samples. The temperature elevation was 8.2C$^{o}$ for the Ag@Si@Au NPs and 7.4C$^{o}$ for the Au@Si@Ag NPs under C.W laser illumination (405, 532 nm), respectively.

In addition, the experiments proved that the proposed nano-system achieved a high killing efficiency against the E-coli bacteria under a CW laser illumination (405,532nm), the diameter of the inhibition zones was 8 and 6 mm for the Au@Si@Ag NPs and the Ag@Si@Au NPs samples, respectively.

The simulation results indicated a considerable relationship between the present computational and experimental results, the results can be enhanced depending on the size, shape, structure, and surrounding media.

Moreover, the COMSOL multi-physics program can predict the experimental results exactly. Accordingly, the results show the possibility of using the core/multi-shell nanoparticles as efficient heat sources in many applications, especially in the disinfection and sterilization of medical equipment.

# List of Figures

# List of Tables

## List of Abbreviations

| Abbreviations | Descriptions |
|---|---|
| C/M-S | Core/Multi-Shell |
| C/S NPs | Core/Shell Nanoparticles |
| CW | Continuous Wave |
| DIZ | Diameter of the Inhibition Zones |
| EM | Electromagnetic Wave |
| FE-SEM | Field Emission Scanning Electron Microscopy |
| fs | Femtosecond |
| FTIR | Fourier Transform Infrared Spectrometer |
| IR | Infrared |
| LAL | Laser Ablation in Liquid |
| LSP | Localized Surface Plasmon |
| M/M | Metal- Metal Contact |
| M/S | Metal/Semiconductor |
| M/S/M | Metallic/Semiconductor/Metallic |
| NPs | Nanoparticles |
| ns | Nanosecond |
| Ps | Picosecond |
| SEM | Scanning Electron Microscopy |
| SPP | Surface Plasmon Polariton |
| SPR | Surface Plasmon Resonance |
| TEM | Transmission Electron Microscopy |
| UV | Ultra-Violet |
| MHA | Mueller Hinton Agar |
| FEA | Finite Element Analysis |
| FDM | Frequency Domain Method |

## Chemical Elements

| Abbreviations | Description |
|---|---|
| Ag | Silver |
| AI | Aluminum |
| Au | Gold |
| Cu | Copper |
| $Cu_2Se$ | Copper selenide |
| Mg | Magnesium |
| Pd | Palladium |
| Pt | Platinum |
| PVA | Poly vinyl alcohol |
| PVP | Poly vinyl pyrrolidone |
| PZT | Lead Zirconate Titanate |
| Si | Silicon |
| $SiO_2$ | Silica |
| ZnO | Zinc Oxide |

## List of Symbols

| Symbol | Description | Unit |
|---|---|---|
| $\epsilon(w)$ | The metal's dielectric function | *F/m* |
| $\epsilon_d$ | The dielectric function of the surrounding. | *F/m* |
| $Q_{(r,t)}$ | Heat Power | *Watt/m²* |
| $\emptyset$ | The work function | *eV* |
| $\mu_0$ | Free space permeability | *H/m* |
| $\sigma_{acs}$ | Absorption cross section | $m^2$ |
| $t$ | The sample thickness | *M* |

| Symbol | Description | Unit |
|---|---|---|
| $I_T$ | The transmitted intensity beams | $w/m^2$ |
| $\tau$ | Electron characteristic time | *ns* |
| $\omega$ | Angular frequency | *Hz* |
| $\epsilon_0$ | Free space permittivity | *F/m* |
| $\epsilon$ | Molar absorption coefficient | $M^{-1}\ cm^{-1}$ |
| $\varepsilon$ | The dielectric constant | *F/m* |
| $\varepsilon_1$ | The real part of the dielectric | *F/m* |
| $\varepsilon_2$ | The imaginary part of the dielectric constant | *F/m* |
| $\epsilon_d$ | The dielectric constant of surrounding medium | *F/m* |
| $l$ | Optical length | *M* |
| $k$ | Wave number | $m^{-1}$ |
| $k_{med}$ | Thermal conductivity of medium | *W/m.K* |
| *C* | Molar concentration of the absorber substance | *M* |
| C | Speed of light | *m/sec* |
| *D* | Dielectric displacement | $C/m^2$ |
| *E* | Electric field | *V/m* |
| $E_{VAC}$ | Energy of the vacuum level | *eV* |
| *J* | Total current density | $A/m^2$ |
| *K* | Extinction coefficient | --- |
| $\emptyset_M$ | The metal work function | *eV* |
| $m_e$ | Electron mass | *Kg* |
| $\gamma$ | electron damping factor. | |
| *N* | Number of electrons | *electron.* |

| Symbol | Description | Unit |
|---|---|---|
| $P$ | Electric Polarization | $C/m^2$ |
| $Pa$ | Polarizability | $C.m^2/V$ |
| $q_e$ | Electron charge | *Coulomb* |
| $\tau$ | The typical duration of transient regime | *Sec* |
| $\emptyset_{Semi}$ | The semiconductor work function | *eV* |
| $w_p$ | Plasma frequency | *Hz* |
| $X$ | The electron displacement | |
| $\alpha$ | The Absorption coefficient | $m^{-1}$ |
| $E$ | The dielectric constant or absolute permittivity | *F/m* |
| n | Refractive Index | --- |
| $\bar{n}$ | The complex refractive index | --- |
| $\lambda$ | Wavelength | *nm* |
| $I$ | Intensity of the transmittance ray through the sample | $W/m^2$ |
| $I_0$ | Intensity of incident ray | $W/m^2$ |
| $\boldsymbol{c_p}$ | The material specific heat | J/ Kg.C$^o$ |
| $r$ | Distance from center of nanoparticle | *m* |
| $R$ | Radius of nanoparticle | *m* |
| $A$ | Absorbance | ---- |
| $V$ | Volume of nanoparticle | $m^3$ |
| $T^{cw}$ | Heat generation due to CW laser irradiation | *K* |
| $T^{pulsed}$ | Heat generation due to pulsed laser irradiation | *K* |
| $\boldsymbol{\rho}$ | The material density | $g/m^3$ |
| $\boldsymbol{\rho}_p$ | Density and of the particle | $g/m^3$ |

| Symbol | Description | Unit |
|---|---|---|
| $\phi_{(KR)}$ | The function represent the radiative decay | |
| $P_{av}^{1}$ | Equivalent polarizability | |
| $R_2$ | Radius of external layer | *M* |
| $q_i$ | Internal wave number | |
| $q_e$ | External wave number | |
| $a_l$ and $b_l$ | The Mie scattering coefficients | |
| $P_{(r,t)}$ | The optical dissipation in NP per unit volume | *Watt/m*$^3$ |

# Chapter One
# Introduction

## 1.1 Introduction

Over the last decade, there have been an increasing interest by researchers in use of plasmonic nanomaterials as effective sources of heat remotely controlled by light named as thermo-plasmonic materials. Thermo-plasmonic is a field of study involving the light-triggered local temperature rise of plasmonic materials (also called "photo-thermal" heating) [1]. Plasmonic nanoparticles (NPs) play a substantial role in this field of research of thermo-plasmonics due to their optical, electronic, thermal, and catalytic properties and also have aroused keen interest due to the distinguished feature of surface plasmon resonance (SPR), which is characterized by plasmonic metal nanoparticles only [2]. The SPR is a collective oscillation of conduction electrons possessed by metal nanoparticles, which is excited by an electromagnetic field at special wavelengths [3]. This field has been widely exploited for a large number of applications, including biomedical sensors [4,5], photo-thermal imaging[6], drug delivery [7], cancer thermotherapy [8,9], disinfection and sterilization [10], etc. In the Fig (1-1), it show some of the basics and applications of the thermo-plasmonics technology.

Despite considerable progress in the techniques of synthesis of nanomaterials and their use in several fields, especially the medical field, a great deal remains to be understood about the fundamentals of thermo-plasmonic nanomaterials, in particular the physiological and biological mechanisms they trigger. The plasmonic nanoparticles are used for their high ability to boost a local temperature based on the optical heating with optical nearfield enhancement and hot-carrier injection [11].

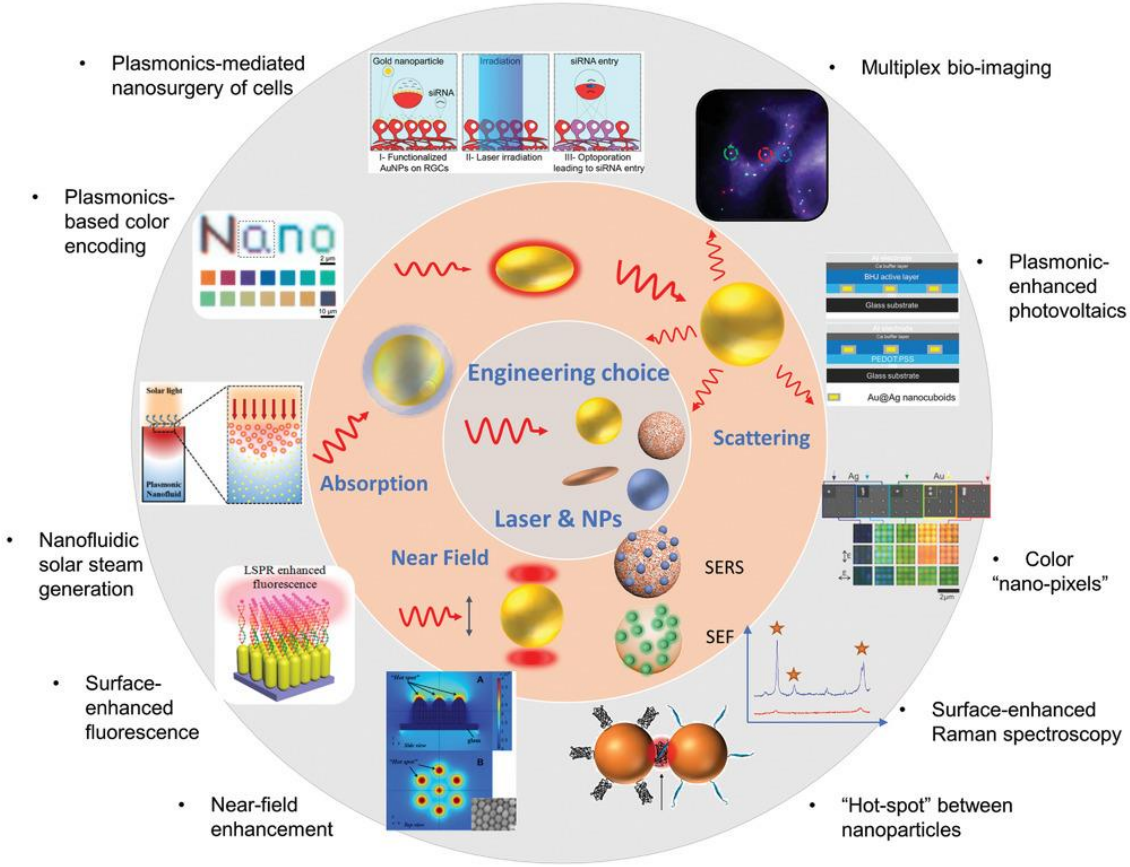


***Fig (1-1) the Schematic representation form of some applications of the thermo-plasmonics [12].***

Thermo-plasmonics represents a significant research area with pivotal, economic, and societal impact that could contribute to the development of the medical nano-field. In particular, hot-electron injection involves plasmonic metal electrons by laser, and it has the ability to raise the temperature which could not happen otherwise through conventional heating [13]. Therefore, with the use of plasmonic nanoparticles as effective light absorbers, this approach provides key features compared with conventional heating. One of these features is that the heating laser provides reduced spatial scale to enable heating over a micrometric area, this allows the heat to not spread to the surrounding areas. Also, the plasmonic heating may produce a high temperature rise with moderate lighting. Pulsed and continuous laser light brings the NPs to a

superheated state. Moreover, the advantage of plasmonic NPs, when sized down to a few nano-metres, it can also feature effective catalytic activity [13]. Furthermore, previous research of the thermo-plasmonic effects has primarily focused on bare noble metals such as Au and Ag NPs in a variety of morphologies such as spherical, ellipsoids, rods, disks, rings, and stars, among others [14-19].

The most famous materials that have the plasmonic property are the noble metals (Au, Ag, Cu, and Pt NPs), and also there are other materials in which the SPR property appears, but most materials are exhibit localized plasmon resonances in the UV range, shown in the Fig (1-2) [20,21].

Since the absorption by the bare noble metal leads to the dissipation of light into resistive thermal energy, optically excited noble Metal/Semiconductor (M/S) core/shell NPs can thereby be exploited as efficient heat sources in a set of applications instead of the bare noble metal in the field of thermo-plasmonics [22]. Therefore, core/shell nanoparticles (C/S NPs) are good candidates for this application [23].

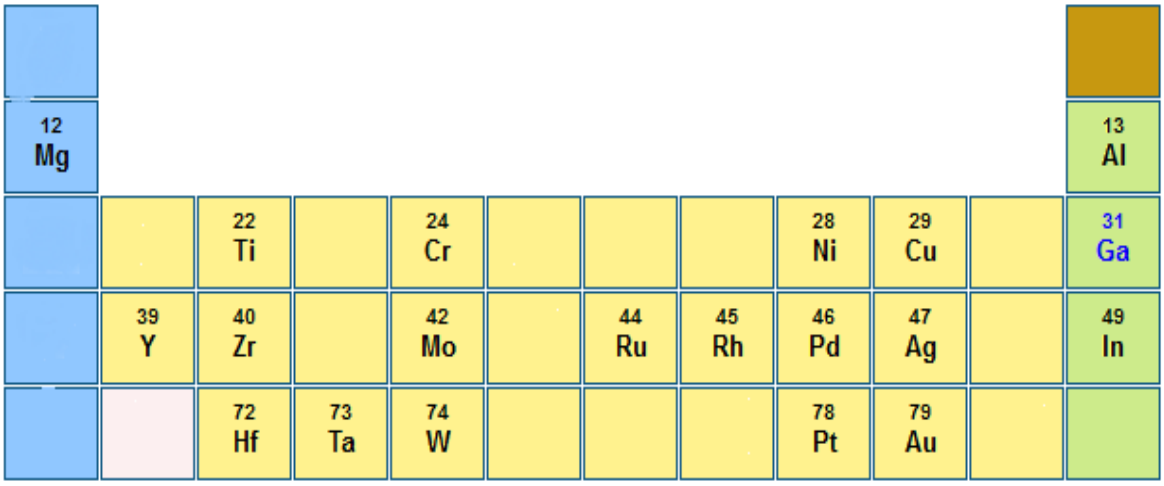


***Fig (1-2) Representation of the elements considering as the plasmonic materials [20,21].***

The core/shell plasmonic nanoparticles have a highly geometrically tunable optical resonance. This in turn gives controllability of the refractive index and the dielectric properties of the nanomaterial [22]. The concentric incorporation of either a spherical gold NPs or silver NPs as a core into the silicone NPs as a shell, followed by the plasmonic NPs coating as the next shell, leads to different plasmonic behaviors and optimized photo-thermal properties of the nanostructure. There has been a lot of experimental work on metal/silica NPs in various applications, but there is still a need to discover the tunable photo-thermal properties of the C/S nanostructures and the role of the shell in the photo-thermal response, which deserves more attention. The plasmonic properties for the C/S NPs are mostly linked to the interaction between the size of the core and the thickness of the shell. The plasmonic coupling strength can be determined by the core size and the shell thickness. Whilst, the plasmon coupling strength makes them efficient for light-to-heat conversion by using the metal/silicon C/S nano-plasmonics when the wavelength shift plasmon band is in the IR-region. Thus, the development of IR-region plasmonic materials still has many challenges [24].

This work have reported enhanced in the properties of thermo-plasmonic for the Core/Multi-Shell (C/M-S) hybrid nanostructures at the visible region , which has the ability to be used in biomedical applications as an effective anti-bacterial. In such a hybrid system, Au/Si/Ag have characteristic plasmon absorption from the UV to NIR spectral region, whereas noble bare metals have narrow wavelength plasmonic absorption. This allows the use of lasers of different wavelengths to irritate the thermo-plasmonic. This work will provide useful information about the thermo-plasmonic properties of the C/S NPs based on

metallic/silicone and the optimal use of the plasmonic NPs for thermo-plasmonic bio-medical applications based on heating.

## 1.2 Literature Survey

The research work in thermo-plasmonic has been investigated for a few years ago. Therefore, the Au, Ag thin films and Au, Ag NPs have been widely studied in recent years [25,26]. However, there are reports on the C/S nanostructures, it is well known that the thermo-plasmonic properties of the C/S nanostructures are different from those of their thin films and NPs counterparts because their characteristics are affected by other factors [27]. According to, the previous literature are reports about the metals/semiconductor C/M-S nanostructures to what was rare to our knowledge. However, there is highly needed for more research due to its importance for the metals/semiconductor C/S nanostructures in different fields of application especially in the medical field. In the following, the most important works for the last ten years are presented.

**In 2013, A. L. Lereu, et al [28],** synthesized the gold nano-islands and the gold thin film with a thickness (57.4 nm) on a quartz prism substrate by the electron beam evaporation method. Their results showed more thermal response and high localized confinement of the Au nano-islands, than compared with gold thin film. They also proved that the temperature elevation depends on the dielectric constant of the materials.

**In 2014, Han Dai, et al [29],** studied Ag NPs with different size (30, 50, and150 nm) deposited on the Si substrate by sputtering annealing method ,the sizes of Ag NPs are controlled by changing sputter current. Their results showed a blue shift of the SPR position, and also a Red shift of the SPR When the annealing temperature changes from 323K to 343 K of the

Si substrate. Their results proved, the thermal effects of morphological change and the damping effects of Ag NPs was small effects.

**In 2014, Qiang Li, et al [30],** studied the photo-thermal characteristic of the C/S NPs by COMSOL Multiphysics program for different compositions (30 Au@10 SiO2 nm), (50 $SiO_2$@7.5 Au nm), and (30 Au@10 $SiO_2$@10 Au nm) irradiated with 540, 830, and 900 nm respectively. Their results showed tunable in the SPR and improving photo-thermal effect, so compositions used more than with the bare Au NPs, also noted that the C/S NPs have high tunable optical resonance and photo-thermal effect by changing the thickness of the shell.

**In 2016, Stephen J. Norton, et al [31],** designed the nano-spheres, nano-spheroids, and nano-stars from the gold NPs as heat sources in fluid. They studied the absorption cross section of these Au NPs, and also calculate heat-flow equation to determine the constant state of the temperature height and the time to reach the constant state. They recommended using the nano-spheroids or the nano-stars for photo-thermal treatment due to the plasmon resonance of these Au NPs lies within the medical windows for the soft tissues transparence at this range of electromagnetic waves.

**In 2017, Lijun Meng, et al [32],** designed and studied thermo-plasmonic a C/M-S based on gold/silica or aluminum/silica multi-shells alternately. The results showed the capable of achieving high temperatures in the core region using moderate illumination intensities, a huge electric field enhancement. In addition to a large optical intensity enhancement of over a relatively broad core region with a simple design consisting of three metal layers.

**In 2018, Maher Abdulfadhil Gatea, et al [33],** prepared Au@$SiO_2$ C/S NPs that flooded in water and PVP using laser ablation in liquid method. They used the theoretical simulation by COMSOL program by irradiating samples of the 532 nm CW laser and the 520 nm fs pulse laser, they founded that the fs pulsed laser caused higher temperature elevation despite the low power used and the temperature elevation in water is higher than that in PVP because the higher thermal conductivity of water than PVP.

**In 2018, Soomin Han, et al [34],** studied heating the compound of the Au@cellulose NPs by laser in water, and also studied efficacy as an antibacterial against E. coli. The temperature at the surface of the compound has increased during Irradiated with NIR laser. Their results proved that the proposed compound can be used to kill E. coli and also sterilization and desalination the water.

**In 2019, Maher Abdulfadhil Gatea, et al [35],** designed the Au@SiO2 NPs in water and PVP theoretically by COMSOL program, which was different in the relative volume fraction of the core and the shell. The results showed the temperature of the samples increase with the core radius increased. Conversely, the temperature decrease with the increase of the thickness of the shell at fixed core radius (20 nm).

**In 2019, Marta Quintanilla, et al [36],** synthesized the Bi-metallic Au@Pd NPs by chemical process, this form shows efficient photo-thermal effects and rising in the thermal stability for a solution, The heating efficiencies around (40%_60%), and also noticed that the minimal Au@Pd NPs have the highest efficiencies, the proportion between extinction and absorption highly relies on the amount and location of Pd NPs.

**In 2020, Ali Alkurdi, et al [37],** studied the Au@$SiO_2$ C/S NPs in water by computer model. They studied the energy transfer between the core and the shell. They found the heat transfer faster than from gold NPs when the thickness of the silica of fine shell also when using a pulsed laser compared to a continuous laser.

**In 2020, A. K. Kodeary, et al [38],** synthesized and studied thermo-plasmonic of the Au@PZT NPs C/S NPs in an aqueous colloidal dispersions. The results showed that the temperature elevation is about 3.7-14.1$C^o$ under laser illumination and electric field.

**In 2021, Haitao Wang and Ming Li [39],** designed the two kinds of concentric multi shell NPs, the hetero NPs (Au@$SiO_2$@$Cu_2Se$) and the homo NPs ($Cu_2Se$@$SiO_2$@$Cu_2Se$) theoretically by COMSOL program. They studied the photo-thermal characteristics and the enhancing in the temperature distribution for these two kinds under Infrared irradiation extending from 1000 to 1700 nm.

**In 2022, M. Jazmin Penelas, et al [40],** synthesized the Au@$SiO_2$ NPs in an aqueous colloidal dispersions that have photo-thermal activity for a range of the wavelengths. The results showed that the characteristics of the shell control both, the photo-thermal effect and the optical properties of the colloidal dispersions. As well as the photo-thermal properties of NPs depended on a thicknesses of silica shells.

## 1.3 Aim of the Work and the Research Motivation

This work aims to synthesize a new plasmonic nanostructures of the C/M-S NPs as a nano-heat source controllable by external or internal parameters, such as the applied lasers or the plasmon position manipulation to use in the optical and biomedical area. Thus the ultimate aim of the study is to gain deep insight onto the physical mechanism of change in the properties and understand the optimum functional behavior of these materials.

In addition, to understand the physical processes at their metal/semiconductor interfaces to improve understanding and performance of novel nano-thermal devices.

# Chapter Two Theoretical Part and Basic Concepts

## 2.1 Introduction

Recently, the researchers have realized that mixing nanomaterials has different properties which opens up a new field set of applications in nanotechnology, the researchers have trapped their attention on finding novel nanocomposites and nanostructures can be controlled when they are irradiated by the laser or the directly affected of the external electromagnetic fields, or affected by mechanical pressure. Accordingly, a large number of studies have focused on noble metal NPs such as Au, Ag, Cu, and Pt due to their plasmonic properties [41,42]. Further, a new hybrid NPs were made by combining these plasmonic metals with semi-plasmonic materials or semiconductor materials such as AI, Mg, ZnO, and $SiO_2$ [43-46].

Furthermore, the interaction between hybrid nanostructures components can change the metal electronic states which are various from the states of the constituent metals. In fact, this adjusting and tuning properties are essential for getting broad applications in bio-sensing, diagnostics and therapeutics, and high-contrast imaging [47], as well as contributing to the development nano-photonic devices [48].

On the other hand, tuning and adjusting the plasmonic and the optical properties of nanostructures, based on understanding interfacial phenomena between the core and the shell in nano-systems.

## 2.2 Nanostructure

Rapidly growth of the nanotechnology is related to infinite applications of devices, systems and structures, by controlling size, shape and structure at nanometer scale [49]. The field of nanotechnology started at 1959 when Richard P. Feynman presented his famous lecture ‘‘There’s Plenty of Room at the Bottom” [50]. The Greek term (nano) means "dwarf" refer to “very small” and denoted as universal unit (SI unit) of

sample "n" as a factor of $10^{-9}$ [51]. Materials at this scale provide many advantages, depending upon the size, shape, structure and method of preparation [52].

Nanotechnology is the understanding and control matter at dimensions of roughly 1–100 nm. At the nanoscale, the properties like electrical conductivity and mechanical strength are not the same as the materials with particles in dimensions much more than 100 nm. The electronic structure changes dramatically too [53].

The particles of different types and materials at the range between 1 to 100 nm can be classified according to agglomeration of atoms and molecules as shown in Fig (2-1) into [54];

**Zero dimensional nanoparticles:** these nanoparticles have all the three direction length in the nanometer scale. The zero dimensional NPs are isolated from each other such as nanocluster materials, metal particles (Au, Ag NPs) or semiconductor (quantum dots) particles [55].

**One dimensional nanoparticle**: these nanoparticles have only one direction length out of the nanometer range including nanorods, nanowires, and nanotubes.

**Two dimensional nanoparticles:** these nanoparticles have two direction out of the nanometer range, including nanofilms, coating surface, and nanosheets.

Agglomerate state of NPs occurs over short distances due to van der Waals force; this the agglomeration affects the chemical and the electromagnetic properties of NPs [56]. The agglomeration process depends on the type of NPs, conditions of synthesis method and concentration of NPs in solvent. The agglomeration process can be avoided by several processes such as coating the nanoparticle surface by another organic or inorganic substance or chemically stabilization by polishing slurries in aqueous suspension [57].

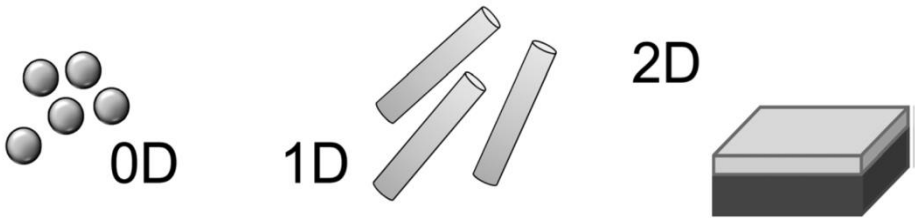


***Fig (2-1) Nanoparticles classified according to their directions [55].***

The high development in NPs s synthesis techniques enables to synthesis different types of NPs such as spherical NPs [58], cube NPs[59], disk NPs[60], wire NPs[61], tube NPs[62], rod NPs[63], prism NPs[64], star NPs[65]. The NPs have larger enhancement of physical and chemical properties compared to bulk material due to their extremely large surface area to volume ratio [66].

The NPs characteristics (physical and chemical properties) are based on the size, shape, structure, physical stability, and distribution of the NPs, which can be investigated using different microscopic technique such as the scanning electron microscopy (SEM), the transmission electron microscopy (TEM) [67]. Various technologies or methods are used to prepare nanostructured materials such as: electro-deposition method [68], Chemical Vapor Deposition method [69], Sol-gel methods [70], Self-Assembly Method [71], Laser ablation method [72], etc.

### 2.2.1 Core/shell Nanoparticles

Nowadays, the researchers have focused their attention in nanotechnology field on finding novel nanostructures in order to achieve novel physical and chemical properties. The C/S NPs as the combination of two different materials in one nano-metric system are considered as

one of these nanostructures which can give novel and fantastic properties. The nanostructures can be classified based on single or multiple materials into simple and composite NPs. A simple nanostructures are made from a single material. Whereas, a composite nanostructures are composed of two or more materials such as C/S NPs [73].

The C/S NPs type are defined as concentric core (inner material) and a coating shell (outer layer material). The C/S NPs can be categorized based on inner and outer material into organic-organic, inorganic-inorganic, organic- inorganic, inorganic-organic materials, Depending on the application, the shell material, the shape and/or structure of NPs could be chosen; Fig(2-2) shows different structure types of the C/S NPs [74].

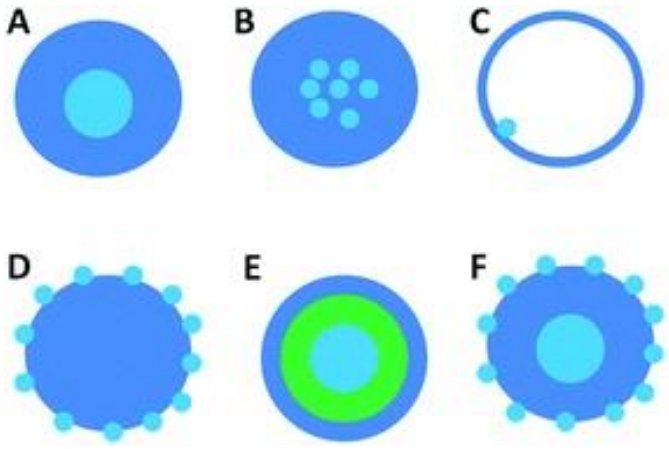


***Fig (2-2) Schematic describing different types of the C/S NPs [74].***

Modified properties of the C/S NPs can be obtained by either changing the volume ratio of the core part to the shell part or changing the composite materials, such as thermal stability, reactivity and dispersibility of the core. The main purpose of the core part coating is to fold the surface modifications, stability and dispersibility to control the functionality of the core [75]. The C/S NPs are widely used in many applications such as control drug delivery [76], photo-thermal cancer

therapy[77],optoelectronics[78],catalysis[79],photoluminescence[80],bio-imaging [81], etc.

## 2.3 Interface between Two Materials

Formation of electronic devices requires putting together two or more dissimilar materials (semiconductors, metals, insulators). The interface between these materials becomes crucial because it affects the electrical properties (transport) of the devices [82]. This interface is called the junction [83]. An ideal junction is one where there are no defects formed at the interface [84]. Forming ideal junctions is challenging and most real materials have defects at the interface which can affect the electronic properties [85]. But can get an idea of the interaction between materials by studying interfaces.

### 2.3.1 Metal/Metal Junction

Metals are characterized by an incomplete energy band (valence and conduction band overlap) with the top of the energy band being the Fermi energy. The distance from the Fermi level to the vacuum level is called the work function (Ø) [82-85].

We know that the work function is very important to describe the transmission of electrons between metal surfaces, the work function locates the bulk chemical potential relative to the vacuum reference level[83].

Overall, the work functions are calculation to determine the effective number of valence electrons. This allows the hardness of the atoms to be calculated which is, in turn, allowing for a covalence induced surface effects predictions of the work functions for metal surfaces [83].

At metal surfaces negative dipoles arise from the spreading effect as surface electrons “spread” out into the vacuum. Positive dipoles form as

electrons flow into low open spaces on atomically rough surfaces. Where it is allowed for both kinds of dipoles and strong correlation between bulk and atomic properties was argued to imply near perfect cancellation to minimize the total surface energy [84].

The work function may then be taken as a good estimate of the bulk chemical potential of the metal relative to the vacuum level.

$$\phi_M = E_{VAC} - E_F \qquad (2.1)$$

where $\emptyset_M$: the metal work function, $E_F$ :Fermi level.

Consider a junction formed between two metals with different work functions, as shown in Fig (2-3). As an example, the two metals are Au and Ag with work functions of 5.10 and 4.26 eV respectively [86].

The most important rule when a junction is formed is that the Fermi levels must line up at equilibrium (no external bias). This can be understood by using Fig (2-3a), where there are electrons in Ag at a higher energy level than those in Au. These electrons can occupy the empty energy levels located above the Au Fermi level. Because electrons move from Ag to Au a net positive charge develops on the Ag side and a net negative charge on the Au side. Thus, a contact potential is developed at equilibrium between the two metals. This contact potential is related to the difference in the work functions, and is shown in Fig (2-3b). For Ag-Au junction the contact potential is 0.84 eV [86].

The Ag has a smaller work function than the Au. When a junction is formed electrons from the Ag move to the Au until the Fermi level lines up and the junction is in equilibrium [86].

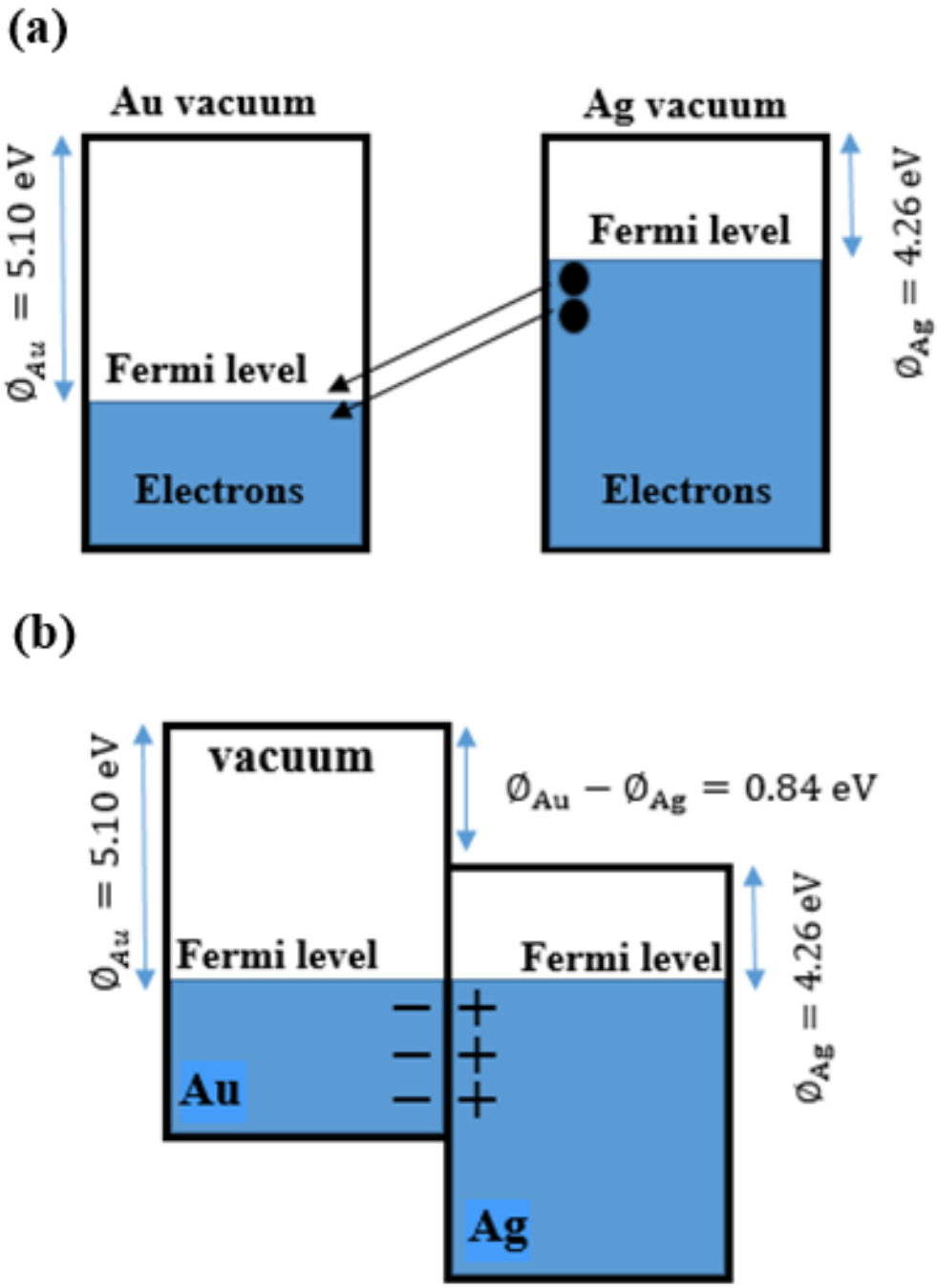


***Fig (2-3) the Junction between Au and Ag, a) before equilibrium, b) at equilibrium, with a contact potential given by the difference between the work functions. The contact potential prevents further motion of electrons from Au to Ag.***

### 2.3.2 Metal/Semiconductor Junction

When a metal and semiconductor are brought into contact, there are two types of junctions formed depending on the work function of the semiconductor and its relation with the metal [87]:-

**a. Schottky junction** $\emptyset_M < \emptyset_{semi}$

**b. Ohmic junction** $\emptyset_M > \emptyset_{semi}$

Consider a junction formed between a metal and semiconductor, the Fermi level of the semiconductor is higher than the metal [87]. Similar to a metal-metal junction, when the metal/semiconductor junction is formed the Fermi levels must line up at equilibrium [88]. The electrons in the conduction level of the semiconductor which can move to the empty energy states above the Fermi level of the metal, this leave a positive charge on the semiconductor side and due to the excess electrons, a negative charge on the metal side, leading to a contact potential [89]. When a contact is formed between two metals, the charges reside on the surface, this is due to the high electron density found in metals. On the other hand, when a contact is formed between a metal and semiconductor, due to the low charge density on the semiconductor side the electrons are removed not only from the surface but also from a certain depth within the semiconductor. This leads to the formation of a depletion region within the semiconductor. Thus, when a Schottky junction is formed between the metal and semiconductor, the Fermi level lines up and also a positive potential is formed on the semiconductor side. Because the depletion region extends within a certain depth in the semiconductor there is bending of the energy bands on the semiconductor side. Bands bend up in the direction of the electric field (field goes from positive charge to negative charge) [90].

This means the energy bands bend up going from semiconductor to metal. The Fermi levels line up and there is a certain region in the

semiconductor [89,90], where the bands bend this is called the depletion region. This is given by the difference in work functions, this is illustrated in Fig (2-4), in relation to Schottky junction and Fig (2-5), in relation to Ohmic junction [89].

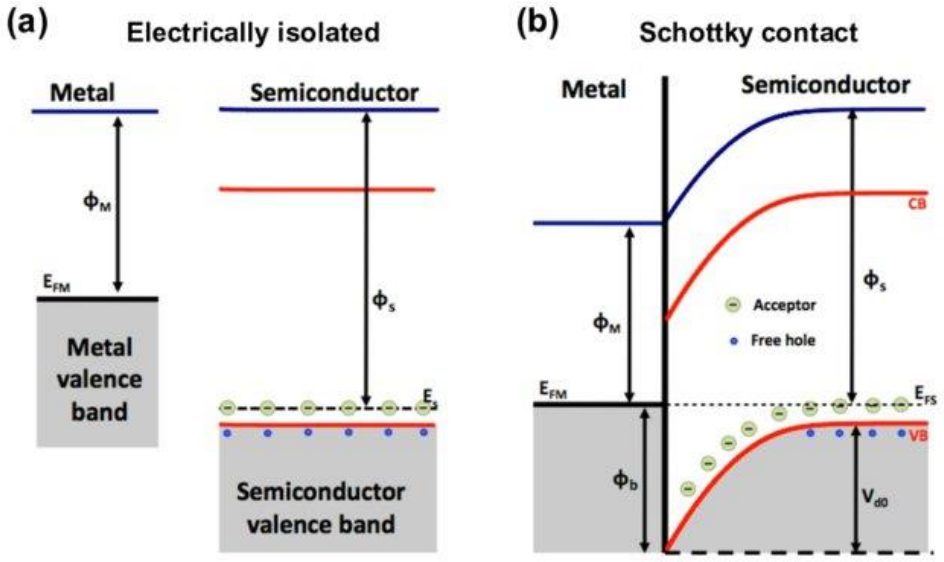


***Fig (2-4) the band structure of metal/ semiconductor Schottky junction at thermal equilibrium; (a) electrically isolated and semiconductor, and (b) the band alignment at thermal equilibrium [89].***

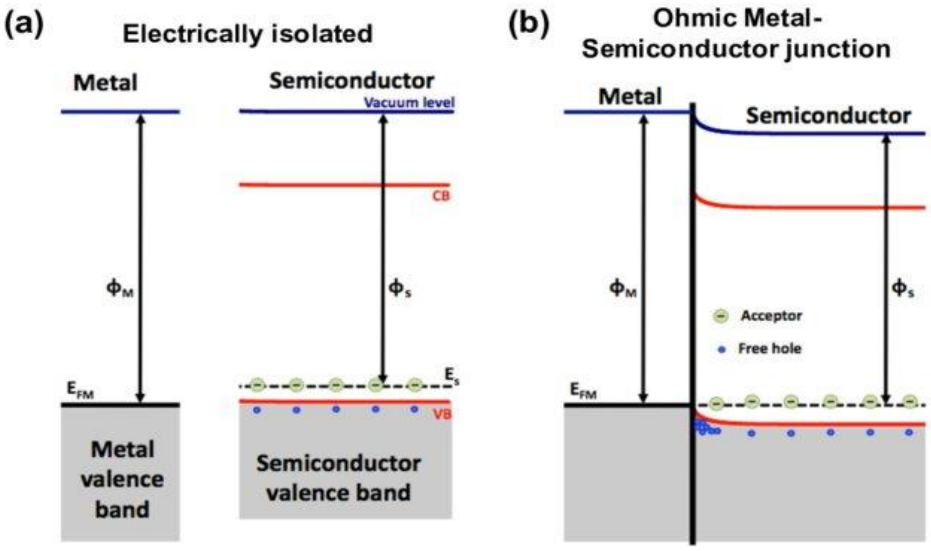


***Fig (2-5) the band structure of the ohmic metal/semiconductor junction at thermal equilibrium; (a) Isolated metal and semiconcutor, (b) The band alignment at thermal equilibrium [89].***

As for a M/S interface, the static polarization charges at the interface arising from thermo-electric effects can then be modulated the height of the Schottky barrier by the applied fielld, resulting in tuning of the barrier electronic-transport properties by the external effects [89].

By utilizing the thermo-plasmonic charges to redistribute the charge carriers inside the semiconductor and modulate the energy band at local contact or junction, the transport behavior of the electric process of the free carriers can be modulated/tuned, which is referred to as the effect [91], which involves using thermo-electric polarization charges as a "gating" voltage for tuning the electronic transport across an interface or junction[92].

Hence, the electron transport is effectively manipulated by thermo-plasmonic effect [93]. When photons whose energy surpasses the bandgap of the semiconductors irradiate on the M/S contact, photoinduced carriers are created at the interface of the contact. The carriers are divided and gathered with the help of Schottky junction. The lower barrier can enhance electron transport, while an increased barrier height can cut off the current, just like a diode [93].

## 2.4 Plasmonic

Plasmonics is the field of study the optical phenomena that results from interaction of conduction free electrons of noble metal nanoparticles with electromagnetic waves (especially at visible optical frequencies) and collective oscillation called as surface plasmon [94].

Plasmonic is a major part of the nano-photonics which can confine electromagnetic waves smaller than the diffraction limit. The development of nanofabrication techniques helps to increase applications of plasmonic nanostructures [95]. When electromagnetic waves are

incident on a metal surface, it will accelerate electrons and lead to induce polarization that creates restoring force which causes an oscillation of the free electron of the metal. This oscillation is quantized and free electrons oscillation is quantization of plasma oscillations and it's called a plasmon[96].

There are two types of surface plasmon according to their interface: Surface Plasmon Polariton (SPP) and localized surface plasmon (LSP).

The SPP are longitudinal waves, which propagate at the interface between a dielectric and metal. These waves travel parallel to the direction of propagation; so they cannot be excited by a transverse waves [97,98]. The most effective way to excite a plasmon is to use electrons i.e. when light excites the electrons, electrons will pass through a thin metal layer and lose some energy, this loss in energy use to excite the SPP[99].

The LSP is non-propagating waves. In case of a spherical NPs, the curved surface of the nanoparticle creates a restoring force on the electrons to result in a localized resonance. This kind of resonance can be excited by direct light irradiation [100], as shown in Fig (2-6).

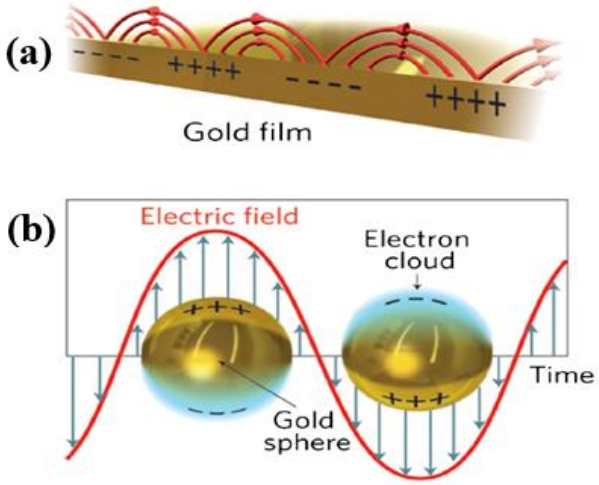


***Fig (2-6) Schematics for the two main ingredients of plasmon resonance: a) propagating the SPP along the dielectric-metal interface; and b) the LSP on the surface of a metal NPs [100].***

This occurs only when the incident light frequency (w) is close to the plasma frequency of the metal, which is in the visible frequency range for good conductors like gold and silver, the incident external electric field excites the free electrons and displaces it from their normal positions in the metal lattice. Movement of oscillating free electron can be described by equation of motion [101].

$$m_e x'' + m_e \gamma x' = -q_e E \qquad (2.2)$$

where $m_e$ is the free electron mass, $x$ is the electron displacement, $q_e$ is the electron charge and $E$ is the external electric field, $\gamma$ is electron damping factor.

The general solution of oscillating electric field is $E = E_0 e^{-iwt}$ so that the solution of equation (2.2) for given amplitude $x_0$ is [102].

$$x_0 = \frac{q_e}{m_e (w^2 + iw\gamma)} E_0 \qquad (2.3)$$

where $w$ is the angular frequency. While in the case of ($N$) number of electrons a macroscopic polarization is rise $P = -N q_e^2 \chi$ and given by [102]:

$$P = -\frac{N q_e^2}{m_e(w^2 + iw\gamma)} E \qquad (2.4)$$

The electric displacement $D$ depends on the dielectric function of the free electron as [102]

$$D = \epsilon_0 E + P \qquad (2.5)$$

So that equation (2.5) becomes[102] ;

$$D = \epsilon_0 \left(1 - \frac{w_p^2}{(w^2 + iw\gamma)}\right) E \qquad (2.6)$$

The plasma frequency of the free electron is [103]:

$$w_p^2 = \frac{N q_e^2}{\epsilon_0 m_e} \qquad (2.7)$$

The dielectric function of the free electron ($\epsilon_w$ ) is [103]:

$$\epsilon_w = 1 - \frac{w_p^2}{w^2 + iw\gamma} \qquad (2.8)$$

The equations describe the behavior of plasmonic in a bulk metal using the Drude model.

For very small spherical metallic nanoparticles (compared to the wavelength of incident light), the nanoparticle polarizability (***Pa***) is[104]:

$$Pa = 4\pi R^3 \frac{\epsilon(w) - \epsilon_d}{\epsilon(w) + 2\epsilon_d} \qquad (2.9)$$

where ***R*** is the nanoparticle radius, $\epsilon(w)$ is the metal's dielectric function and $\epsilon_d$ is the dielectric function of the surrounding.

The LSP resonance occurs when the polarisability of the nanoparticle reaches to maximum value i.e. $(\epsilon(w) + 2\epsilon_d)$ is minimized.

The optical cross section of the spherical NPs enhances (strong scattering and absorption properties) under plasmonic conditions and given by[105]:

$$\sigma_{scs} = \frac{k^4}{6\pi} |Pa|^2 \qquad (2.10)$$

$$\sigma_{acs} = kIm[Pa] \qquad (2.11)$$

where $\sigma_{scs}, \sigma_{acs}$ are the scattering and the absorption cross sections, ***k*** is the wave vector of incident light and $I_m[Pa]$ is the imaginary part of polarizability.

## 2.5 Thermo-Plasmonic

Recently, researchers have realized that plasmonic nanoparticles can act as an effective heat source depending on opto-heating generation. Therefore, the metal nanoparticles can be considered as nano-heat sources when they are irradiated by laser or, they are directly affected by the external electromagnetic fields, which opens up a new field set of applications in nanotechnology named as Thermo-Plasmonic [106].

Thermo-Plasmonic is a field that study thermodynamic effects at the nanoscale of plasmonic nanomaterials including measuring and

controlling of the result temperature [107]. Thermo-plasmonic is considered as a new way of increasing temperature remotely by light beam [108]. Part of incident electric filed interacts with mobile electrons of metal nanoparticles and turns in to heat through three thermalization steps [109]: Photon-electron interaction, Electron-phonon coupling, and surrounding thermalization [110], this is processes of different time scales [111] as follows:

**Photon- electron interaction:** part of incident light energy gets absorb by free electrons of metal. This process takes around 100 fs and leads to non-equilibrium with respect to lattice [112].

**Electron-phonon coupling:** in this step excited electrons get relax with time scale of 1.7 ps depending on nanoparticle size and nanoparticle at this step has an uniform temperature [113].

**External thermalization:** the heat energy transfer from nanoparticle to heat up the surrounding medium with time scale of few nanosecond depending on nanoparticle size [114] as:

$$\tau = \frac{\rho\, c_p R}{3 k_{med}} \qquad (2.12)$$

where, τ is typical duration of transient regime, $\rho$ is the material density, $c_p$ is the material specific heat and $k_{med}$ is the thermal conductivity of surrounding medium.

The generated heat power ($Q_{(r,t)}$) in metal nanoparticle at any time ($t$) and position ($\mathbf{r}$) is [115]:

$$Q_{(r,t)} = J_{(r,t)}\, E_{(r,t)} \qquad (2.13)$$

where $E$ is the electric field inside the NP and $J$ is the current density of electrons.

Uniform incident electric field is considered which lead to uniform heat source density because the thermal conductivity of metal much larger than that of surrounding medium [116].

When the electric field with a proper wavelength illuminates the metal nanostructures, free electrons oscillate coherently in a localized region. The electromagnetic field near metallic surface is highly enhanced. The position of the plasmon resonance is sensitive to the dielectric environment within near field region [117]. Scattering and absorption cross sections of metallic nanoparticles are enhancing under illumination of visible or near-infrared electromagnetic radiation [118].

Laser induced materials processing is based mainly on the absorption of laser radiation in the material, which results in various effects, such as heating, vaporization, plasma formation, melting, and ablation. The extent of these effects depends primarily on the characteristics of the laser radiation (laser intensity, laser wavelength, beam spot size, the pulse repetition rate, and interaction time), as well as the thermo-physical, the electronic structure, and optical properties of the material (the material surface, thermal conductivity, specific heat capacity, and mass density)[119]. The main advantage of using pulsed laser irradiation is to achieve temperature confinement in space and time over nanoscale dimensions [120].

For this reason, the investigation of thermo-physical and optical phenomena use the samples under the laser irradiation is so important. Mainly, find the best classes of samples to this aim is beneficial for any scientist. Generally the field of thermo-plasmonic has two challenges: the micro/nanoscale particle design and the temperature measurement [121].

## 2.6 Laser Ablation

The process of removing material from a surface of solid target (placed in liquid or gas) by irradiating with a laser radiation is called laser ablation[122], it has become a convenient method for the fabrication of NPs [123]. The advantages of the method in comparison with chemical routes of synthesis are its simplicity, absence of precursors that can contaminate the ablated material, and potential for synthesis of compound nanostructures that cannot be synthesized chemically due to energy barrier constraints [124]. Furthermore, the nanoparticle characteristics can be modified by the laser radiation parameters: such as the energy, pulse duration [125], and wavelength [126], as well as properties of the target material and surrounding [127].

### 2.6.1 Laser Ablation in Liquid

The laser ablation in liquid (LAL) method is one of the most promising approaches to generate pure and uncontaminated nanoparticles (highly pure without other remnants from the chemical reactions) with mechanism simple, convenient, and fast process relatively. In addition to, It possesses a highly rate of mass production at a low cost [128,129].

It is important to note that laser ablation in liquids provides much better opportunities to manipulate the size and other properties of nanoparticles. In particular, ablation in liquids enables to control the size and size distribution of nanoparticles by the addition of various chemically active compounds into liquid solutions. It involves the use of short pulses of laser energy focused on a target in a solvent. The target absorbs the energy from the laser pulse and is vaporized. The vaporized material then condenses as nanoparticles [130].

### 2.6.2 Laser Ablation in Liquid Mechanism

The ablation of the target material upon laser irradiation is a very complex process. The incident laser pulse penetrates into the surface of the material within a certain penetration depth. This dimension is dependent on the laser wavelength and the refraction index of the target material and is typically in the range of 10 nm. When solid target absorbs the later part of the laser pulse, after that an electric field with very high intensity is produced on the surface of the irradiated area, the strong electrical field generated by the laser light is sufficient to remove electrons from the bulk of the penetrated volume within 10 microseconds for a nanosecond laser pulse, this electric field produces strong repulsive force between ions. This repulsive force is larger than the bond strength, which cause surface of the solid material is stripped and this process indicates as a Coulomb explosion [131].

The free electrons oscillate within the electromagnetic field and can collide with the atoms of the bulk material, thus the energy is transfer to the surrounding liquid [132]. At a high enough laser flux, the material is typically converted to plasma, as shown in Fig (2-7), which contains various energetic species including atoms, molecules, electrons, ions, clusters, particulates, and molten globules.

Subsequently, the large pressure difference between the laser produced initial seed plasma and ambient atmosphere causes a rapid expansion of the plasma plume and then it cools down. After collapse of cavitation bubble the pressure and the temperature are decrease lead to cooling of the plasma plume and release small nanoparticles [133].

The mechanism for the C/S NPs architectures are the result of a two-step approach, consisting of preparation of nanoparticles and then modification of their surface, or an in-situ approach during particle formation. The formation of the Ag core/Au shell NPs as shown in Fig

(2-7) [132]. When the Au plate is ablated in Ag colloidal solution, the Au plate absorbs most of the incident laser energy. As a result, Au atoms escaping from the Au surface can be deposited on the spherical surface of Ag particles to form an Au shell in such a rich-Au-atoms environment. With the ablation time increased, the Au shell could be formed due to the rich-Au-atoms environment and the thickness of Au shell increases gradually as well. The coupling between the core and the shell could lead to surface plasmon resonance (SPR) properties different from the nanoparticles made of each individual component [134].

The miscibility of two materials should be high and the interfacial energy should be as small as possible to form C/S NPs so that the material which choose should not differ significantly in their lattice constant (lattice mismatch within (1-3%) [135].

To achieve a uniform C/S NPs by laser ablation in liquid:

- The sequence of mixing should be carefully selected.
- Controlling the change of the temperature.
- The ablation time should be choosing correctly, where the thickness of the shell can be controlled by the ablation time.

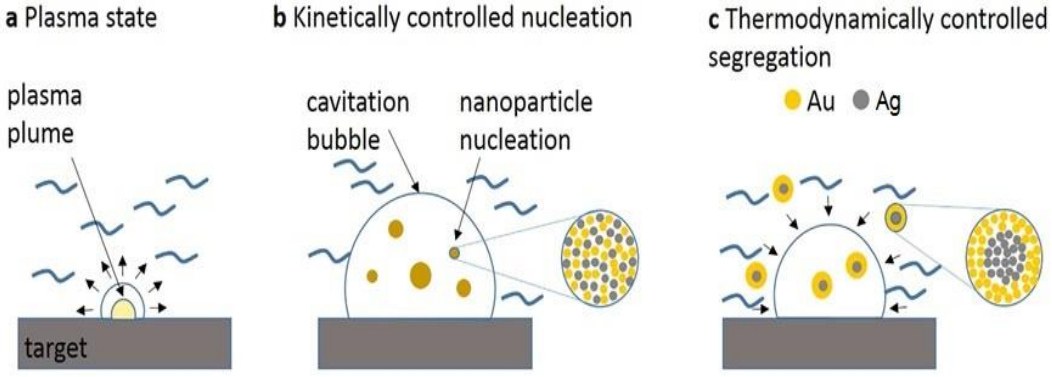


***Fig (2-7) Steps of the C/S NPs formation mechanism after laser pulse absorption. (a) Plasma formation and initial cavitation bubble formation, (b) expansion of the cavitation bubble into the liquid and rapid cooling of the ablated matter, and (c) cavitation bubble collapse and nanoparticle release into the liquid [132].***

## 2.7 Linear optical properties

The optical properties appeared when there were interaction between the electromagnetic waves and transparent materials, this interaction depends on the material type and the nature of the charge distribution inside of the material. The optical phenomena such as absorbed, transmitted and reflected are very important to get information about the internal structure, the nature of the matter bonds, and determine direct and indirect energy transitions [136,137].

### 2.7.1 The Absorbance (A)

The absorbance study for the colloidal solutions very important and gives information about the optical density and the refractive index. In addition, the valuable information such as the electronic band structure and the optical energy band gap are obtained by absorption coefficient. The absorbance is the relation between the concentration of the molecules in the sample and the thickness of the sample [136,137].

$$A = Log\ (I_0/I) \qquad (2.14)$$

where: $I_0$: intensity of incident ray, $I$: intensity of the transmittance ray through the sample.

The energy transfer from the incident electromagnetic wave to the material passing through it, this happens by the electric field of the incident photon interacts with the momentum of the electric dipole of the material. This leads to the electron a rise to a higher energy level, so decrease the incident intensity [136,137].

$$I = I_0\ e^{-\alpha l} \qquad (2.15)$$

When the incident energy sufficient to cause an electronic transition in the matter, the absorbance increase with increases the concentration of the molecules that absorb the electromagnetic wave and the numbers of incident photons, according to Beer Lambert's law "For a given material,

the sample path length and concentration of the sample is directly proportional to the absorbance of the light." The Beer lambert law applied if the "light monochromatic" [136,137].

$$A = \epsilon c l \qquad (2.16)$$

where: $\epsilon$ molar extinction coefficient (molar absorptivity) $M^{-1}$ $cm^{-1}$, ***C*** molar concentration of the absorber substance in (M), $l$ optical length.

### 2.7.2 The Absorption coefficient (α)

The Absorption coefficient is an important optical factors, which represent how far light penetrate before absorbed by the material. The Absorption coefficient depends on the photon energy and properties of the material under study. The absorption coefficient can be determined from the optical absorption spectrum by the following equation[136,137].

$$\alpha = 2.303 \frac{A_0}{t} \qquad (2.17)$$

where, $t$ is the sample thickness and $A_0$ is defined by log ($I_0/I_T$) where $I_0$ and $I_T$ are the incident intensity and transmitted intensity beams, respectively.

### 2.7.3 The Refractive Index and Extinction Coefficient

The Refractive Index (n) is the ratio between the velocity of light in vacuum (c) to the velocity of the light in medium (v), ***n = c/v***.

The refractive index for specific material vary with the wavelength of the incident electromagnetic wave and excepting some material which refractive index changing according to the direction of the electromagnetic waves inside the material, so these materials can change

the direction of polarization of these wave, so the complex refractive index ($\bar{n}$) represented by the following equation [136,137]:-

$$\bar{n} = n + i\kappa \qquad (2.18)$$

where, n: the real part (the usual) of complex refractive index, κ: extinction coefficient is the imaginary part of the complex refractive index, both depend on frequency (ν).

$$\kappa = \alpha\lambda/4\pi \qquad (2.19)$$

When an electromagnetic wave at a certain frequency falls on a material it works to change the position of the material charge from its original position producing a dipole. so the electrical polarization of the molecule will oscillate with the frequency of the electromagnetic wave, this will transfer part of the energy of the incident wave to oscillating energy for the generated electric dipole, this will reduce the amplitude of the incident wave.

There is a relation between the refractive index and the polarization caused by the electromagnetic wave, when refractive index increase leads to decrease the speed of the light inside matter, the delay effect increases. But when the value of the refractive index is equal to one that means there is no delay and there is no polarization [136,137].

### 2.7.4 Dielectric Constant

Real and imaginary parts of the complex dielectric constant represent the polarization ability of the matter and dissipated energy under irradiation respectively. In other words, the real part of the dielectric constant shows how much it will slow down the speed of light in the sample and the imaginary part of the dielectric constant shows how a dielectric absorbs energy from an electric field due to dipole motion.

The real part and imaginary part of the dielectric constant have been determined by equations [138]:-

$$\varepsilon = \varepsilon_1 - i\varepsilon_2 \quad (2.20)$$

$$\varepsilon_1 = (n^2 - k^2) \quad (2.21)$$

$$\varepsilon_2 = (2nk) \quad (2.22)$$

where $\varepsilon$ is the dielectric constant, $\varepsilon_1$ is the real part of the dielectric and constant $\varepsilon_2$ is the imaginary part of the dielectric constant.

## 2.8 Numerical Simulation

### 2.8.1 Optical Part

Finite element method is used via COMSOL Multiphysics to find a numerical computation of absorption cross section for the proposed core/shell NP in different media. Optical properties of our small core shell NPs of volume V and radius *R* in different surrounding media with the relative permittivity are $\boldsymbol{\epsilon} = (\boldsymbol{n} - \boldsymbol{ik})^2$ has been calculated by means of electrostatic polarizability ($\boldsymbol{P_a}$), Where both the absorption and scattering cross sections mainly depend on the electrostatic polarizability of the nanosphere [139,140]:

$$\boldsymbol{P_a} = \frac{3\,V\,(\varepsilon_w - \varepsilon_d)}{4\pi(\varepsilon_w + \varepsilon_d)} = \boldsymbol{R^3}\,\frac{\varepsilon_w - \varepsilon_d}{\varepsilon_w + 2\varepsilon_d} \quad (2.23)$$

where $\boldsymbol{\varepsilon_w}$ **and** $\boldsymbol{\varepsilon_d}$ are the dielectric constant of nanoparticles and surrounding medium respectively.

Then the absorption cross sections are depending on normalized polarizability ($\boldsymbol{P}$) is given by:

$$\boldsymbol{C_{abs} = \frac{12k\,\varepsilon_d Im(\varepsilon_w)}{R^3|\varepsilon_W - \varepsilon_d|}\left|P^2\right|} \qquad \textbf{(2.24)}$$

$$\boldsymbol{K = \frac{2\pi\varepsilon_d^{1/2}}{\lambda}} \qquad \textbf{(2.25)}$$

where $\boldsymbol{k}$ is the wave number in the medium and the normalized polarizability as:

$$\boldsymbol{P = \frac{P_a}{1 + \phi_{(KR)} R^{-3} P_a}} \qquad \textbf{(2.26)}$$

In which, the function $\boldsymbol{\phi_{(KR)}}$ represent the radiative decay as;

$$\boldsymbol{\phi_{KR} = 2 + 2(IKR - 1)\, exp(i\, KR) \approx -(KR)^2 - i\frac{2}{3}(KR)^3} \qquad \textbf{(2.27)}$$

For NPs, equation (2.26) is reduced to the known approximations:

$$\boldsymbol{P = R^3 \frac{\varepsilon_w - \varepsilon_d}{\varepsilon_w + 2\varepsilon_d - i(\frac{2}{3})(KR)^3(\varepsilon_w - \varepsilon_d)}} \qquad \textbf{(2.28)}$$

We have the core/shell NPs for this reason must go to multilayer particle of radius $R_1$ in a medium with the permittivity $\boldsymbol{\varepsilon_d}$ , equivalent polarizability $\boldsymbol{P_{av}^1}$ which gives the same dipole moment as that for the initial particle, is known. Then, we determine the equivalent mean permittivity $\varepsilon_{av}^{(1)}$ :

$$\boldsymbol{P_{av}^1 = R_1^3 \frac{\varepsilon_{av}^1 - \varepsilon_d}{\varepsilon_{av}^1 + 2\varepsilon_d}} \qquad \textbf{(2.29)}$$

For a usual sphere $\boldsymbol{\varepsilon_w = \varepsilon_{av}^1 = \varepsilon_1}$ and $\boldsymbol{R}$=$\boldsymbol{R_1}$

Let now assume that a particle( $\boldsymbol{\varepsilon_{av}^{1}}$ ,$R_1$)is surrounded by an external layer of radius $R_2$ with the permittivity $\boldsymbol{\varepsilon_2}$,then the polarizability of that core/shell sample by equivalent dipole method as it explained completely in [141].

$$\boldsymbol{\varepsilon_{av}^{2} = \varepsilon_2 \frac{1 + 2f_{12}P_{12}}{1 - f_{12}P_{12}}} \qquad \textbf{(2.30)}$$

In which $\boldsymbol{P_{12} = \frac{\varepsilon_1 - \varepsilon_2}{\varepsilon_1 + 2\varepsilon_2}}$ and $\boldsymbol{f_{12} = \frac{R_1^3}{R_2^3}}$

Further, in order to calculate the absorption of the NPs with the radius of R, absorption cross section by [142] is used:

$$\sigma_{abs} = \frac{2\pi}{k_e^{\,2}} \sum_{l=1}^{\infty} (2l+1)[\mathrm{Re}(a_l + b_l) - (|a_l|^2 + |b_l|^2)] \qquad \textbf{(2.31)}$$

Where $a_l$ and $b_l$ are the Mie scattering coefficients which defined as a function of Riccati-Bessel functions as $\psi_l(q_i) = q_i j_l(q_i)$ and $\xi_l(q_e) = q_e h_l(q_e)$ with internal and external wave numbers as $q_i = \sqrt{\varepsilon_i}\, k_0 R$ and $q_e = \sqrt{\varepsilon_e}\, k_0 R$

$$a_l = \frac{q_i \psi_l(q_i)\psi_l'(q_e) - q_e \psi_l(q_e)\psi_l'(q_i)}{q_i \psi_l(q_i)\xi_l'(q_e) - q_e \xi_l(q_e)\psi_l'(q_i)}$$
$$b_l = \frac{q_e \psi_l(q_i)\psi_l'(q_e) - q_i \psi_l(q_e)\psi_l'(q_i)}{q_e \psi_l(q_i)\xi_l'(q_e) - q_i \xi_l(q_e)\psi_l'(q_i)} \qquad \textbf{(2.32)}$$

### 2.8.2 Thermal Part

The photo-thermal response of plasmonic the core/shell NPs which arise from absorption of incident light energy was investigated using COMSOL multi-physics, the time depending of the heat transfer model was used, based on the Drude Lorentz model [139,140] to investigate the

heat transferred from spherical core/shell nanoparticle that illuminated by the CW laser radiation to the surrounding media, with similar boundary conditions that used to find the optical properties. The system is described by heat transfer equation [143].

$$\boldsymbol{\rho_{(r)} C_{(r)} \frac{\partial T_{(r,t)}}{\partial t} = \nabla . \left( k_{med(r)} \nabla T_{(r,t)} \right) + Q_{(r,t)}} \qquad \textbf{(2.33)}$$

where $T_{(r,t)}$ is the local temperature, $\boldsymbol{Q_{(r,t)}}$ is the optical dissipation in NP, $\boldsymbol{k_{med(r)}}$ , $\boldsymbol{C_{(r)}}$and $\boldsymbol{\rho_{(r)}}$ are thermal conductivity, specific heat and mass density of the material respectively. The thermodynamic physical constants of the used material are shown in Table (2-1).

***Table (2-1) the physical constants of the used materials [144-148].***

| *Parameters* | *Au* | *Ag* | *Si* | *Water* | *PVP* | *Unit* |
|---|---|---|---|---|---|---|
| *Thermal conductivity (k)* | *317* | *424* | *123* | *0.6* | *2.8* | *W/(m·K)* |
| *Specific heat capacity* $(c)$ | *129* | *234* | *711* | *4187* | *3428* | *J/(kg·K)* |
| *Mass density* $(\rho)$ | *19320* | *10490* | *2203* | *1000* | *1200* | *kg/m³* |

The temperature generated of the core/shell NPs when exposed to CW laser in the effective volume is given by [149];

$$T^{cw} = \frac{I\,\sigma_{acs}}{4\pi\,K_{med}\,r}\,(1+\lambda) \qquad for \quad r > R \qquad \textbf{(2.34)}$$

$$T^{cw} = \frac{I\,\sigma_{acs}}{4\pi\,K_{med}\,R}\,(1+\lambda) \qquad for \quad r < R \qquad \textbf{(2.35)}$$

While the temperature generated of the core/shell NPs that exposed to laser pulse is given by:

$$T^{PL} = \frac{I\,\sigma_{acs}}{\rho\,c\,V} \qquad \textbf{(2.36)}$$

Where $\boldsymbol{I\,\sigma_{acs}}$ **=** $\boldsymbol{Q}$ is the heat power, $\boldsymbol{I}$ is laser average irradiance, $\sigma_{acs}$ is absorption cross-section, $\boldsymbol{r}$ is the position distance, $\boldsymbol{R}$ is the radius of the

nanoparticle, $k_{med}$ is the thermal conductivity of surrounding media, $\rho$ is the mass density, $c$ is the specific heat capacity, $V$ is the nanoparticle volume. The generated heat power is considered to be uniform inside the NPs because of the thermal conductivity of the metals is much larger than that for surrounding [139,140].

### 2.8.3 Surface Electric-Field Distribution on the Boundary between Nanoparticles Interface

At the boundary between noble metals and semiconductors or dielectric materials, the density of electric charges increases, and these charges vibrate with the electromagnetic wave at a certain frequency, this is called SPR. The SPR Leads to thermo-plasmonic enhancement in the plasmonic nanoparticles by raises the temperature of nanoparticles, when the charge transition between the boundaries increases.

In this work, the nanoparticles of hybrid systems are adopted to study the distribution of electromagnetic fields of the different systems from the plasmonic nanoparticles. So that the electric field and surface charge distributions in the spherical nanoparticles were simulated, then hybrid systems (core/shell) were stimulated under the same boundary conditions using COMSOL multiphysics by the frequency domain method, by using electromagnetic waves of the wavelengths (190-900nm).

## 2.9 The E-coli Bacteria

The Escherichia coli, is a Gram-negative, rod-shaped, facultative anaerobic, coliform bacterium of the genus Escherichia that is organisms a member of the Enterobacteriaceae family, it is the most prevalent commensal organism in the gastrointestinal tract of humans and

warm-blooded animals, as well as one of the most important pathogens [150,151].

The E. coli is one of the most common causes of bacterial infections in humans and animals, it is notable cause of enteritis, urinary tract infection, septicemia, and other clinical infections, such as neonatal meningitis [152].

The prevalence of multidrug-resistant the E. coli strains is increasing worldwide mainly due to the spread of mobile genetic elements, such as plasmids [152]. The E. coli is intrinsically resistant to therapeutic levels of penicillin, due to its outer membrane barrier [153]. As the E. coli is resistant to several different classes of antibiotics, the E. coli is able to survive and adapt in many extra-intestinal habitats and spread resistance among humans [153].

The emergence of new bacterial strains that are resistant to current antibiotics has become a public problem, which has increased the need to develop a new antibacterial materials, the silver NPs produced unique, superior and indispensable properties and much attention has been drawn to their properties [153]. Its uniqueness arises from a higher surface-to-volume ratio and an increase in the percentage of atoms at the grain boundaries. They represent an important class of materials in the development of a new devices that can be used in various physical, biological, biomedical and pharmaceutical applications, the silver NPs adhered to the cell wall of the bacteria and penetrated the cell membrane. This led to the inhibition of bacterial cell growth and multiplication leading to bacterial cell death [151-154].

# Chapter Three Experimental Part and Simulation

## 3.1 Introduction

This chapter includes a step description preparation the samples of the C/S NPs and materials used in preparation, it also explains the experimental set-up which is required for laser ablation in liquid method to fabricate the C/S NPs samples. In addition, the techniques used characterization for the C/S NPs. And also the temperature detection setup is presented to measure the temperature elevation of the samples during the irradiation of lasers.

In this chapter, a simulation program is performed for a better understanding of the heat generated in plasmonic media and the diffusion of surrounding under illuminating with laser light at their corresponding plasmonic wavelength. Besides, the optical properties have been studied by finding a numerical computation of the absorption cross-section for the proposed C/S NPs in this work.

Furthermore, we get an understanding of the heat generated in plasmonic media and the diffusion of surrounding under illuminating with laser light at their corresponding plasmonic wavelength.

## 3.2 Experimental Work

The experimental work includes two parts namely, the first part includes synthesis techniques for the samples, where it used technique laser ablation in liquid to fabricate bare nanoparticles and also prepared the C/S NPs as well as the C/M-S NPs, which are based on (Au, Ag, and Si). While the second part includes characterization techniques used to characterize samples, where it used several techniques we will explain later.

### 3.2.1 Fabrication Technique of Samples: Laser Ablation in Liquids

The experiments were conducted by using the 1064 nm Nd:YAG laser, have 5 ns pulse width, and 6 Hz repetition rate. Energy per pulse was 120 mJ focused directly on the sample placed in a liquid medium. Fig (3-1) shows the schematic diagram of the experimental setup of laser ablation in liquid mediums.

The laser pulses were directed at the pure (99.9%) (Au and Ag) (Sigma Aldrich, Germany) metal targets with a thickness of 2 mm, and also the Si target (>99.99% purity, Sigma Aldrich, Germany) with a thickness of 2mm, were used as targets, immersed in various aqueous solutions inside a glass container with a high reflectivity mirror and a lens with focal length 150mm. The height of water over the target was maintained at 10mm. In the meantime, the entire system slowly rotates about its vertical axis during the ablation process to prevent developing deep holes in the target, and therefore keep the same surface conditions for each laser pulse. Subsequently, the distance between the target and the lens has been set to get the focus point on the target.

The liquid media used distilled deionized water, PVP polymer (Polyvinyl pyrrolidone) that dissolved in 1% deionized distilled water using a magnetic stirrer. For comparison, 1% PVA polymer (Polyvinyl alcohol) has been used dissolved in deionized distilled water by a magnetic stirrer at room temperature, in order to obtain more stability for the colloidal solution. The PVP powder is dissolved in pure water with mixing ratio of 1:100 and put on magnetic stirrer for 15min. The PVP is exhibits interesting features, such as nontoxic polymer [155], high chemical stability [156], good biodegradability [157], quick dissolution in water [158], easy film formation processability [159], excellent stabilizing agent for noble metal particles [160], and tissue compatibility [161]. Given these features, the PVP is widely used in medical applications,

such as pharmaceutical production [162], blood plasma substitution[163], and drug delivery system [164].

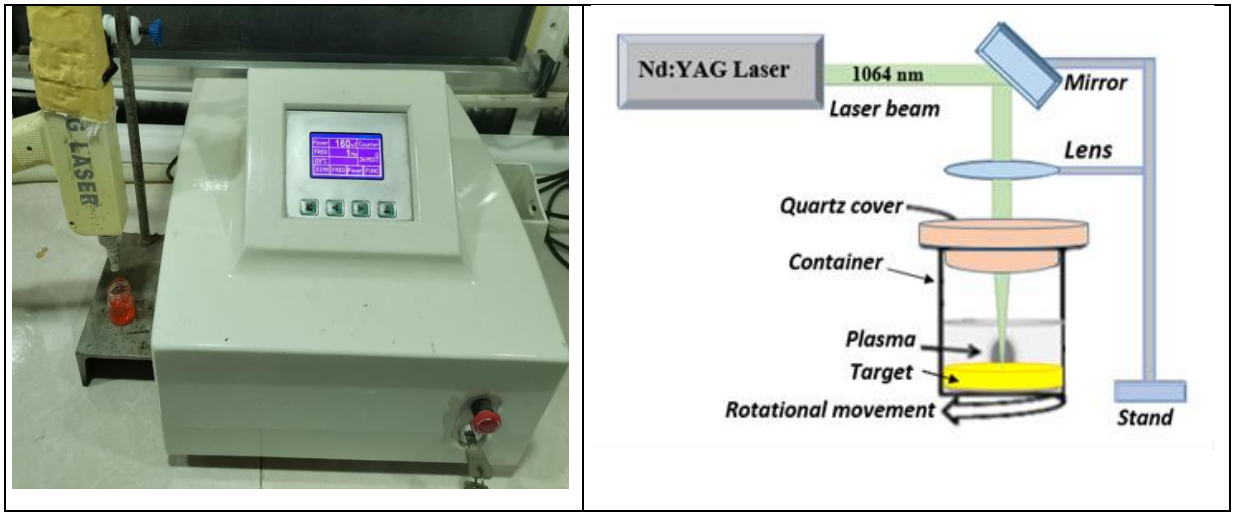


***Fig (3-1) shows a scheme of the experimental setup used in NPs preparation by laser ablation confined in a liquid medium.***

### 3.2.2 The Samples Preparation

Three groups of NPs by laser ablation in liquid were prepared, which are eleven samples for all groups;

#### 3.2.2.1 The Bare Nanoparticles Group

There are three samples of bare NPs, which are from the Au, Ag, and Si NPs in PVP. The ablation time for producing the bare NPs was 3min. The colloidal solution preparations samples are described in Fig (3-2).


***Fig (3-2) the colloidal solution preparations samples for the bare NPs group.***

### 3.2.2.2 The Core/Shell NPs Group

There are six samples of core/shell NPs (Au@Si, Ag@Si, Si@Au, Si@Ag, Au@Ag, and Ag@Au NPs) in PVP, producing these six samples using a sequential method of two steps for each sample, which will be explained in the following paragraph.

A two-stage sequential ablation method was used for the preparation of bimetallic the C/S NPs. First, a core NPs colloid solution was prepared using laser ablation of an Au target in deionized water with the PVP polymer. Irradiation of the target endured for 3 min and has been accompanied by a homogeneous liquid coloration in a characteristic bright red color due to the SPR band of Au NPs in the visible region, followed by ablation of the Si target in a colloidal solution Au NPs prepared. The Si NPs act as a shell for ablated hot Au species. However, the ablation duration was 2-3 min as shell for the Si NPs to obtain core/shell morphology with variable shell thickness.

A similar procedure was performed using Ag NPs as a core with Si NPs as a shell to produce the Ag@Si C/S NPs, the ablation time for producing core was 3 min and for shell was 2 min, has been accompanied by a homogeneous liquid coloration in a characteristic yellow color due to the SPR band of Ag NPs in the visible region. The colors of the colloidal suspensions obtained in our samples are the characteristic ones due to the presence of Ag, and Au NPs. Namely, this is proof that the sample has a SPR absorption spectrum that changes thusly as per their NP sizes. The colloidal solution preparations the C/S samples are described in Fig (3-3).


***Fig (3-3) the colloidal solution preparations samples for the C/S NPs group.***

### 3.2.2.3 The Core/Multi-Shell NPs Group

There are two samples of core/multi-shell NPs (Au@Si@Ag, and Ag@Si@Au NPs) in PVP. The hybrid multi-shell nanostructures consist of gold-silver and silver-gold sandwich with silicon shell in between. The ablation time for producing core NPs was 3-2 min for all shell NPs. The colloidal solution preparations the C/M-S samples are described in Fig (3-4).


***Fig (3-4) the colloidal solution preparations samples for the C/M-S NPs group.***

### 3.2.3 Characterization Techniques of Samples:

#### 3.2.3.1 The Measurement of Absorption Spectra

The linear optical properties of samples have been dedicated by optically transmission and absorption spectra from deep UV to visible region (the wavelength range 190 – 900 nm). The absorption spectra were measured at room temperature using (CE 7400- UV/VIS) double beam spectrophotometer supplied by Aquarius (South Korea) as in Fig (3-5).

***Fig (3-5) the UV-Visible Spectrophotometer.***

### 3.2.3.2 Measurement of the Refractive Index of Colloids

In order to measure the refractive index of all samples under illumination of lamps of different wavelengths, to show the effect of wavelength on the refractive index of the liquid samples under study. A refractometer device (NOVEX, HOLLAND) is used illuminated by a LED lamps (green, blue, red, and white lamp). The refractometer is an easy-to be-used, manually operated device that measures the refractive index of liquid samples with high accuracy and depends on the wavelength used in lighting. As shown in Fig (3-6).

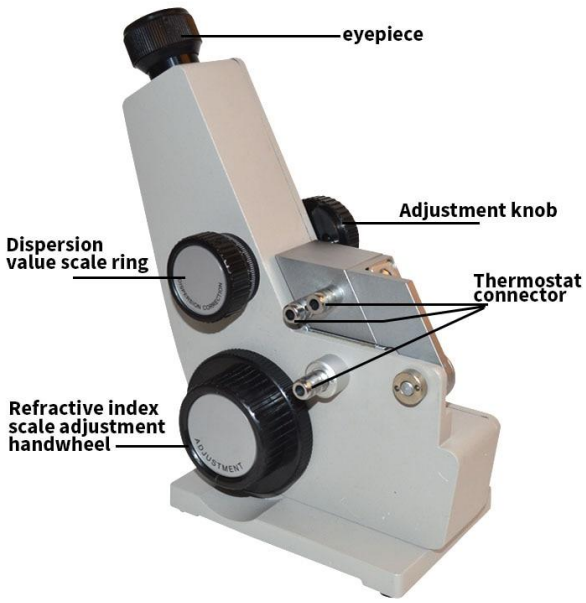


***Fig (3-6) the Refractometer.***

### 3.2.3.3 Field Emission Scanning Electron Microscopy (FE-SEM)

In order to investigate the C/S NPs shape, size and the thickness, Field Emission Scanning Electron Microscopy was used (FE-SEM) (ΣIGMA, JSM-7610F, Carl Zeiss, Germany) image operating at an accelerating voltage of 10 kV. As shown in Fig (3-7). While the average size of the C/S NPs was calculated from FE-SEM images via Image J software.

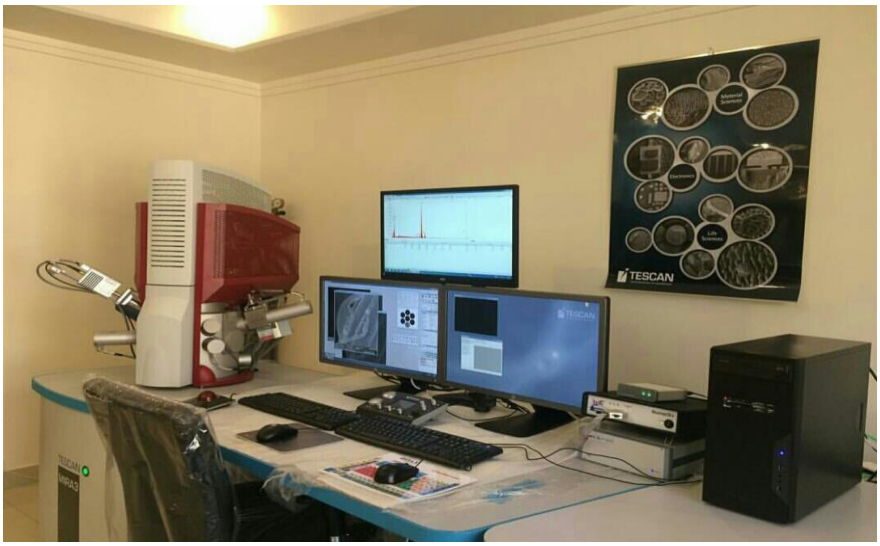


***Fig (3-7) Schematic of the FE-SEM device.***

### 3.2.3.4 Photo-Thermal Characterization (Temperature Detection)

In order to determine the photo-thermal effect for all samples that used in this work. The temperature elevation of a colloidal is measured is by recording the heat rise of the absorbing NPs which act as an efficient point sources of heat. In general, a key issue examined here is the convertibility of light into the heat of the core/shell plasmonic NPs of different nanostructures [165].

A IR camera can converts the infrared energy emitted from the objects to an electronic images, it shows the temperature of the object surface as a thermal image. The IR camera have an optical elements focus IR energy on detector chip which contains many detector pixels (arranged as grid), each pixel converts the incident IR energy on it to signal, then these signals goes to the camera processor which creates a color map sends to the camera memory then the camera displays a color image represent the temperature of the surface object.

It has been used the high resolution thermal imaging camera (type of EIRC5s) during laser direct irradiation in order to reveal the temperature elevation, which is caused by the conversion of light into heat with the

help of plasmonic nanostructures. Three lasers were used to illuminate the prepared samples. First, we used CW Nd:YAG laser, operates with 30 mW power and 532 nm wavelength. Second, used a 30 mW diode laser with a wavelength (473 nm). Subsequently, used a 30 mW diode laser with a wavelength (405 nm) to compare and study the effects of the laser wavelength on the samples. Nevertheless, the thermal images were recorded at room temperature of all samples under fixed conditions, the sample illumination time for the laser was 4 minutes per sample, the setup as shown in Fig (3-8).

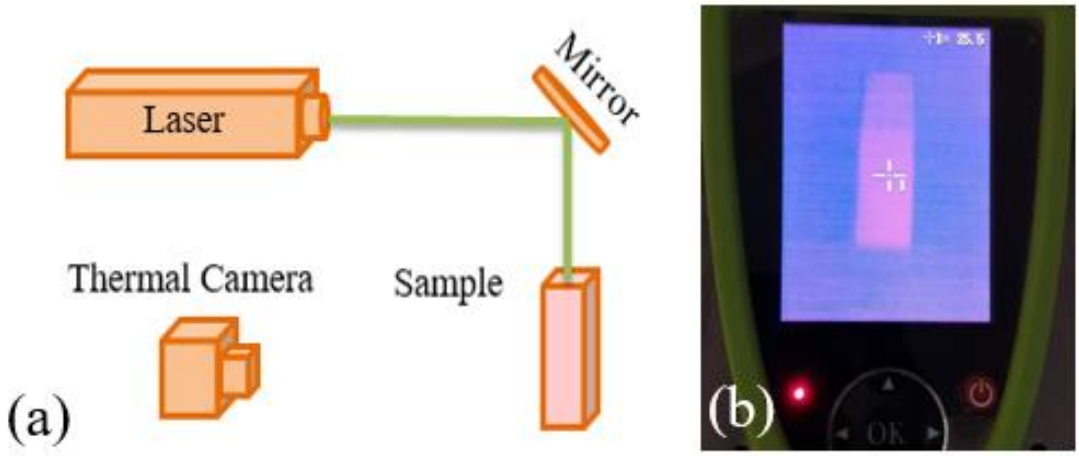


***Fig (3-8): a) Diagram of the experimental setup used of the thermo-plasmonic imaging, b) the thermal images at room temperature recorded by thermal camera for the colloidal solution preparations samples.***

### 3.2.3.5 Antibacterial Activity

The gram-negative E.coli bacterial were used to analyze the antibacterial against the nanostructures proposed in this work. The bacteria are clinically isolated from complex blood samples, to prepare them for later use [166]. Neatly, to prepare the nutrient broth, 1 gram of Mueller Hinton Agar (MHA) was dissolved in 100mL of distilled deionized water. The mixture is melted at a temperature of 120° C under

continuous magnetic stirring for 20 minutes. After that, the solution is left to cool and distributed on a petri-dish. After the mixture freezes, the E-coli bacteria are distributed onto the surface of the petri dish by agar well-diffusion method. Then, leaving the dish of agars at 37 °C for 24 hours of incubation for bacteria to grow well. Moreover, the wells are making in the middle of the agar following the standard well diffusion procedures[167], which were punched using the sterile cork borer with 10mm diameter. The wells were flooded with 100 µl of the C/M-S NPs solution was used as an antibacterial positive control. Subsequently, the wells containing the nanostructures are irradiated by laser at different wavelengths (405,473 and 532 nm) during three different periods, each period lasted 5 minutes, to compare it with non-laser irradiated wells. Finally, the diameter of the inhibition zones (DIZ) [168], around the well impregnated with the C/M-S NPs were monitored, as in Fig (3-9). To demonstrate the effect of thermo-plasmonic on the activity of bacteria studied in this work.

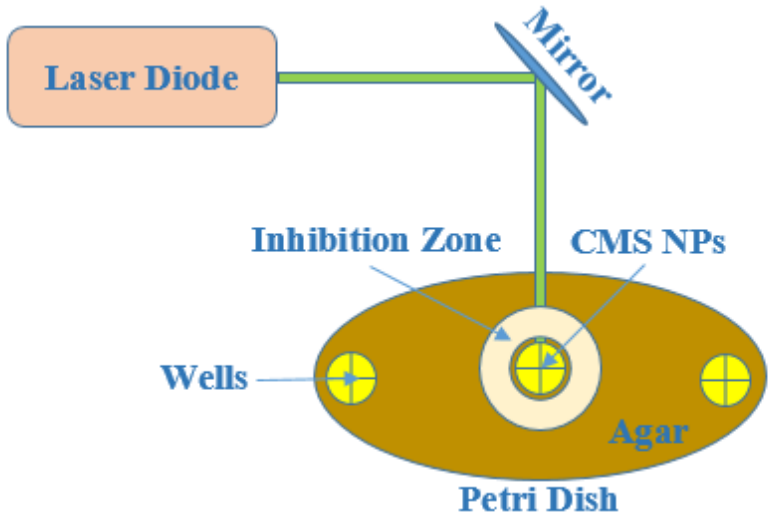


***Fig (3-9) the diagram of the experimental setup used of the antibacterial activity.***

### 3.3 Simulation Program

In this order, a simulation program is performed for a better understanding of the heat generated in the plasmonic media and the diffusion of surrounding under illuminating laser light at their corresponding plasmonic wavelength. As well as is the understanding of the electronic transport of the electric charges at the boundary between the metal/metal and the metal/semiconductor to reach an understanding of physical phenomena at the boundary between two materials.

The design and investigation of the plasmonic C/S NPs at different nanosystems were simulated using the COMSOL multi-physics program. The simulation software package based on the Finite Element Analysis (FEA), Frequency Domain Method (FDM), and Drude-Lorentz model for heat transfer by study the variation in optical and opto-thermal characteristics, and also study the distribution of the electromagnetic fields by the local distribution of surface charges. The frequency domain model of electromagnetic waves is coupled with a heat transfer model to solve the thermo-plasmonic effects on sub-wavelength scale.

### 3.4 Sample Description

A spherical symmetry of core- shell nanoparticles of core radius “R” and shell thickness “t” of samples are proposed. The core radius used is (5, 10,15,20,25, and 30 nm) for Au NPs.

In the second stage the core radius is fixed at 30 nm for shell thicknesses (15 nm) for the first shell for the C/S NPs, as for another shell thicknesses (15 nm) for the second shell for the C/M-S NPs.

The samples are immersed in homogeneous polymeric matrix of the deionized water with 1% of the PVP polymer, to be similar of the experimental work.

The thickness of the Perfectly Matched Layer (PML) is chosen to be λ/2. The symmetry of a quarter of a sphere is only considered from the simulation geometry to get faster results than multiplied by four as shown in Fig (3-10).

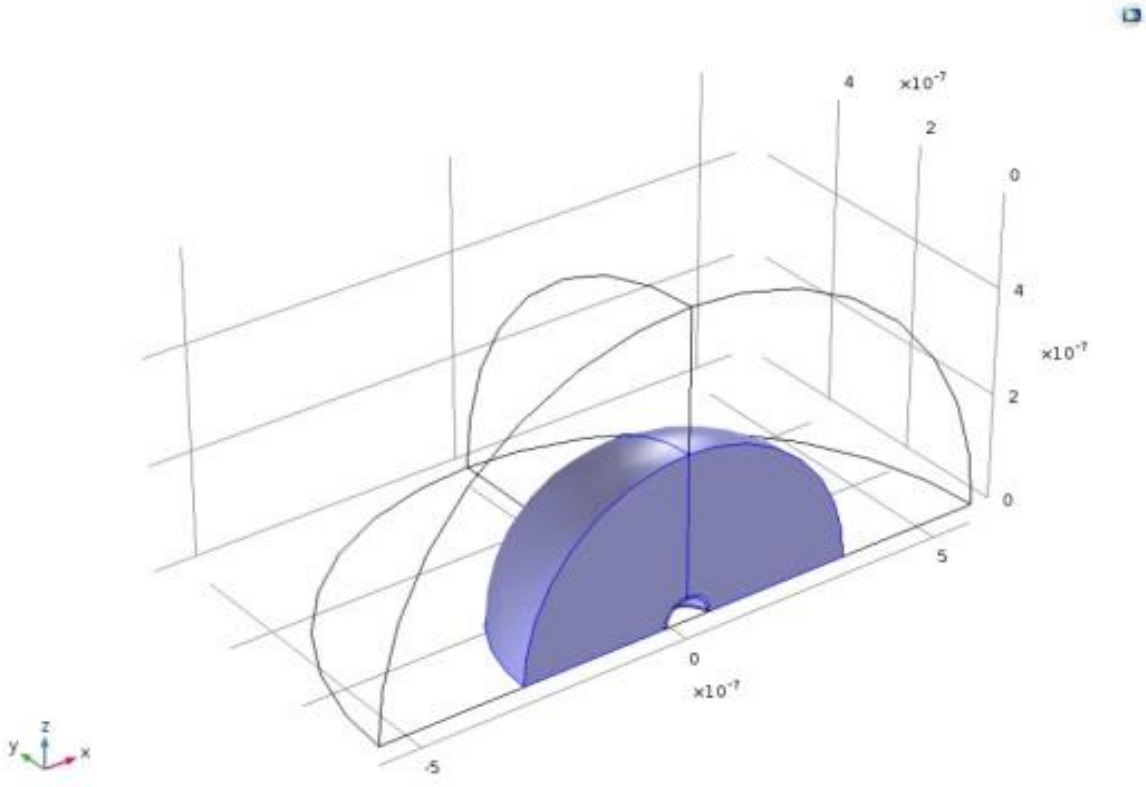


***Fig (3-10) Geometrical structure of one quarter of the core-shell nanoparticle in homogeneous liquid medium.***

Fig (3-11) shows the geometrical mesh structure of the core/shell NPs. The high mesh quality of λ/6 could be selected in this model. Real and imaginary components of the refractive indices of all materials air, water, PVP, gold, silver and silicon were interpolated [139,169].

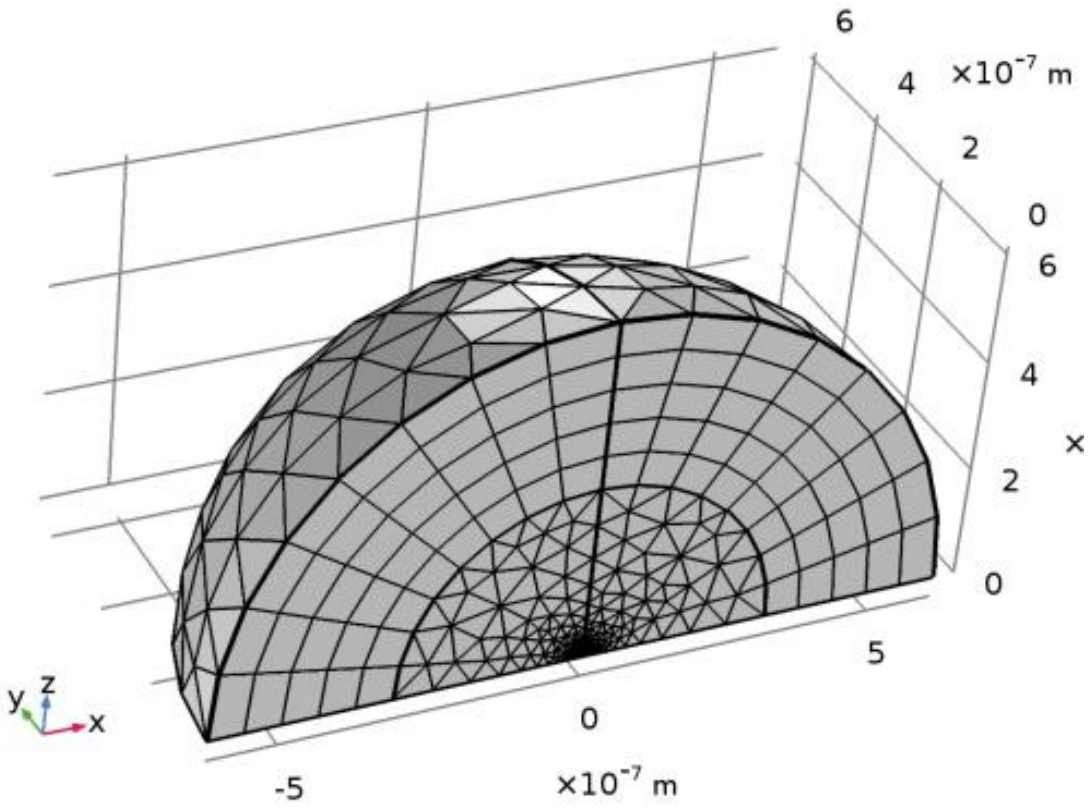


***Fig (3-11) Geometrical mesh structure of core-shell nanoparticle in liquid medium.***

# Chapter Four
# Results and Discussion

## 4.1 Introduction

This chapter includes the results of the experimental measurements used of characterization for the hybrid nanostructures manufactured in this study for evaluating their performance, where it includes characterization the shape and size of the core/shell nanostructures, as well as the results of measurements of their linear optical properties and also the characterization of their thermo-plasmonic properties. In addition, the results of measure the temperature elevation of the samples under external effects are also described, as well as the results of tested the hybrid nanostructures as an antibacterial. Also involve the results of the simulation programs used to describe the experimental results. Besides, it involved the discussion of all results this study.

## 4.2 The Experimental Results

### 4.2.1 The Results of Measurements, Linear Optical Properties

The optical spectra for the prepared samples were measured by using a UV–Vis spectrophotometer. The behavior is shown in Fig (4-1) of the bare NPs.

Fig (4-1a) shows the UV-Vis absorbance of the gold NPs in different liquid media, it can be noted that each sample has an absorbance peak due to the SPR for the gold NPs according to surrounding media of the nanoparticle. The SPR peak is more pronounced in the PVP solution, compared to other solutions, which makes it more stable than the deionized water and the PVA polymer, this result agrees with Ref [170].

Moreover, due to larger NPs in the PVP medium, which was confirmed by FE-SEM, red shift in the SPR wavelength from 522 to 526 nm can be

noticed. This fact leads to increasing the refractive index of the medium leads to the ability to modify the SPR wavelength of the samples, this result is confirmed by comparison with the Ref [38]. It is noticed from Fig (4-1b) that the absorption spectrum of silver NPs increased in PVP polymer compared to distilled water at different ablation times for the same reason. Increasing the size of NPs in turn leads to increasing the refractive index of the medium, and also can be notice a shift towards long wavelengths (red shift) for the absorption spectrum of about (406-414nm), when changing both the liquid medium and the ablation time, which is evidence of an increase in the size and stability of NPs in the PVP polymer matrix compared to deionized water.

The absorption spectrum of the silicon NPs samples in the deionized water solution and the PVP solution for different ablation times (3-12 min) is illustrated in Fig (4-1c), which can see more effective absorption of silicone in the PVP matrix and increase the intensity of silicon absorbance with increasing ablation time.

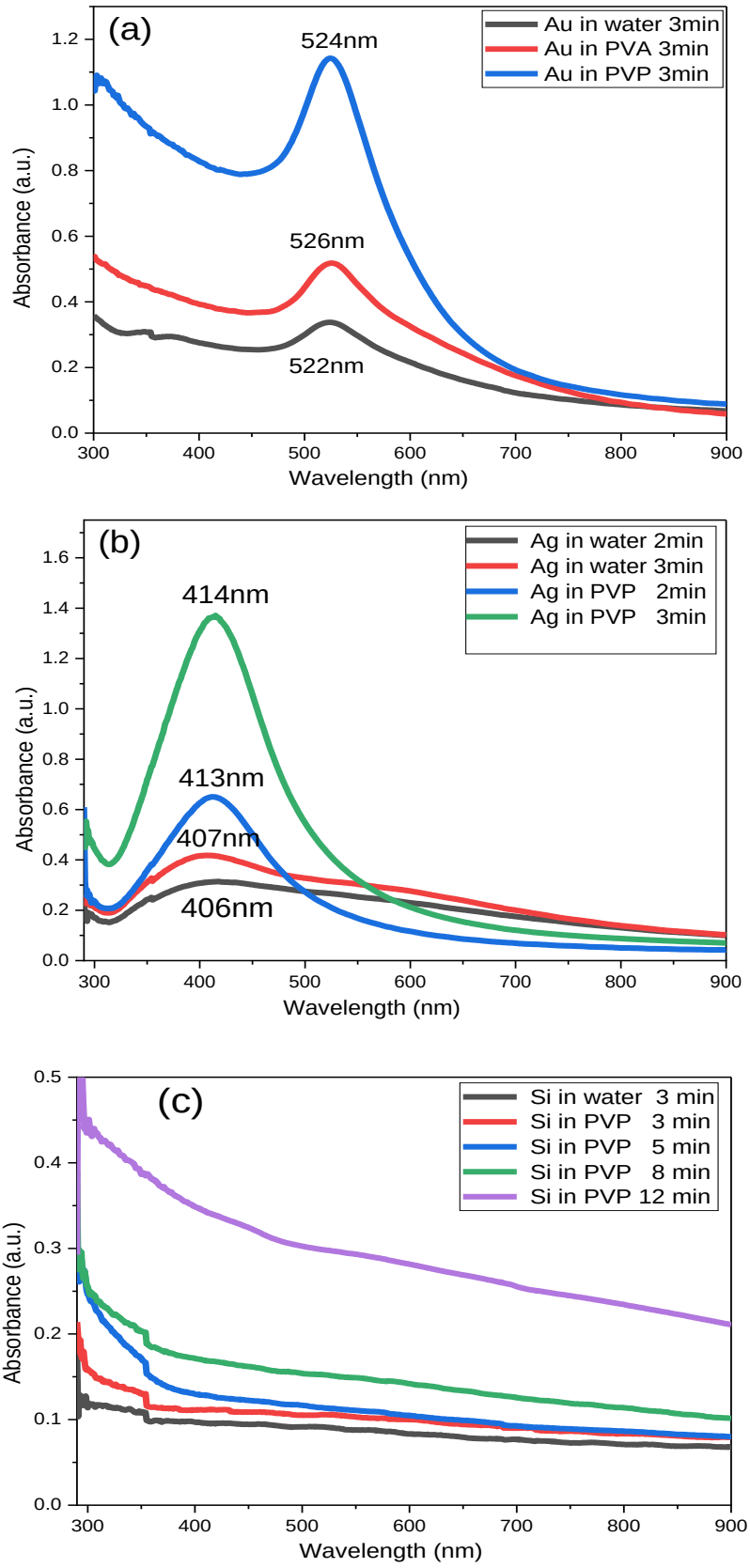


***Fig (4-1) the absorption spectra of the bare NPs; a) the gold NPs in different liquid medias for3 min ablation, b) the silver NPs for different ablation time, and c) the silicon NPs for different ablation time.***

As it was expected, in the spectra of absorbance for the (M/S) core/shell when silicon is shell, there is an increase in the intensity of absorbance with a redshift in the wavelength when compared to the silicon core, as shown in Fig (4-2a).

But clearly notice at the metal/metal (M/M) core/shell NPs and the Metal/Semiconductor/Metal (M/S/M) core/multi-shell NPs samples, two distinct peaks which come from the absorption of plasmonic noble metals the gold NPs and the silver NPs in the core/shell, as shown in Fig (4-2b). The SPR position controlled of the red shift in wavelength, which is confirmed in these hybrid nanostructures samples as shown in Table(4-1).

The silicon shell over the metal core leads to the extended near-field due to coupling between the core of the noble metal and the shell of the silicon, which also changes the position SPR towards the far wavelength (redshifts) accompanied by a decrease of the maximum near-field enhancement [33]. Subsequently, increasing the total size of the C/S NPs makes the SPR enhancement weakens at their redshifted resonance, it compared to Ref [171].

It is well known that, the position of the plasmon can be adjusted and tuned into the optical window through controlling their geometry by controlling the type and size of the metallic nanomaterials, and also the SPR position is affected by the refractive index of the surrounding medium [172]. Consequently, when adding a silicon shell over the metal core, the nearfield is extended because of the plasmonic coupling between the core of the noble metal NPs and the shell of the silicon NPs, which also changes the position of the SPR towards redshift wavelength, accompanied by decreasing in the maximum nearfield enhancement. Thus, increasing the total size of the C/S NPs makes nearfield enhancement weaken at their redshifted resonance wavelength [173].

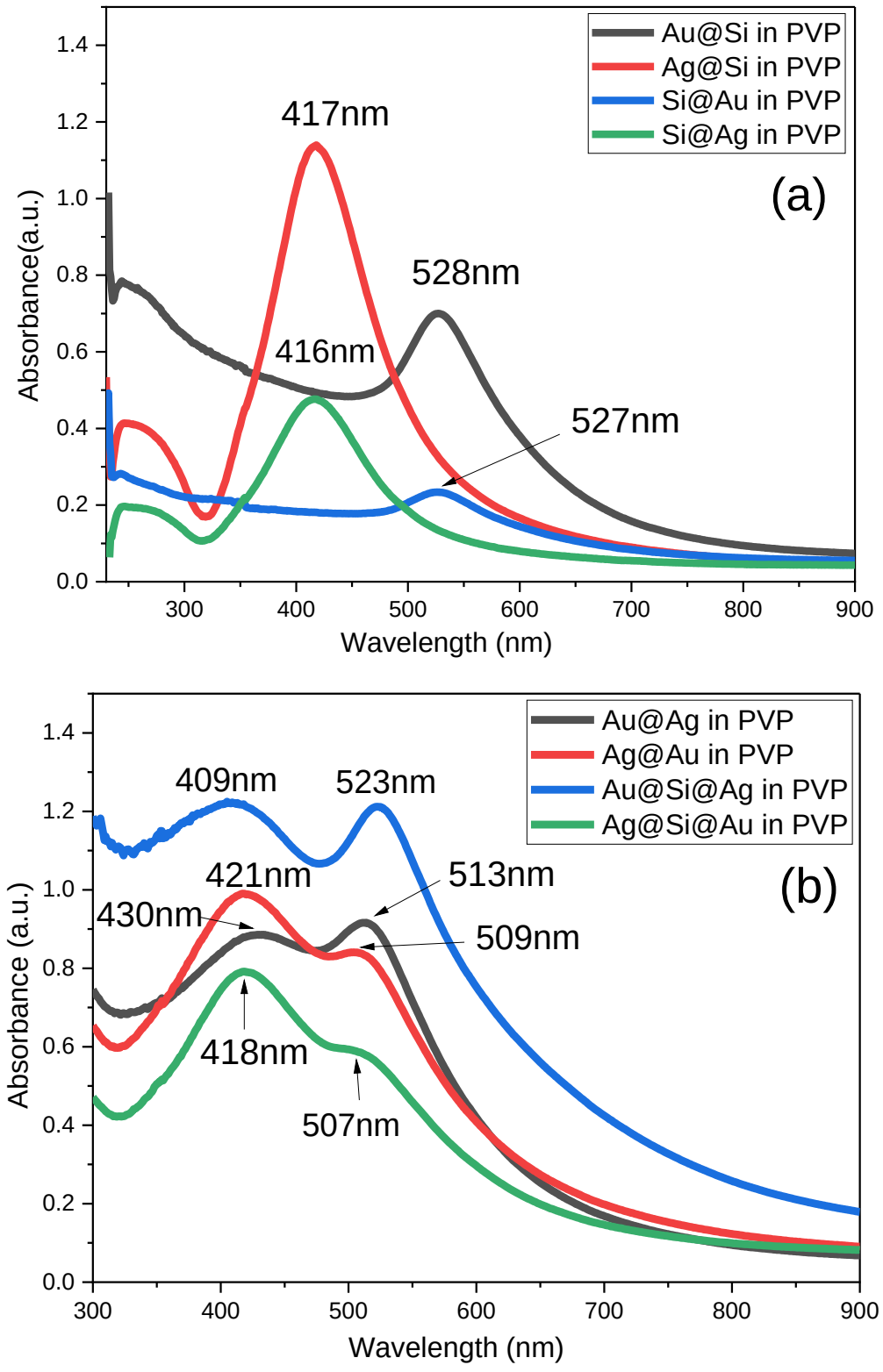


***Fig (4-2) the absorption spectra of the C/S NPs; a) M/S core/shell NPs for different compositions, b) M/M core/shell NPs and M/S/M core/multi-shell NPs for different compositions.***

***Table (4-1): the SPR controlling with different compositions of the hybrid NPs, the ablation time was 3 min for core and 2min for all shell.***

| Samples | SPR in PVP matrix |
|---|---|
| Au@Si NPs | 528 nm |
| Ag@Si NPs | 417 nm |
| Si@Au NPs | 527 nm |
| Si@Ag NPs | 416 nm. |
| Au@Ag NPs | 513@430 nm |
| Ag@Au NPs | 421@509 nm |
| Au@Si@Ag NPs | 523@409 nm |
| Ag@Si@Au NPs | 418@507 nm |

### 4.2.2 The Results of FE-SEM

The morphology of the samples, the size and the shape were investigated using FE-SEM images. The average size of used C/S NPs are calculated using (Image J) software, It is selected randomly a number of the NPs to take the average size, maximum core diameter and shell thickness was measured for samples in the deionized water and the polymeric solution. The results showed that the average size of the gold NPs in the PVP polymeric solution increases when compared to the deionized distilled water solution (from 15 to 20 nm) as in Fig (4-3), and this is due to the reason for NPs to be collected inside the polymer. This result agrees with [174,175], and also noticed that the density of the gold NPs in the PVP polymeric solution is greater when compared to the distilled water, and this is due to the fact that the polymeric solution is

more stable to keep the nanoparticles from sedimentation to the bottom of the container after a period of time.

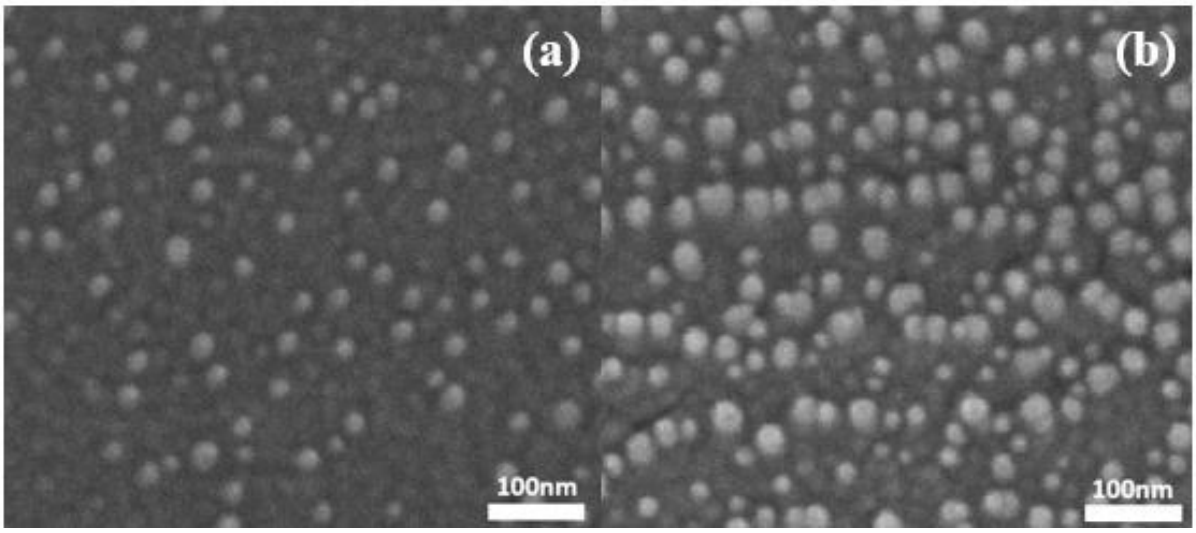


***Fig (4-3) Image of the FESEM for a) Au NPs in the distilled water, and b) Au NPs in the PVP solution.***

In addition, the samples were obtained of metal phase/semiconductor core/shell nanostructures in quasi-spherical morphology. The results show that all the examined samples successfully formed the shell clearly and distinctly. The behavior is shown in Fig (4-4). The core/shell nanostructures are made of gold, silver, and silicon particles in an aqueous solution of the PVP polymer, with the core size ranging from 20–30 nm and the shell from 10–20 nm for Au@Si NPs as in Fig (4-4a), and Si@Ag NPs as in Fig (4-4b), with a slight increase in the average size of samples for the C/M-S hybrid nanostructures, as in Fig (4-4c) and Fig (4-4d).

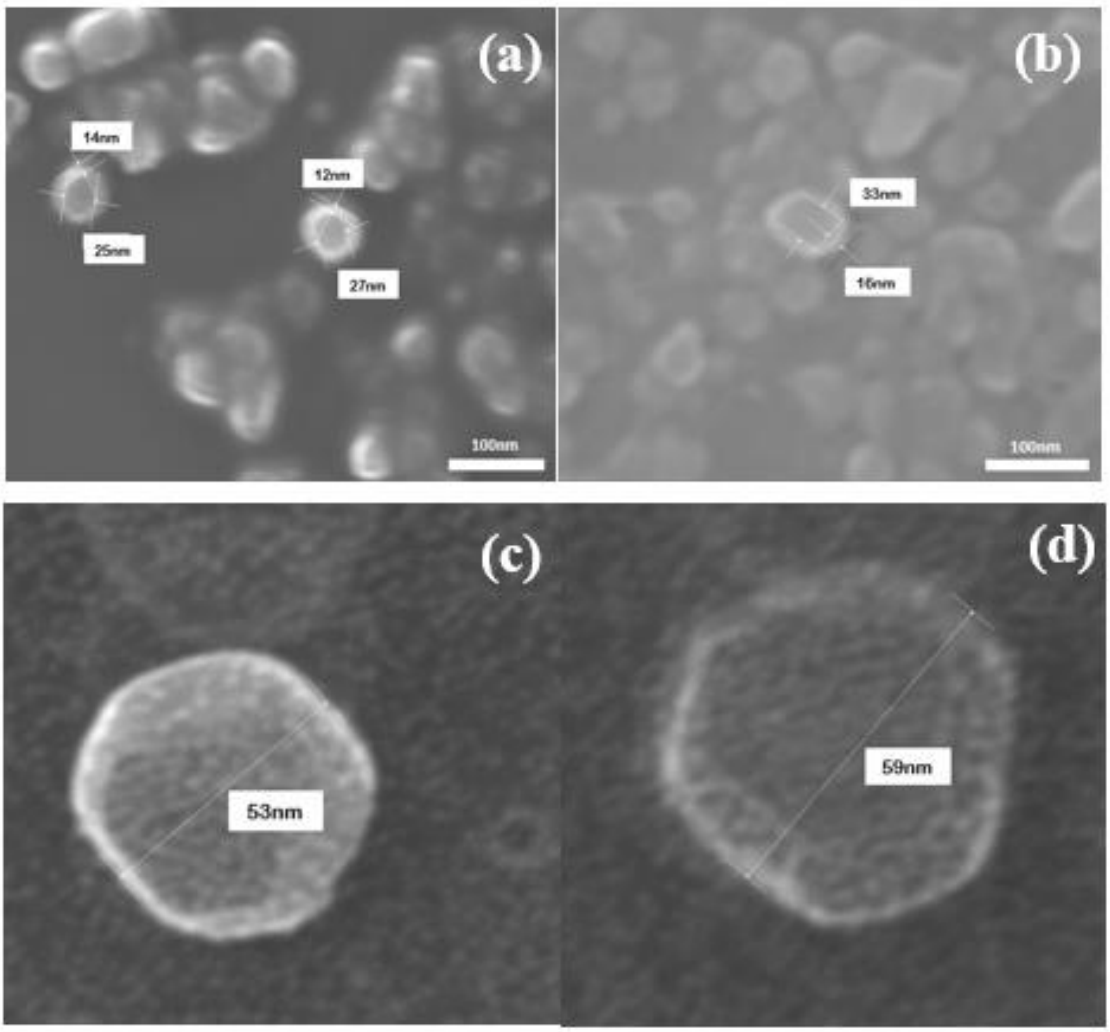


***Fig (4-4) the FESEM image of a) Au@Si NPs, b) Si@Ag NPs, c) Au@Si@Ag NPs, and d) Ag@Si@Au NPs in PVP.***

### 4.2.3 The Results of the Refractive Index

The refractive index results for all samples measured using the refractometer device under illumination green, blue, red, and white lamps respectively, as shown in Fig (4-5). Based on the results, the refractive index of all samples depends on the wavelength of the light used in the illumination. As well as the results showed that the refractive index of the C/M-S NPs samples increase slightly compared to the refractive index of the C/S NPs samples, and the bare NPs have a lower refractive index than

hybrid NPs. It is evident from the above that adding a shell NPs of the nanoparticle or increasing size of the nanoparticle leads to an increase in its refractive index depending on the wavelength of the light used.

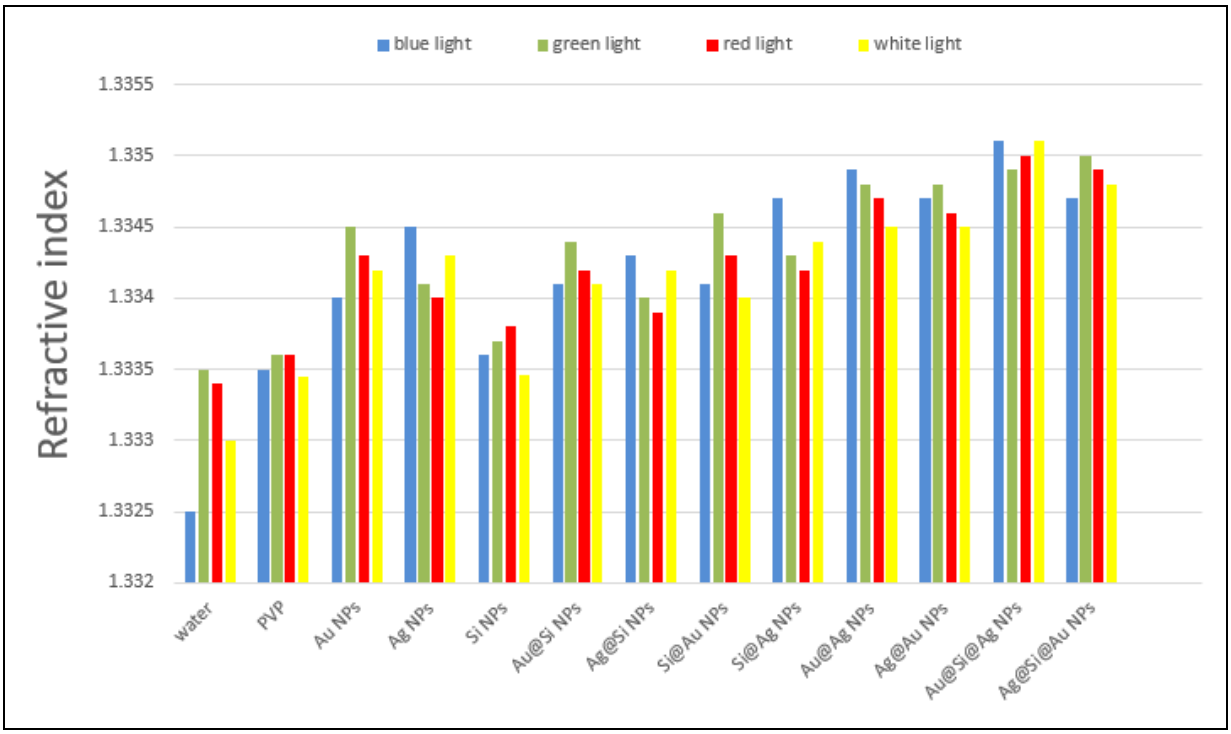


***Fig (4-5) the refractive index for all samples under lamps illumination at different wavelengths immersed PVP matrix.***

### 4.2.4 The Results of Dielectric Properties

As known that the dielectric properties of material are very important and have a major role in determining the intensity and position of the peak of the SPR of the plasmonic NPs [174].

As expected, the coupling between the plasmonic noble metals with semiconductors yields a change in the dielectric properties. This in turn leads to a change the real and imaginary part of the refractive index for all samples [175,176]. Through the relationships between the real and the

imaginary dielectric coefficients as a function of the refractive index of the samples can be calculated by equations (2.20) and (2.21).

The Fig (4-6) shows the real dielectric parameter of the C/S NPs and the C/M-S NPs, and the Fig (4-7) shows the imaginary dielectric parameter of the C/S NPs and the C/M-S NPs. The real and the imaginary parts of the dielectric coefficient in these figures were extracted from the empirically measured absorption spectra to find the main optical properties of the samples in the PVP polymer matrix.

Moreover, the coupling between the silicon NPs and the plasmonic metal NPs in the C/S NPs leads to a high tunability of the surface plasmon position. As well as a clear negative increase in the real dielectric constant, due to increasing the extinction coefficient, it is understood when we compare Fig (4-6a) for the C/S NPs with Fig (4-6b) for the C/M-S NPs, as two distinct peaks are observed in the real part of the dielectric coefficients.

It is clear that the SPR was improved for the Au@Si@Ag NPs sample, where the silver NPs in the shell region increases the plasmonic property, which leads a clear redshift in wavelength. By contrast, in the Ag@Si@Au NPs sample, no significant change in the position and the intensity of the SPR was observed.

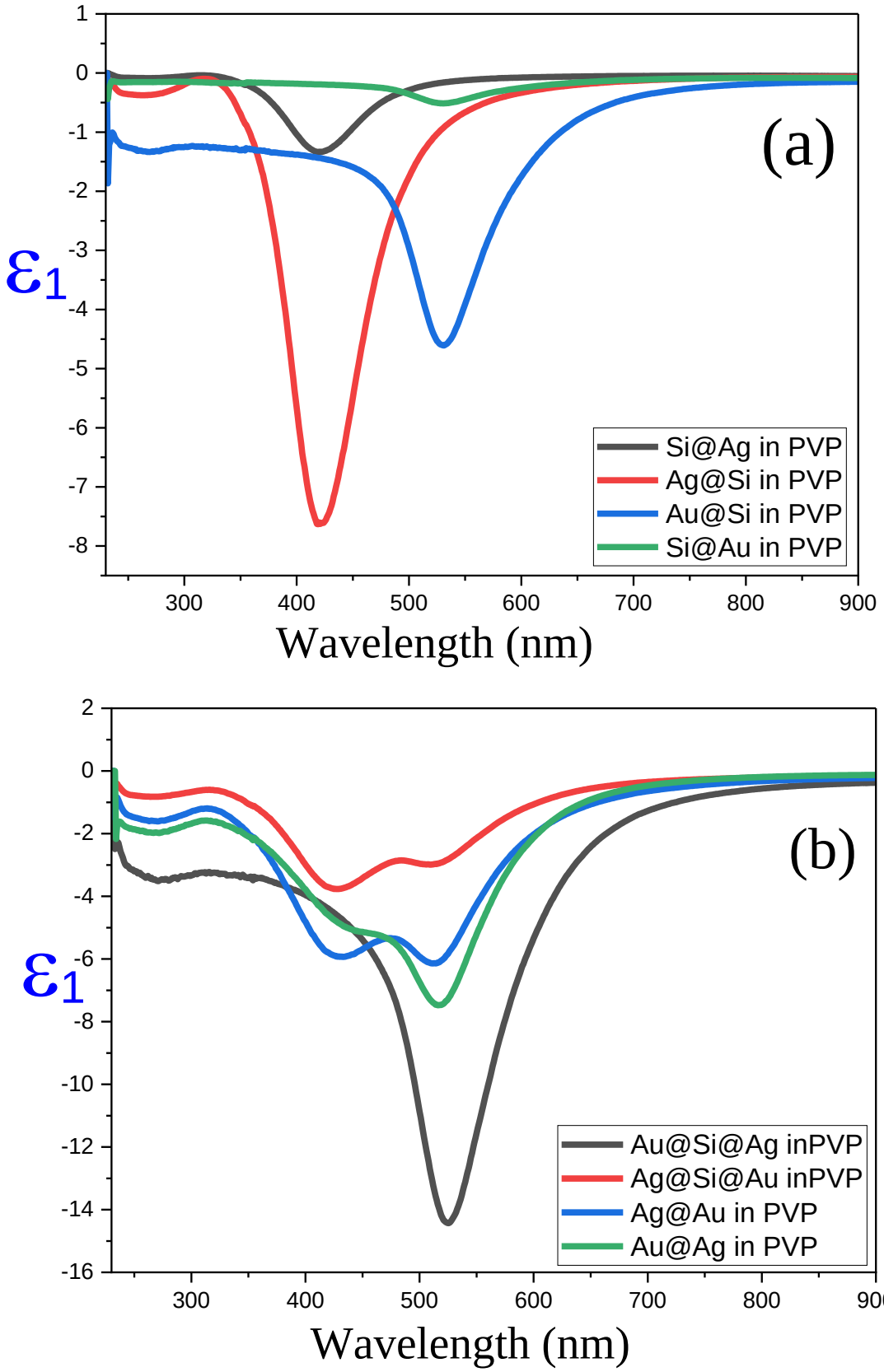


***Fig (4-6) the real dielectric coefficient as a function of wavelength in the matrix of the PVP polymers, for samples; a) the M/S core/shell NPs, b) the M/M and M/S/M core/shell NPs.***

To better understand the results, the imaginary dielectric properties discussed as a function of the imaginary refractive index, as it gives a clearer picture of the surface plasmon behavior of NPs, just as studied the real value of the refractive index, where one complements the other. This change can be realized by the fact that the properties of the plasmon intensity and position can be determined with high accuracy by describing the imaginary dielectric properties of the material through the imaginary refractive index.

When the silicon NPs is shell of the C/S NPs samples becomes an improvement in plasmon intensity, as in Fig (4-7a). We also notice an increase in the plasmon intensity of the Au@Si@Ag NPs in the imaginary dielectric constant curve, as in Fig (4-7b), this is because of an increase in the refractive index, as well as the coupling between the plasmonic properties of the gold NPs and the silver NPs with the semiconductor properties of the silicone NPs, which led to a change in the refractive index of all samples according the eq (2.21). The results are consistent with studies [170-172].

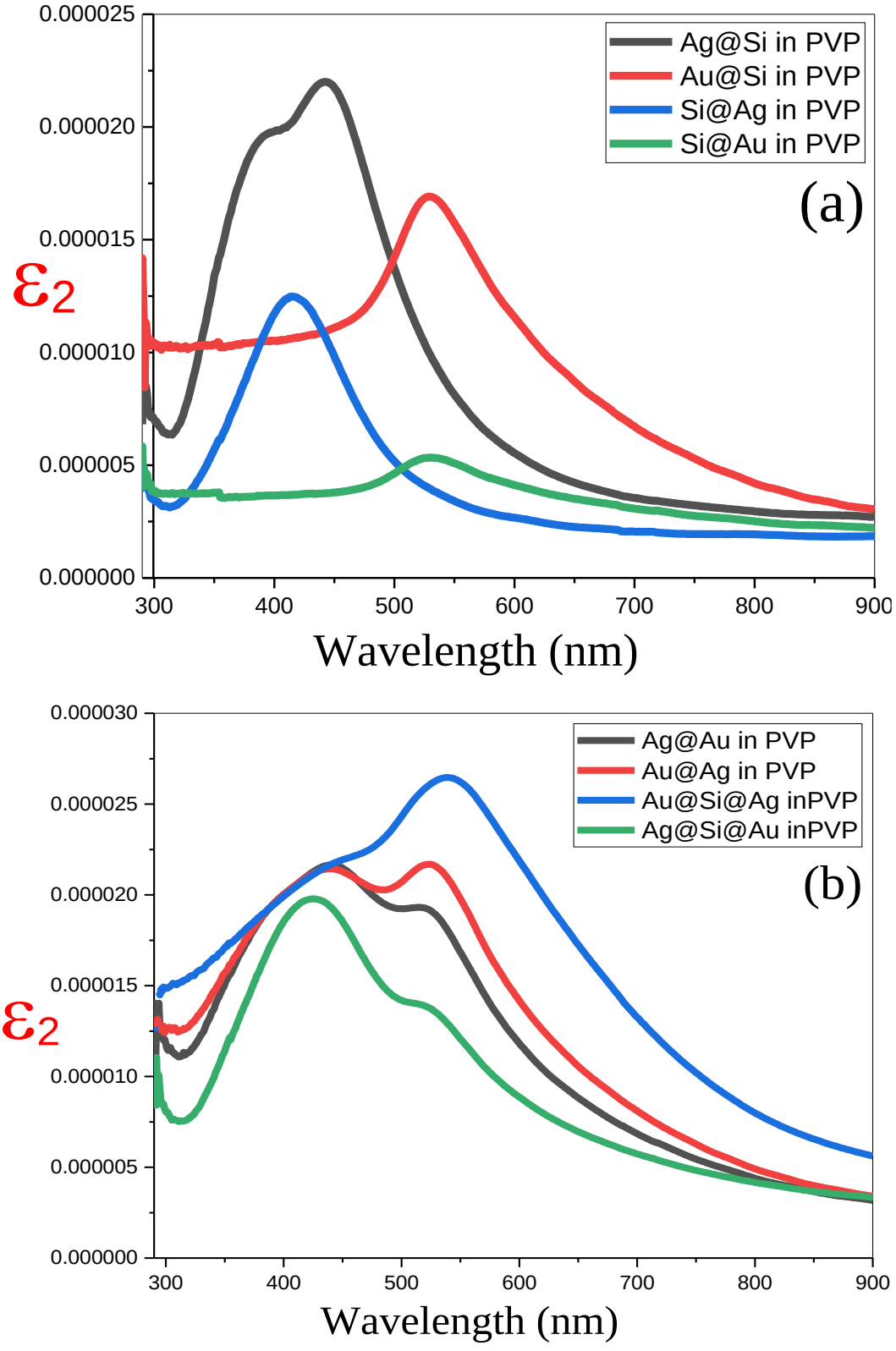


***Fig (4-7) the imaginary dielectric coefficient as a function of wavelength in the matrix of the PVP polymers for the samples; a) the M/S core/shell NPs, b) the M/M and the M/S/M core/shell NPs.***

### 4.2.5 The Results of Thermal Imaging Camera

According to the results, the enhancement in the properties, wavelength shift, and tunability in position of the SPR is very important for the study of the thermo-plasmonic properties of the proposed nanosystem in this study. However, the thermal behavior of metallic NPs are defined by their ability to absorb light and convert it into heat. In other words, for the purpose of investigation a high light-to-heat conversion efficiency by the remote control of heating by external irradiation. Consequently, by applying a suitable illumination, it is proportional to the plasmonic absorption of the nanomaterial. Several previous studies reported that the heat generation depends on the shape and the size of NPs, as well as the number of NPs in the sample and also the type of material, as increasing the number of NPs in the sample improves its thermal response to light [177].

The temperature of the nanostructure for all samples that irradiated by laser has been monitored by using a high-resolution thermal camera from the experimental point of view at room temperature. The aim is looking for a new opportunity in the thermo-plasmonics field by exploiting the different applications for nanomaterial technology in advanced biomedical applications. Besides, from the thermal camera images, can clearly see the quartz cell position has a temperature higher than the surrounding medium, as in Fig (4-8).

It is evident from this result, the nanosystem suggested in this work, which have the ability to absorb light and generate thermo-plasmonic and heat up the surrounding medium under laser lighting, this result is very similar to Ref [178].

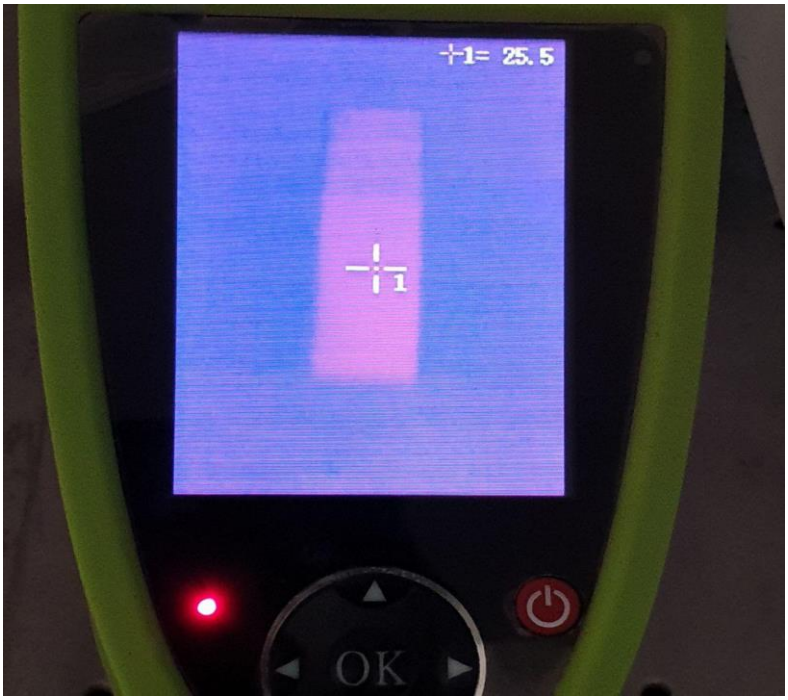


***Fig (4-8) the thermal images recorded by thermal camera at room temperature for the Si@Au NPs in the PVP.***

Furthermore, the thermo-plasmonic technique is mainly primarily based of the photo-thermal effect induced by a focused laser beam that remotely generates a confined temperature field at the desired position with high controllability among the laser parameters, such as the wavelength of laser, intensity, pulse width, and illumination time. With the possibility of changing these parameters to achieve the desired thermal effect [178,179].

The results of the temperature elevation for the bare gold, silver and silicon NPs under 30 mw CW laser illumination at different wavelengths (405, 473, 532nm) are presented in Fig (4-9).

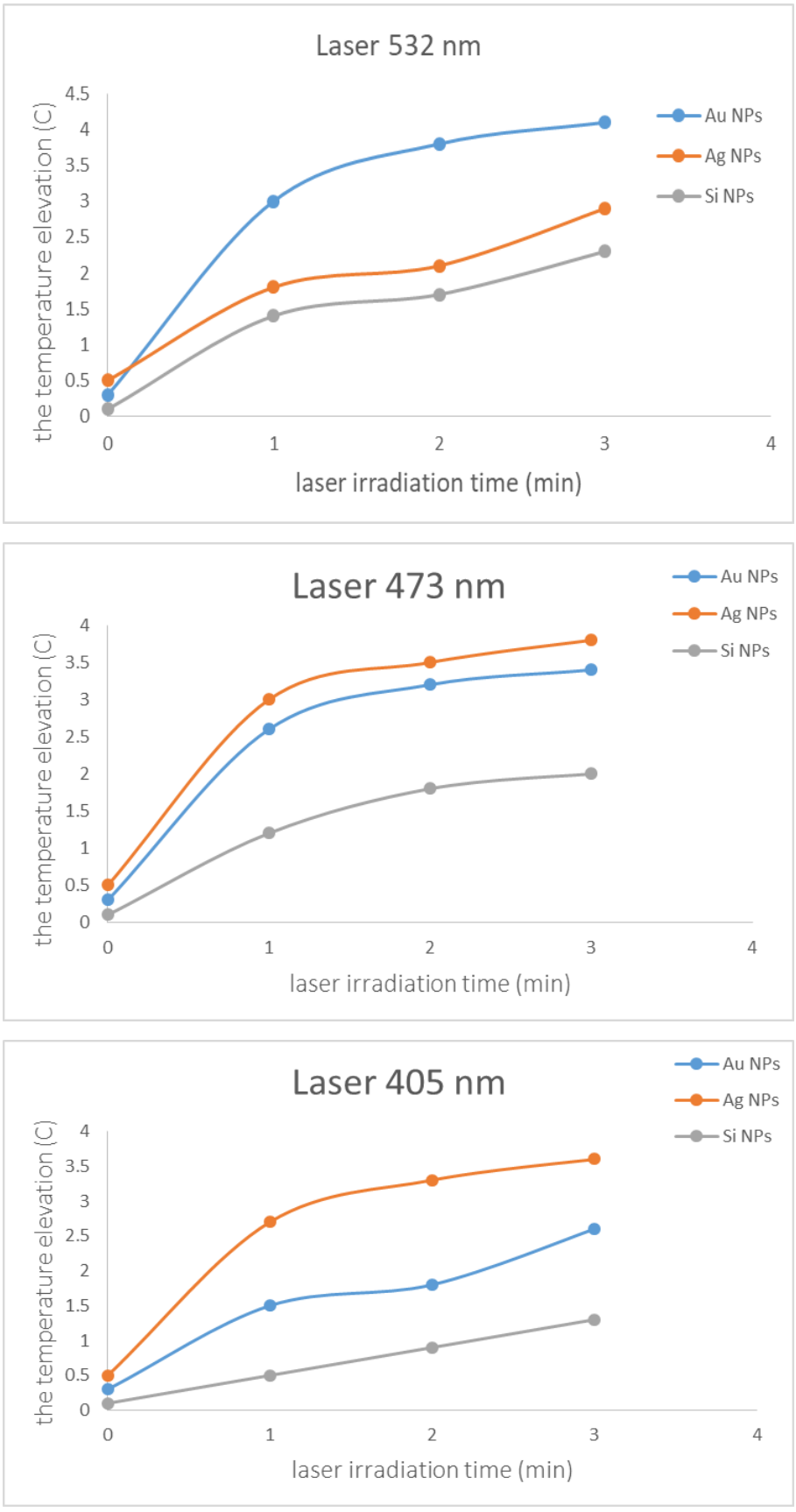


***Fig (4-9) the experimental heat generation by (405,473, and 532 nm) 30 mW CW laser illumination of the bare samples in this study.***

The results for the bare nanoscale samples are as follows, for the Au NPs sample that temperature rises by ΔT = 2.6 °C, 3.4 °C, and 4.1 °C under 30 mW the laser lighting for 3 minutes at wavelengths 405nm, 473nm, and 532nm respectively. Correspondingly, the Ag NPs sample for the lasers influence of heat up (ΔT = 3.6 °C, 3.8 °C, and 2.9 °C) under 30mW 405nm, 473nm, and 532nm the lasers influence respectively. While the photo-thermal results of the Si NPs sample were by a high (ΔT = 1.3 °C, 2 °C, and 2.3 °C) under the influence of the same lasers above, the results are presented in Table (4-2).

It is clear from these results that the wavelength of the laser used in irradiation when it is close to the absorption edge of the noble metal, which leads to an improvement in the plasmonic properties, thus a greater thermal response, this does not apply to the Si NPs sample, as it is a non-plasmonic material, which leads to not being heated.

The Fig (4-10) represents the results of the temperature elevation for the C/S NPs samples under 30 mw CW laser illumination at different wavelengths (405, 473, 532nm), it is clear from the figure that the silicon NPs make as a shell with the noble metal NPs as a core leads to the enhancement of the plasmonic phenomenon, which leads to the absorption of laser light more than from the state of bare NPs, thus the enhancement of thermo-plasmonic of the samples.

On the other hand, when the silicone as a core with noble metal shell leads to the enhancement of the plasmonic phenomenon when compared with the bare NPs, this is done by increasing the size of the NPs, which makes it vibrate with the applied field more freely.

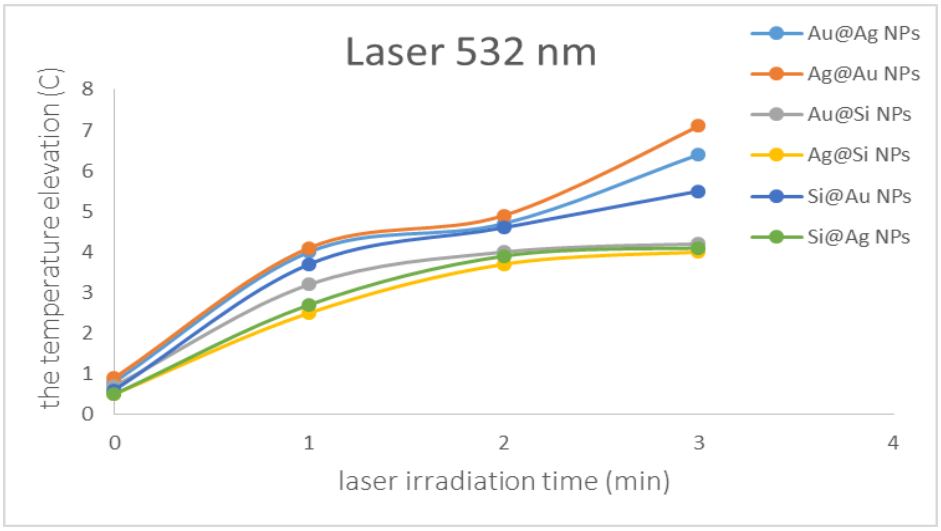


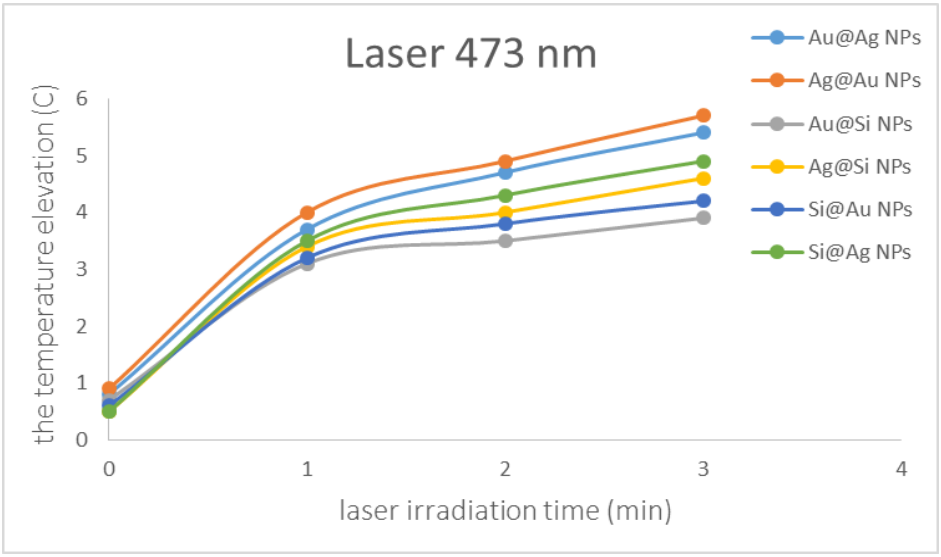


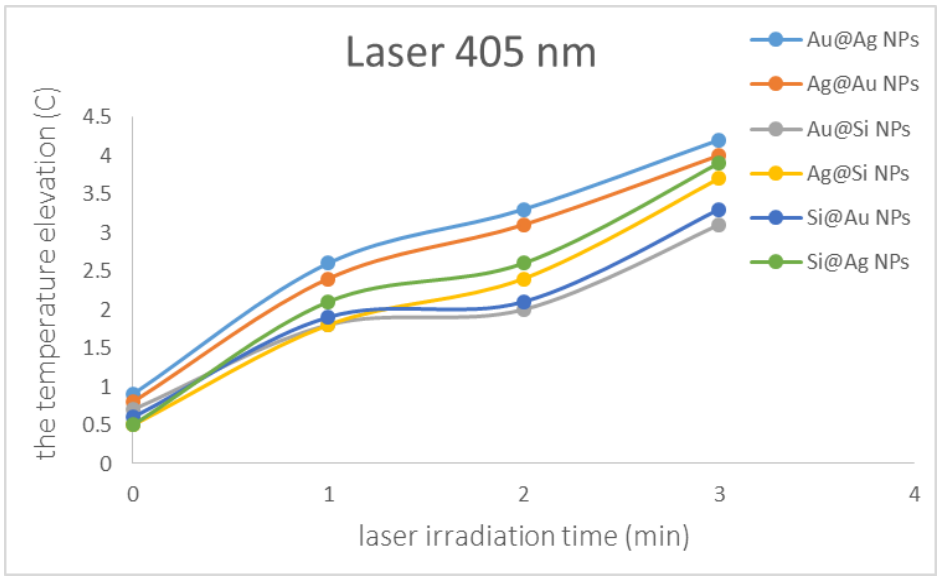


***Fig (4-10) the experimental heat generation by (405,473, and 532 nm) 30 mW CW laser illumination of the C/S samples in this study.***

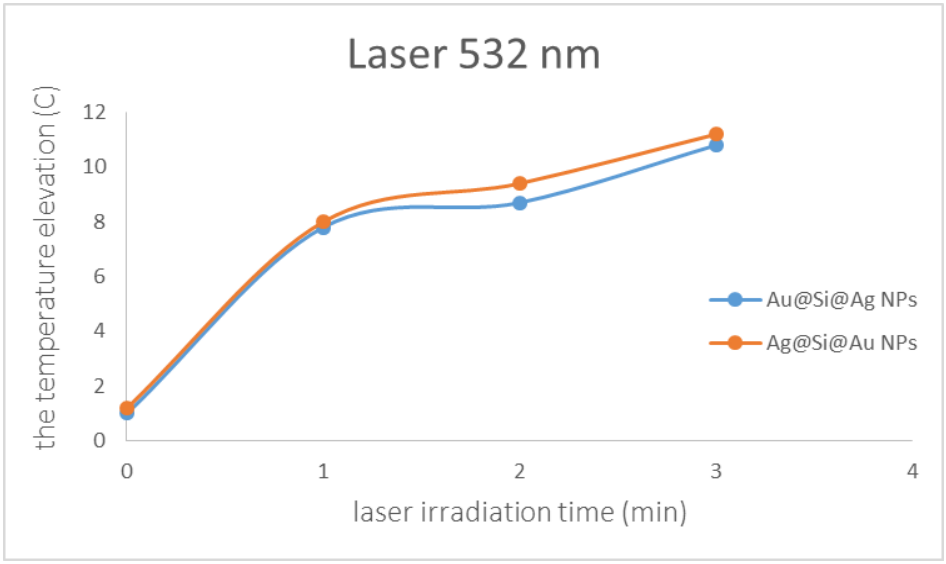


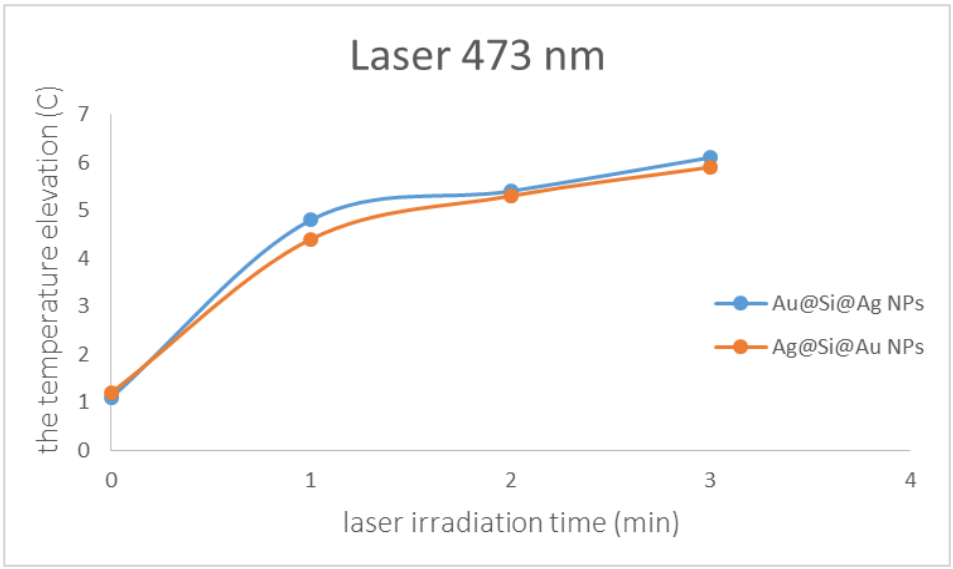


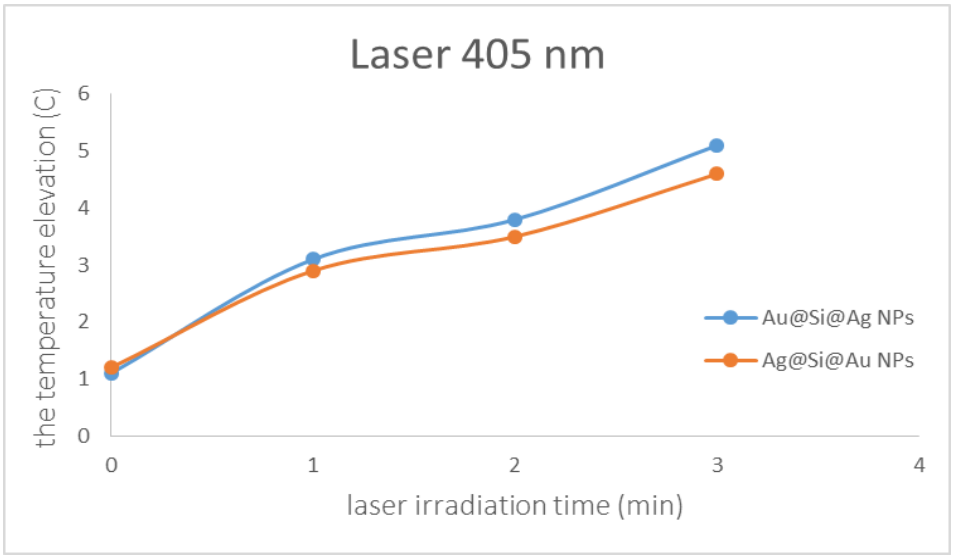


***Fig (4-11) the experimental heat generation by (405,473, and 532 nm) 30 mW CW laser illumination of the C/M-S samples in this study.***

When silver NPs is combined with gold NPs, two peaks in the absorption spectrum presented, as well as an increase in the absorption edge, thus obtaining an enhanced thermo-plasmonic. This is evident from the results of the temperature elevation of the C/S NPs which are explained in the Table (4-2).

Moreover, it can be clearly observed from Fig (4-11) that the Au@Si@Ag C/M-S NPs samples that temperature rises by ΔT = 7.4 °C, 7.1 °C, and 6.9 °C under laser lighting the 30 mW 405nm, 473nm, and 532nm respectively. Correspondingly, the sample of the Ag@Si@Au C/M-S NPs sample heat up by ΔT = 6.3 °C, 6.6 °C, and 8.2 °C, under the influence of the same lasers above.

***Table (4-2): the temperature elevation for all samples under 30 mW laser of the different wavelengths.***

| The temperature elevation for all samples (°C) | | | |
|---|---|---|---|
| The samples | The wavelength of laser | | |
| | 405 nm | 473 nm | 532 nm |
| Au NPs | 2.6 | 3.4 | 4.1 |
| Ag NPs | 3.6 | 3.8 | 2.9 |
| Si NPs | 1.3 | 2 | 2.3 |
| Au@Si NPs | 3.1 | 3.9 | 4.2 |
| Ag@Si NPs | 3.7 | 4.6 | 4 |
| Si@Au NPs | 3.3 | 4.2 | 5.5 |
| Si@Ag NPs | 3.9 | 4.9 | 4.1 |
| Au@Ag NPs | 4.2 | 5.7 | 6.4 |
| Ag@Au NPs | 4 | 5.4 | 6.5 |
| Au@Si@Ag NPs | 7.4 | 7.1 | 6.9 |
| Ag@Si@Au NPs | 6.3 | 6.6 | 8.2 |

Experimentally, the temperature elevation of Ag@Si@Au NPs was higher than Au@Si@Ag NPs under 532 nm laser illumination, because the Au has a high absorption of the SPR peak is close to the excitation wavelength of the laser, lead to more heat diffusion when is a shell. While the Au@Si@Ag NPs sample is heat absorbs from 405 nm laser more than others, because the surface plasmon excitation region is close to the wavelength of 405 nm laser.

In order to compare all of the samples, some plots were drawn, as shown in Fig (4-12). We conclude that C/M-S NPs have a higher temperature than the C/S NPs, and this in turn has a higher temperature than bare NPs. Besides, the results show that C/S NPs samples produce more heat than individual bare NPs samples, due to the redistribution of an electron/hole pair in the M/S interfaces that leads to the height of the Schottky barrier in the C/S samples [174,180]. These changes depend on the boundary conditions between the core and the shell for the samples.

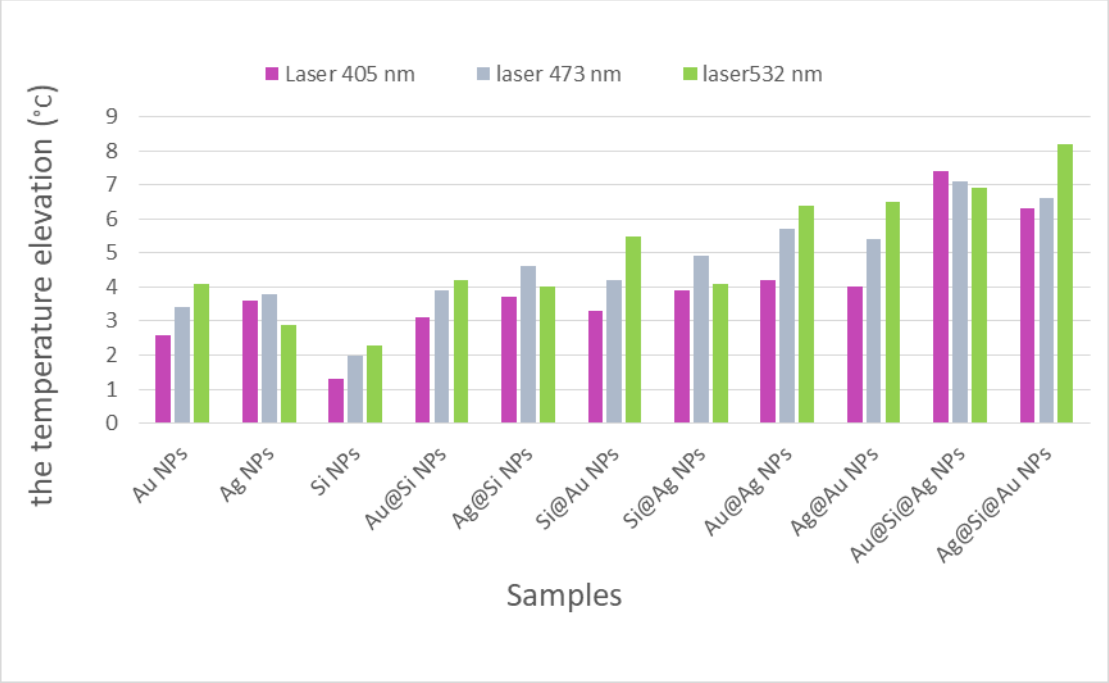


***Fig (4-12) the experimental heat generation by 30 mW CW laser (405,473, and 532 nm) illumination of all samples in this study.***

### 4.2.6 The Results of Antibacterial Activity

The findings demonstrated that a temperature elevation was encouraging for the use of the C/M-S NPs samples for thermo-plasmonic applications in living tissues, despite the fact, so various previous studies pronounced that a temperature elevation in living tissues required a range over 3–13 °C [178]. As a result, the C/M-S NPs proposed in this study have the potential to be used in cancer treatment and other biomedical applications, including antibacterial activity.

Through investigation of the antibacterial effects of the proposed nanosystem by testing the mean diameter of the inhibition zones (DIZ) (mm in diameter) for the C/M-S NPs samples under laser illumination, depending on the compatibility between the wavelength of the laser used in samples irradiation with the SPR position of the nanostructures. Here thermo-plasmonic plays a major role in determining the effectiveness of NPs to inhibit bacterial growth, which in turn leads to the transfer of heat from the nanostructures to the surrounding areas, thus inhibiting the growth of bacteria. The thermo-plasmonic lead to the rupture of bacterial membranes due to the increase in temperature upon irradiation by the laser. Thus, protein denaturation and permanent damage for bacterial cell, then autolysis and death of cells [150, 151].

The effectiveness of the C/M-S NPs against the E-coli bacteria increases as the laser irradiation on petri-dish containing bacteria and NPs increases. The DIZ depends on the wavelength of the laser irradiation. Can be noticed that the diameter of the inhibition zone increases when the wavelength of the laser used for irradiation is close to the SPR of the shell NPs of the sample used by inhibition. The DIZ are explained in Table (4-3) for all wavelengths used in this work.

In addition, when observing zones of inhibition a significant increase in the DIZ were observed in irradiated laser wells when compared to non-

laser irradiated wells. This increase proves the effect of thermo-plasmonics on the inhibitionzation of bacteria. The behavior is shown in Fig (4-13).

In general, there are several scenarios that lead to bacterial cell death, such as adhesion of the nanomaterial to the cell wall, Reactive Oxygen production, inhibition of biofilm formation, and interaction of the nanomaterial with DNA and/or proteins the bacterial cell [151-154].

In this work , the likelihood of death the bacterial cells is due to the synergistic effect and the interaction between the C/M-S NPs and the bacterial cell membrane leads to the adhesion of the proposed nanosystem to the cell wall, thus the penetration of the cell membrane and the production of Reactive Oxygen Species. In addition, the areas around the wells are getting heated up because of the thermo-plasmonic which led to the disintegration, death and extermination of bacterial cells.

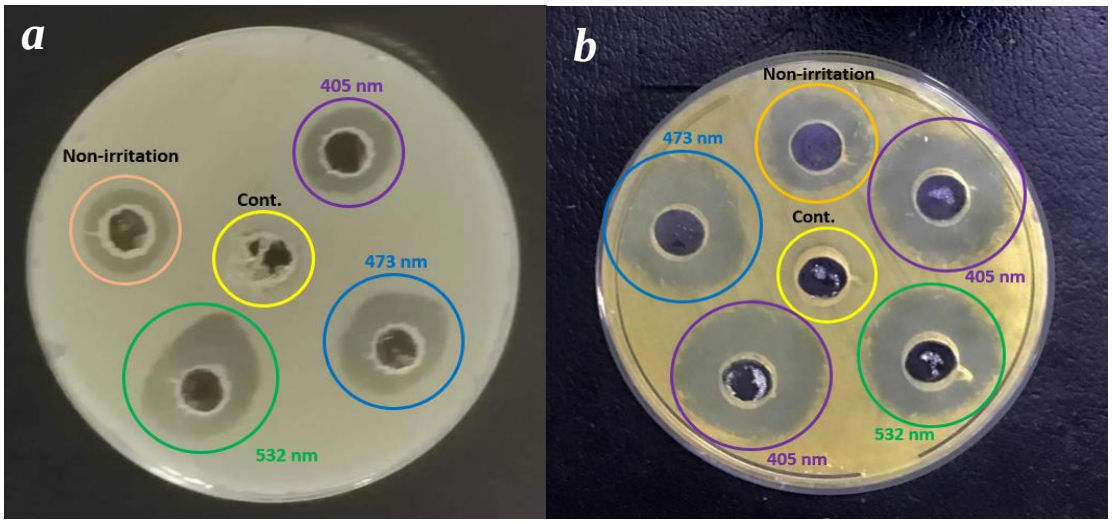


***Fig (4-13) the petri dishes photos containing the E. coli with the C/M-S NPs under the influence of the laser radiation 30 mW of different wavelengths (405, 473, and 532nm) for 5 min ; a) the Ag@Si@Au NPs as the anti-bacterial, and b) the Au@Si@Ag NPs as the anti-bacterial.***

***Table (4-3) Antibacterial activity of C/M-S NPs under laser radiation against the E-coli bacteria by the DIZ.***

| Zone of inhibition (mm) | | | | | |
|---|---|---|---|---|---|
| The samples | control | non-irradiated | 405nm | 473nm | 532nm |
| Ag@Si@Au NPs | - | 2 | 3 | 4 | 6 |
| Au@Si@Ag NPs | - | 4 | 8 | 7 | 5 |

## 4.3 The Simulation Results

Based on Drude-Lorentz model and heat transfer model, COMSOL multi-physics program is used to estimate the heat generated and transferred from spherical the core/shell NPs that illuminated by (532 nm for the Au shell, and 405nm for the Ag shell) 30 mwatt CW laser in the surrounding of the PVP polymer matrix. as well as benefit from the FEA method to understand the behavior of the optical absorption of appreciate the wavelength shift when changing the core size and the shell thickness. In addition to using the FDM method to determine the electronic transport of the electric charges at the boundary of nanoparticles.

### 4.3.1 Optical Results of the Finite Element Analysis

The numerical results of the optical absorption behavior have been calculated by the FEA method, which depends on the permittivity of materials using experimental optical properties. The simulation results are displayed in Fig (4-14) for the Au NPs in PVP sample, which is comparable by results of the optical linear properties in experimental section in this work. A distinguishable peaks is observed in the absorption spectra for, as shown in Fig (4-14). It can be observed that the peak intensity increases when the diameter of nanoparticles increases. Furthermore, the SPR position has a redshift from 527 nm to 540 nm in

the PVP solvent, when the diameter of nanoparticles increases from 5 nm to 30 nm, the result agrees with Ref [38].

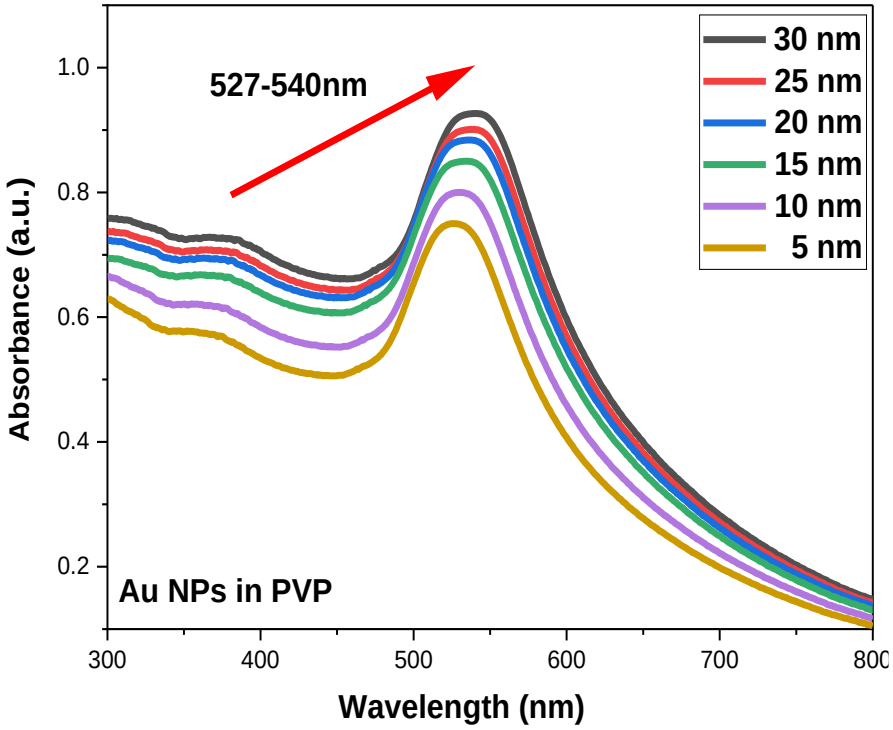


***Fig (4-14) Absorption spectra, as a function of wavelength with different size of nanoparticles of the Au NPs in PVP matrix.***

Furthermore, a multilayer particle method is used to investigate the core/shell NPs instead of single-type nanoparticles method. The suppose of the core radius is fixed (30 nm), and the change in the shell thickness (10, 15, and 20 nm), for the core/shell NPs samples in the PVP polymer matrix. It noticed of the absorption spectrum of the core/shell NPs, a clear red shift in the SPR position (from 502 to 570 nm), with different peak intensities for the Si@Au NPs sample, when changing the shell thickness, as in the Fig (4-15a). But noticed little red shift in the SPR position (from 539 to 544 nm), with different peak intensities for the Au@Si NPs sample, when changing the shell thickness, as in the Fig (4-15b).

This due to the coupling between metal/semiconductor (Au/Si NPs), as well as the electronic transport and the movement direction of the charges

at the boundary, where changes appear clearly in the absorption spectra when changing the location of the gold NPs between the core and the shell. These results are in good agreement with the experimental results.

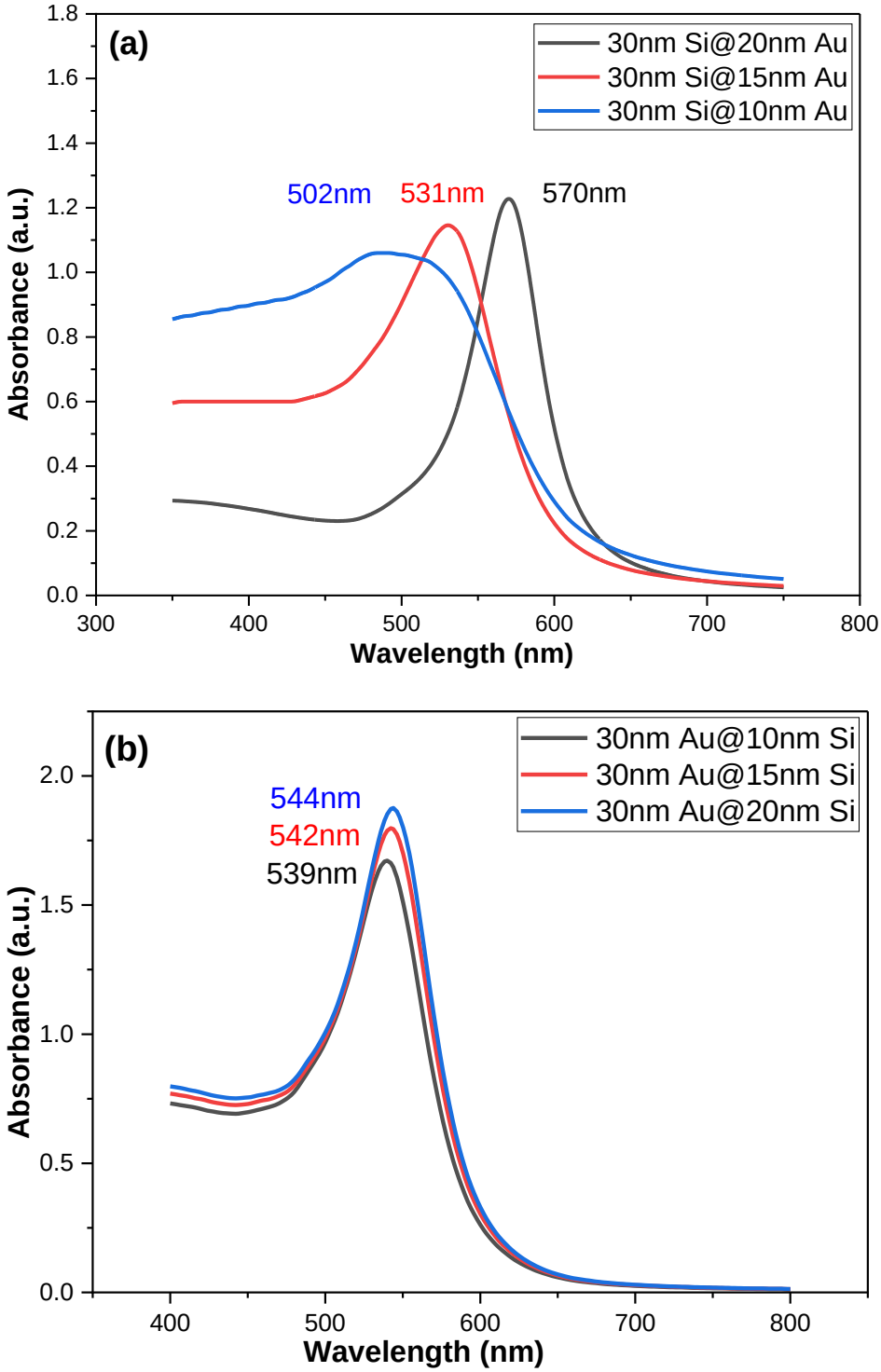


***Fig (4-15) Absorption spectra, as a function of wavelength, when core diameter 30nm, with different shell thickness; a) the Si@Au NPs, b) the Au@Si NPs in the PVP polemar.***

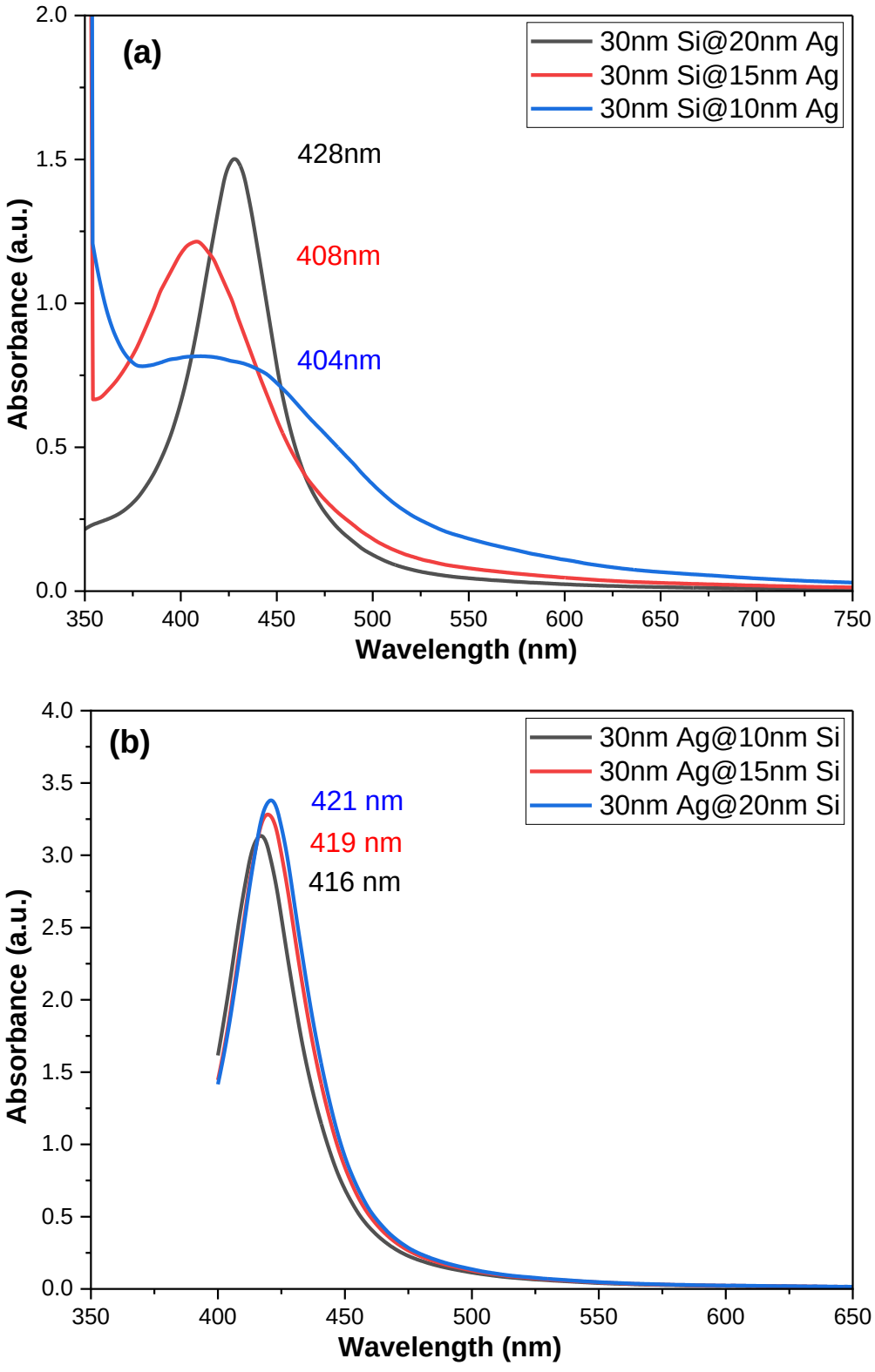


***Fig (4-16) Absorption spectra, as a function of wavelength, when core diameter 30nm, with different shell thickness; a) the Si@Ag NPs, b) the Ag@Si NPs in the PVP polemar.***

The results show that absorption peak of the Si@Ag NPs in the PVP matrix have clear red shift from 404 nm to 428 nm, with different peak intensities, when the increasing shell thickness from 10 nm to 20 nm, as in Fig (4-16a).

While the absorption peaks of Ag@Si NPs in the PVP matrix have a little redshift from 416 nm to 421 nm, with different peak intensities, when the increasing shell thickness,as in Fig (4-16b).

This result is in agreement with both the Si@Au, and the Ag@Si core/shell NPs samples, in addition to its agreement with the experimental results.

For the same reason mentioned earlier, which is the movement direction of the charges at the boundary coupling between (Ag/Si NPs).

The results indicated a considerable relationship between the present computational and experimental results in the PVP matrix. However, the FEA method can predict the experimental results exactly.

The comparison between the simulation and the experimental results for the SPR position at the 30 nm diameter of the core and the 15 nm thickness of the shell, shown in the Table (4-4).

***Table (4-4): The SPR position of the core/shell samples in PVP matrix for the simulation and the experimental results***.

| **The core/shell samples** | **The SPR position for the experimental results** | **The SPR position for the simulation results** |
|---|---|---|
| Au@Si NPs | 528 nm | 544 nm |
| Si@Au NPs | 537 nm | 570 nm |
| Ag@Si NPs | 417 nm | 421 nm |
| Si@Ag NPs | 416 nm. | 428 nm |

### 4.3.2 Results of the Temperature Detection

The metal/semiconductors nanoparticles can serve as an efficient nano-heat source with confinement photothermal effects. Thermo-plasmonic technology allows researchers to control the temperature at a nanoscale due to the possibility of precise light propagation.

The simulated program is used to estimate the temperature elevation using the real parameters that were used in the experimental work for the 30nm core size and the 10-20nm shell thickness, heating starts from the center of the sample.

The response of opto-thermal generation of the hybrid nanosystem consisting of Au/Si and Ag/Si core/shell NPs immersed in the PVP polymer matrix is theoretically investigated. Two lasers (CW 30 mwatt) at the plasmonic resonance (532nm and 405 nm) are utilized. The simulation results by COMSOL multiphysics showed that the illumination of the samples by varying shell thickness, the heat dissipation as a function of distance from the center of nanoparticles depends on the shell thickness and the laser power that used in illumination process.

The results showed that changing the shell thickness from 10-20 nm leads to an increase in the temperature of the Au@Si NPs sample from 20 $C^{\circ}$ to 22.84 $C^{\circ}$, while the temperature of the Si@Au NPs sample increased from 20 $C^{\circ}$ to 25.83 $C^{\circ}$ under the irradiation of the 532nm laser, as shown in Fig (4-17) and Fig (4-18).

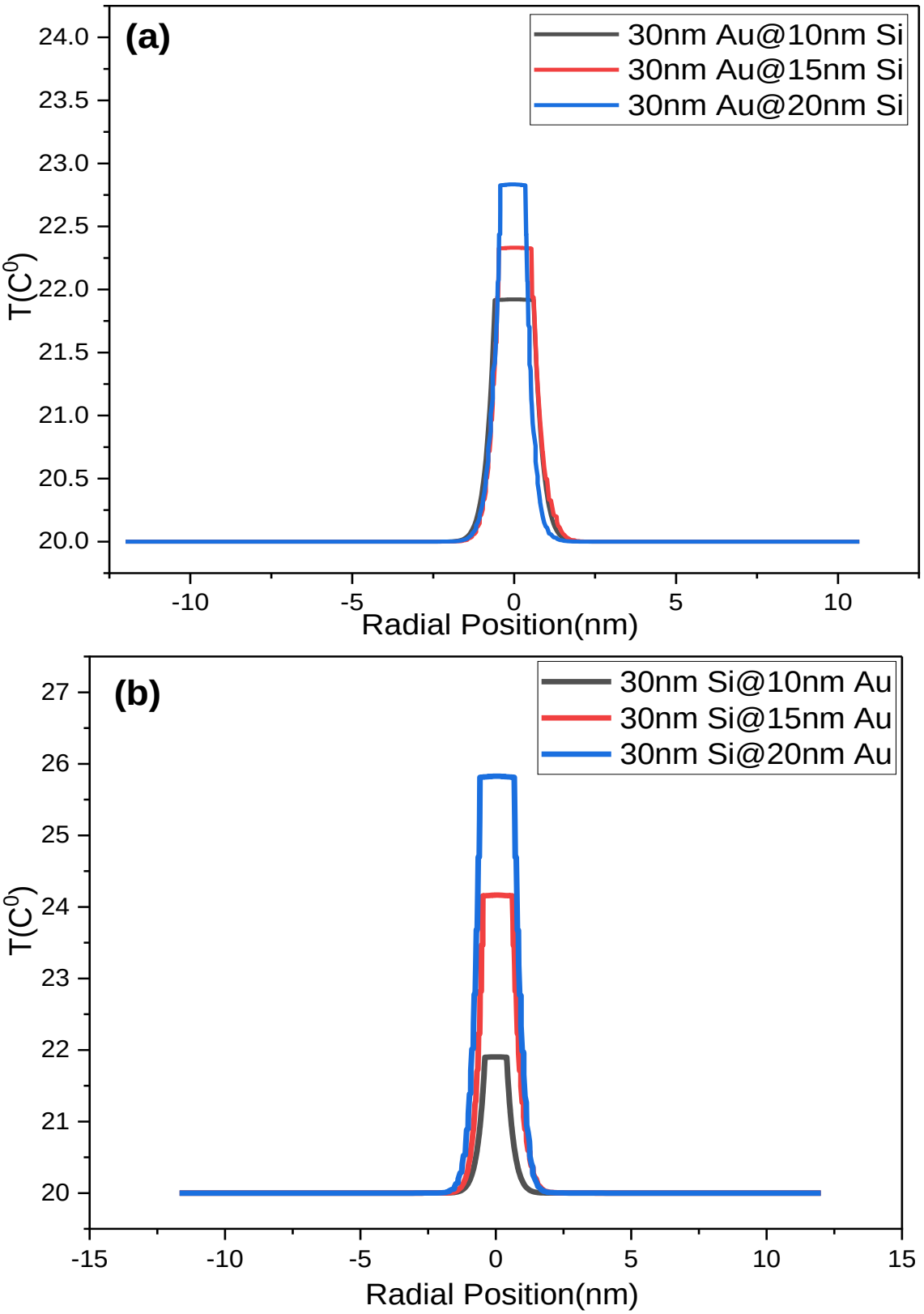


***Fig (4-17) the simulated heat generation by 30 mwatt CW, 532 nm laser illumination of the samples; a) the Au@Si NPs, b) the Si@Au NPs.***

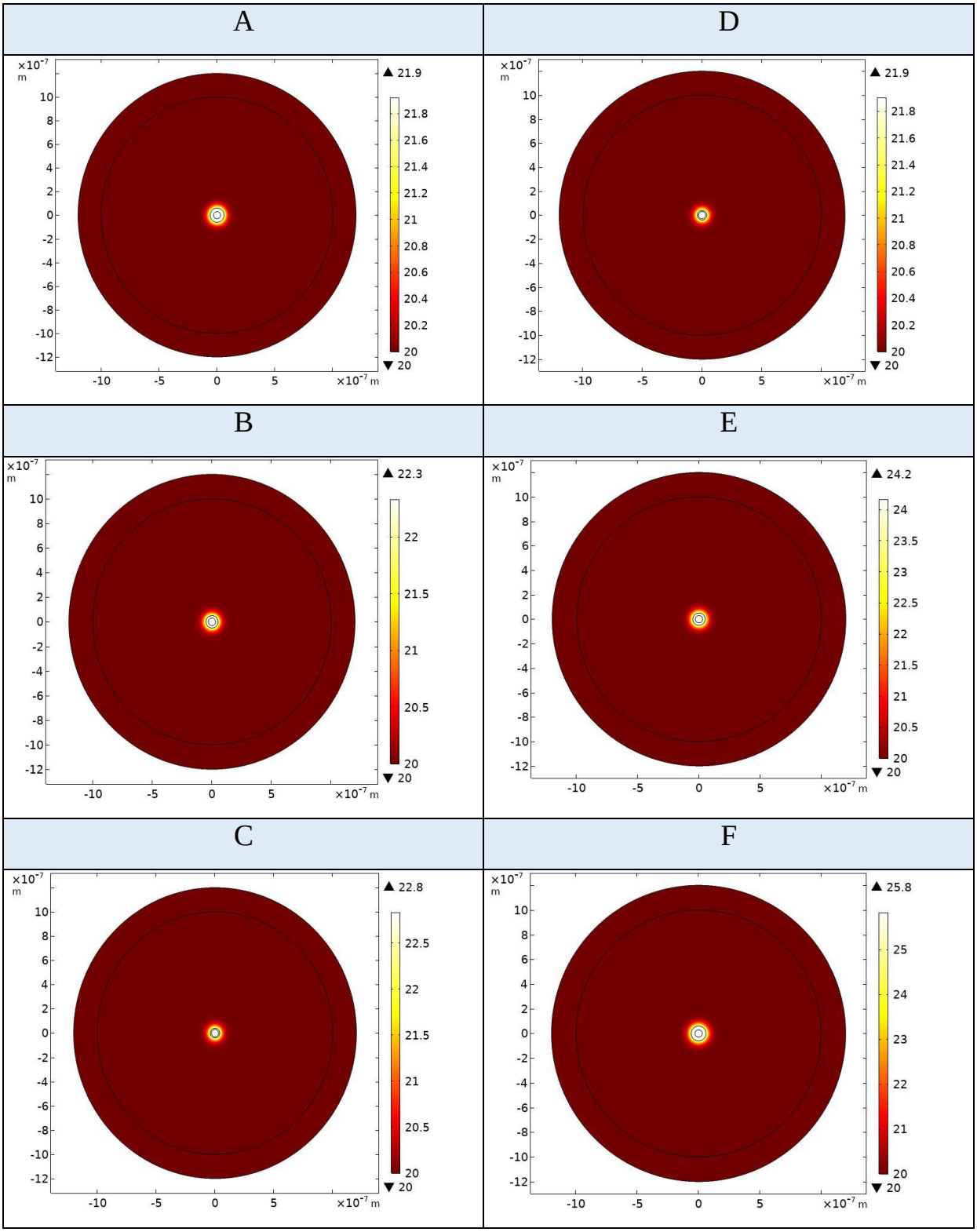


***Fig (4-18) The simulation images of the heat dissipation as a function of distance from the center of the Au@Si core/shell NPs at the Au core 30 nm is fixed; a) the Si shell 10 nm, b) the Si shell 15 nm, and c) the Si shell 20 nm. And the Si@Au core/shell NPs at the Si core 30 nm is fixed; d) the Au shell 10 nm, e) the Au shell 15 nm, and f) the Au shell 20 nm.***

The heat power distribution when the laser operates at wavelength 405 nm using the 30nm core size and the 10-20nm different shell thickness, the obtained results are shown in Fig (4-19) and Fig (4-20) for the Ag@Si NPs and the Si@Ag NPs samples. The increase in the temperature of the Ag@Si NPs sample from 20 $C^{o}$ to 21.88 $C^{o}$, while the temperature of the Si@Ag NPs sample increased from 20 $C^{o}$ to 24.92 $C^{o}$ The simulation results using different shell thickness, we were obtaining a clear increase in temperature as a result the illumination of all samples by laser. The temperature change are reported in Table (4-5).

Based on the results, metal/dielectric core/shell nanoparticles strongly absorb light and convert into an efficient localized heat source in the presence of electromagnetic radiation at their plasmonic resonance [181]. This process can be enhanced depending on the size, shape, structure, and surrounding media.

***Table (4-5): The simulation temperature difference ( $\Delta T$ ) of the core/shell samples due to laser illumination as a function of the different shell thickness, it Compared with ( $\Delta T$ ) experimentally.***

| ***Sample*** | ***The shell thickness*** | | | $\Delta T$ ***experimentally*** |
|---|---|---|---|---|
| | ***10nm*** | ***15nm*** | ***20nm*** | |
| ***Au@Si NPs*** | 1.91 $C^{o}$ | 2.33 $C^{o}$ | 2.84 $C^{o}$ | 4.2 $C^{o}$ |
| ***Si@Au NPs*** | 1.90 $C^{o}$ | 4.17 $C^{o}$ | 5.83 $C^{o}$ | 5.5 $C^{o}$ |
| ***Ag@Si NPs*** | 1.46 $C^{o}$ | 1.65 $C^{o}$ | 1.88 $C^{o}$ | 4 $C^{o}$ |
| ***Si@Ag NPs*** | 2.05 $C^{o}$ | 2.75 $C^{o}$ | 4.92 $C^{o}$ | 4.1 $C^{o}$ |

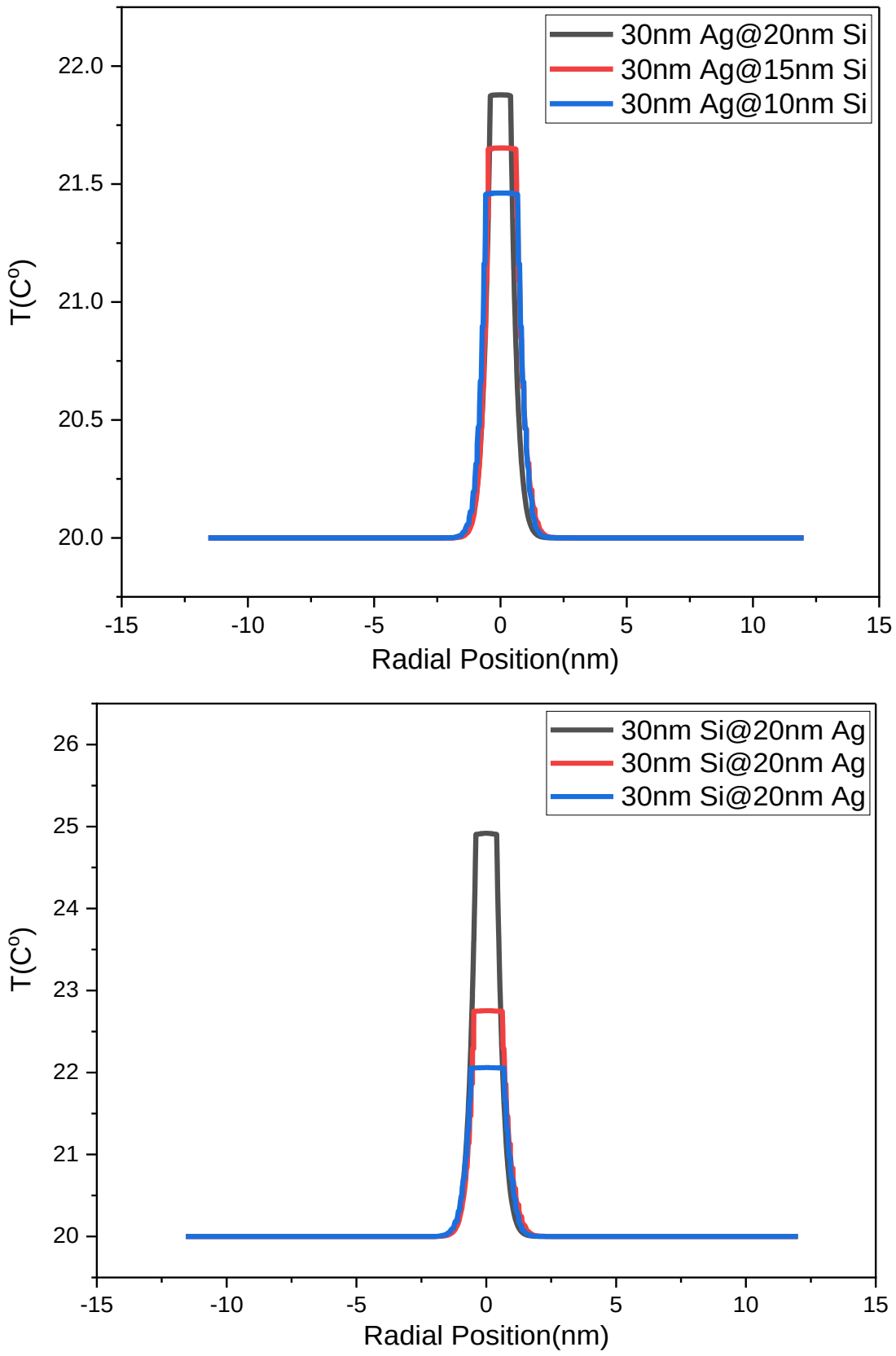


***Fig (4-19) the simulated heat generation by 30 mwatt CW, 405 nm laser illumination of the samples; a) the Ag@Si NPs, b) the Si@Ag NPs.***

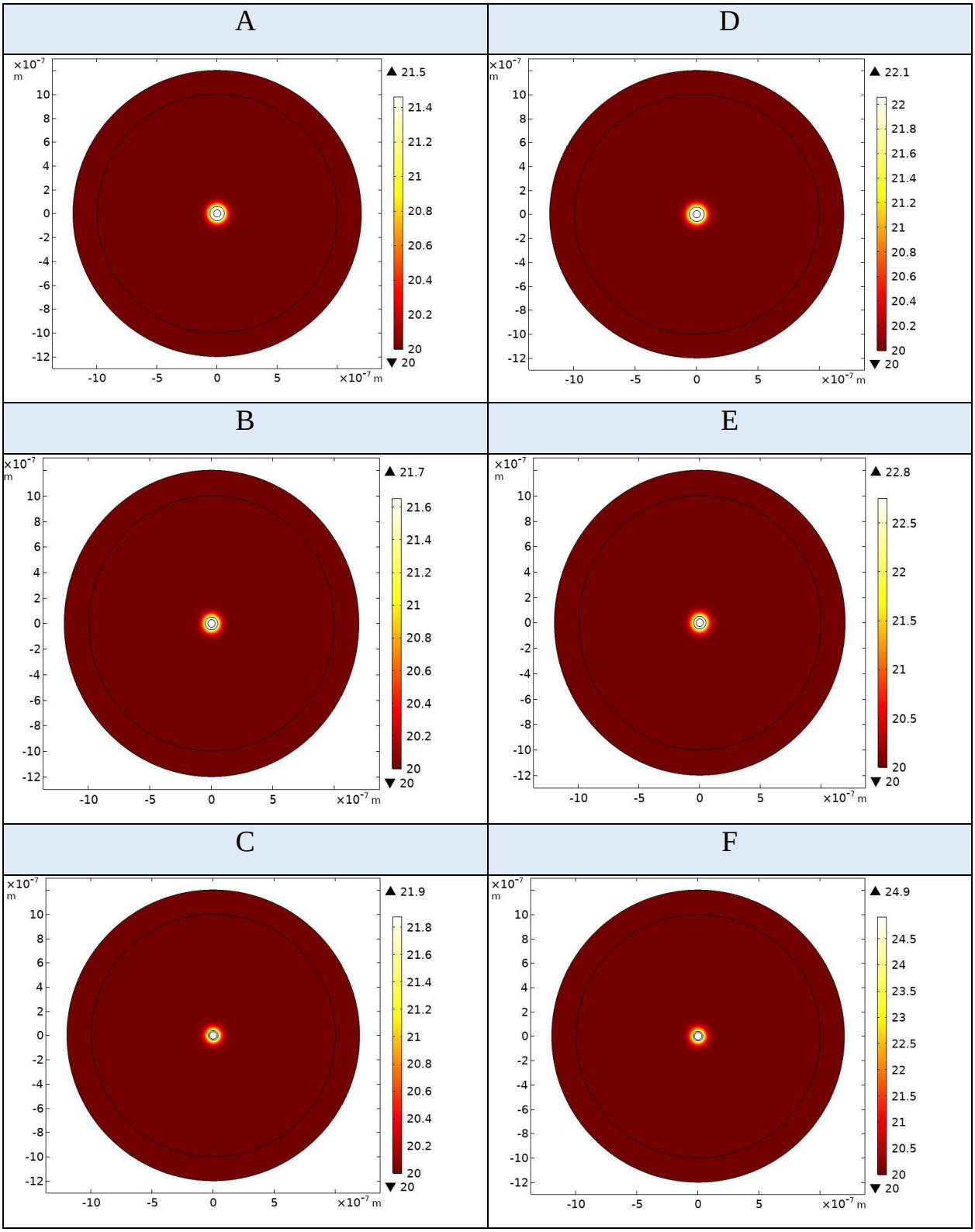


***Fig (4-20) the simulation images of the heat dissipation as a function of distance from the center of the Ag@Si core/shell NPs at the Ag core 30 nm is fixed; a) the Si shell 10 nm, b) the Si shell 15 nm, and c) the Si shell 20 nm. And the Si@Ag core/shell NPs at the Si core 30 nm is fixed; d) the Ag shell 10 nm, e) the Ag shell 15 nm, and f) the Ag shell 20 nm.***

### 4.3.3 Results of the surface electric-field distribution on the boundary between nanoparticles interface

The electric charge distribution of the bare nanoparticles (Au, Ag, and Si) showed from the Fig (4-21), the red arrows represents the direction of movement of the charges. The bare nanoparticles with size 30 nm immersed in the PVP polymer matrix. It is clearly shown that the charges are concentrated on the surface of the metallic gold and silver nanoparticles and their density increases at the boundary with the surrounding due to the SPR phenomenon. While the electric charge is concentrated inside the silicon nanoparticle and decreases on the surface as it is a non-plasmonic material, to clearly understand see the Fig (4-22).

For the core/shell nanoparticles, the distribution of electric charge is spread inside the shell layer, it leads to an improvement in the intensity of the electric field in the shell layer, and this enhancement can be noticed when compared with the bare nanoparticles, as a the Fig (4-23).

When comparing the four samples in the Fig (4-23) for the core/shell NPs together, an improvement in the electric field can be clearly observed when the metallic nanomaterial is in the core, as in the Au@Si and the Ag@Si samples. While the width of the charge distribution area increases, but with less intensity for the Si@Au and the Si@Ag samples. This decrease in intensity is due to the distribution of the surface plasmon field over two regions at the boundary between the metal and the semiconductor, as well as the boundary between the metal and the environment, as in the Fig (4-24).

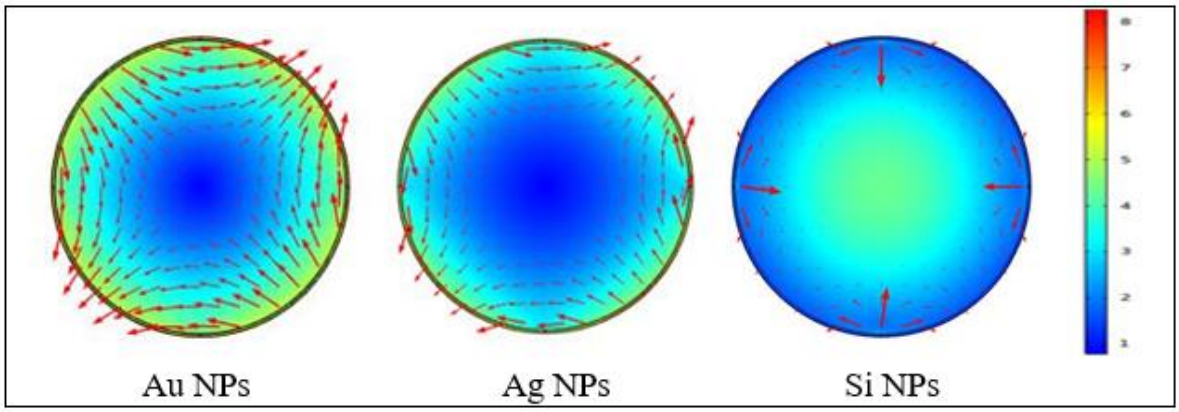


***Fig (4-21) the electric charge distribution of the bare nanoparticles immersed in the PVP polymer matrix.***

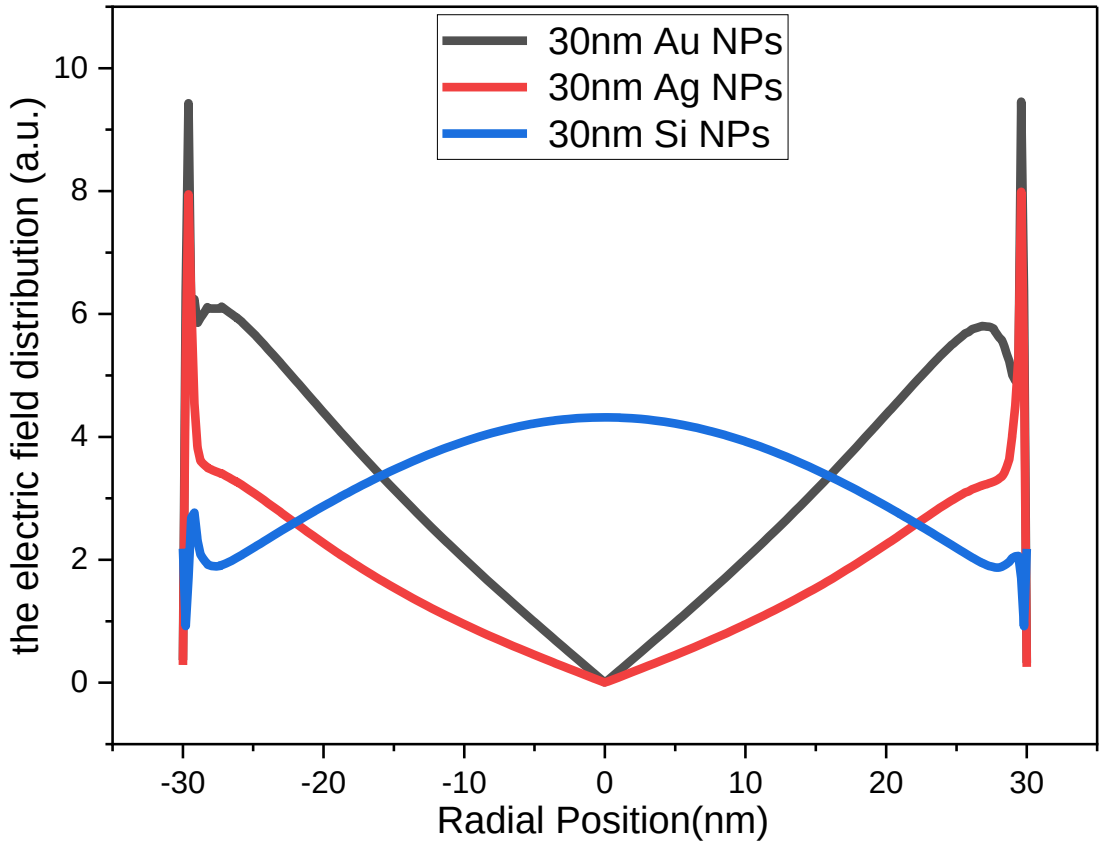


***Fig (4-22) the electric charge distribution of the bare nanoparticles immersed in the PVP polymer matrix as a function of the radial position.***

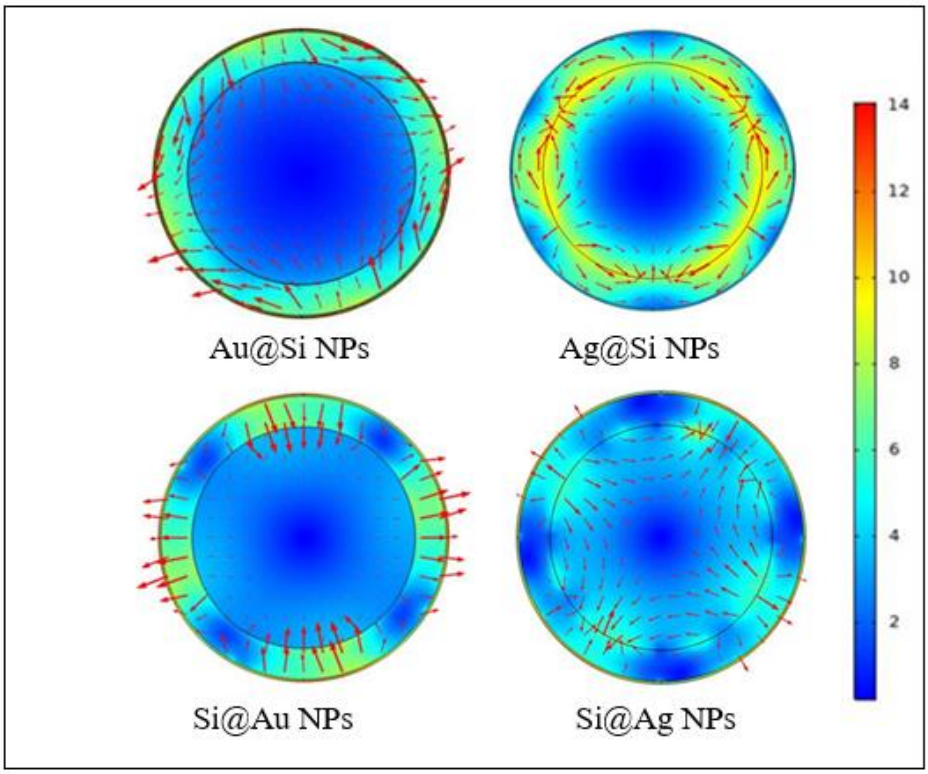


***Fig (4-23) the electric charge distribution of the core/shell nanoparticles immersed in the PVP polymer matrix.***

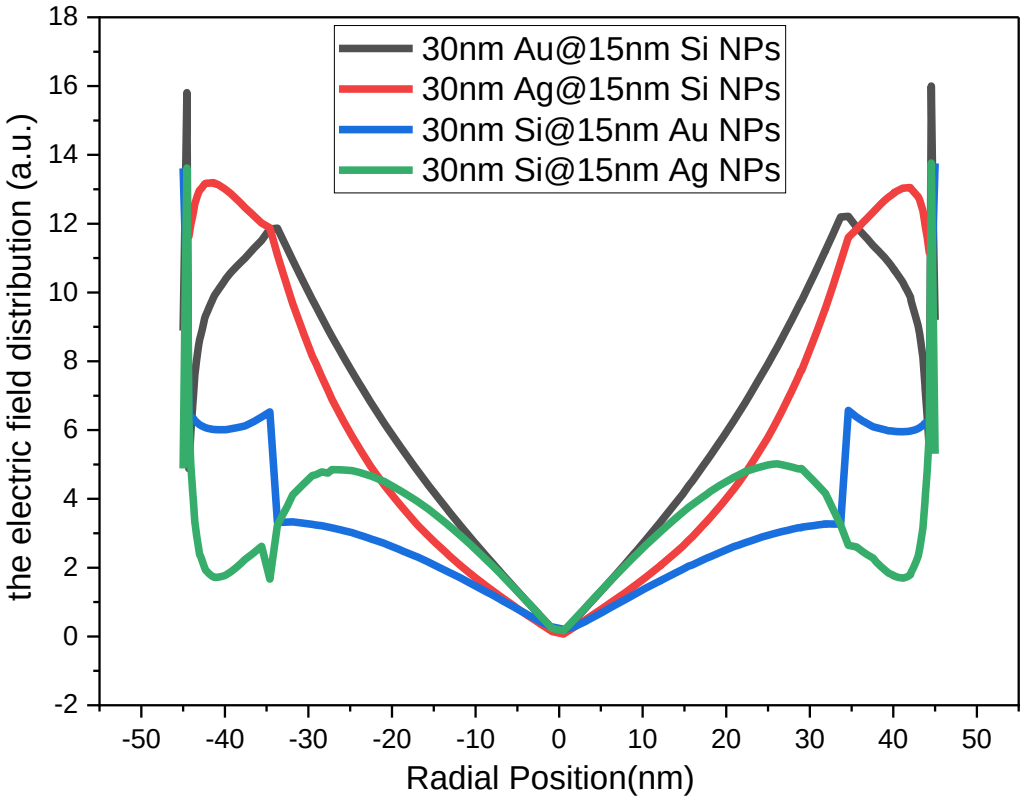


***Fig (4-24) the electric charge distribution of the core/shell nanoparticles immersed in the PVP polymer matrix as a function of the radial position.***

In addition, the density of the electric charge increases clearly for the core/multi-shell nanoparticles when compared with the core/shell nanoparticles, this is due to the SPR appears in three areas between the core and the first shell, as well as between the first and second shells, and also between the outer shell and the environment, as in the Fig (4-25).

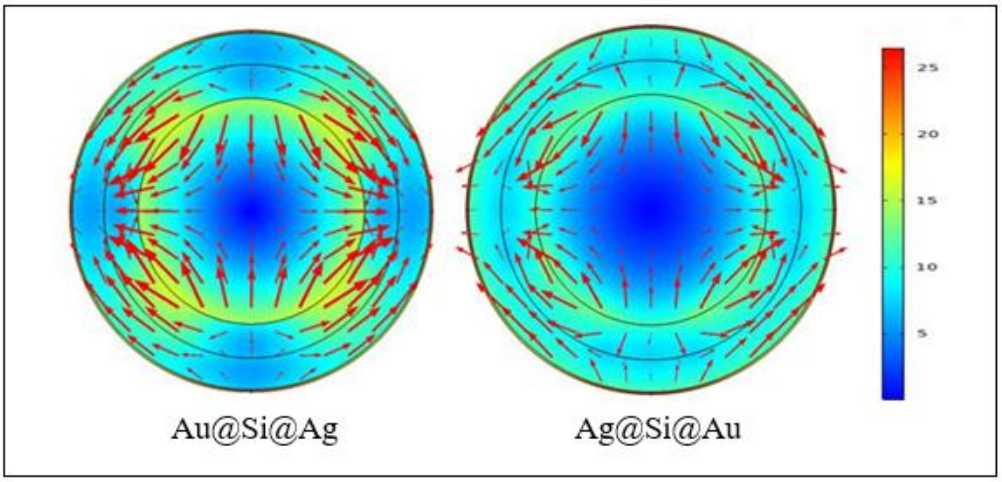


***Fig (4-25) the electric charge distribution of the core/multi-shell nanoparticles immersed in the PVP polymer matrix.***

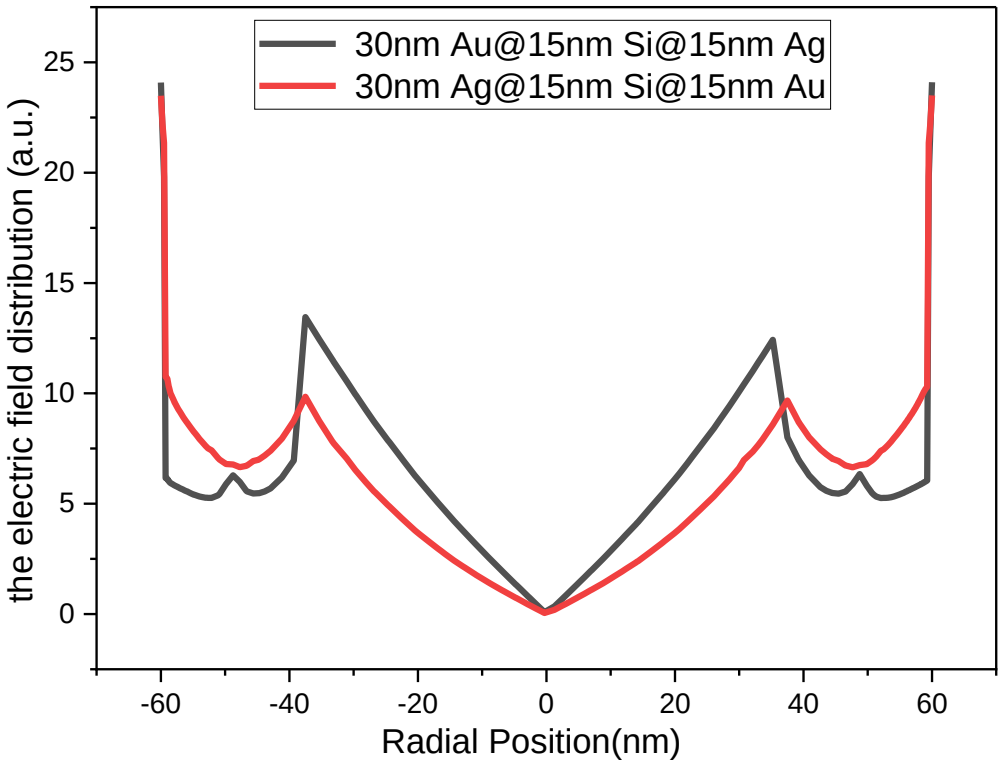


***Fig (4-26) the electric charge distribution of the core/multi-shell nanoparticles immersed in the PVP polymer matrix as a function of the radial position.***

It is evident from the Fig (4-26) that the Au@Si@Ag NPs sample has the electric charge density more than the Ag@Si@Au NPs sample,due to the dielectric properties of Au@Si@Ag ,The results showed that the local distribution of the electric field depended on size and structure the core/shell nanoparticles.

In addition, one of the important issues in our work is investigate the interface physical phenomena such as the height of the Schottky Barrier at the boundary between metals and semiconductors. It to a great extent defines the current transport and the potential distribution through these interfaces, and consequently the usefulness of the electronic devices[182]. When the sample is irradiated with the visible light, within the energy gap of semiconductor such as the laser light are irradiated on the samples Au/Si and Ag/Si, lead to, absorption of photons as, the generates an electric field at the Schottky Barrier forcing the photo-generated electrons ($e^-$) and holes ($h^+$) to isolate in opposite directions. When the metal/Si NPs is irradiated with light, the electrons in the valance band of Si come to be excited to the conduction band. Since the fermi energy of the metal is at a lower level than the Si conduction band, hence the Au inter bands capture the electrons from Si. Thus, the Au layer acts as the reservoir for the electrons and prevents the fast recombination of photo excited the electrons and the holes in the semiconductor [183,184]. This leads to increases in the absorption coefficient and thus nanoparticle heat and thus in the SPR sample quantities. This work will give some idea to those interested in scientific research for the more advancement of photo-thermo-plasmonic effects.

## Conclusions

This study proved that the hybrid NPs (the core/shell and the core/multi-shell) can be successfully produced by using the pulsed laser ablation in liquid method.

In addition, this study proved that the Au/Si/Ag nanostructures proposed in this work can be used as a nano-heat source in biomedical applications, by utilizing the thermo-plasmonic feature. Accordingly, the temperature elevation of the core/multi-shell NPs by about 5-8 $C^{o}$ was sufficient to kill and inactivate the E. coli bacteria under different wavelengths of laser irradiation.

Moreover, the results show the exhibit extremely agile tunability in position of the SPR, and also the local distribution of the electric field and thermo plasmonic propreties for each set of NPs that is may be useful in the design of optical absorption devices and bio-medical applications.

Furthermore, the core/multi-shell NPs proposed in this study have an encouraging results to use it as a nano-heat source in biomedical applications, and they are promising candidates for the cancer treatment.

Besides, the simulation results match well with the experimental results, this confirms that the finite element method from COMSOL multi-physics can describes the results very closely to the experimental results.

Therefore, the results can open new insights for researchers to improve thermo-plasmonic effects more in the photo-optical devices.

## Suggestion for Future Work

The current work can be extended as a future work in the following:-

1- Study the effect of other materials and other solvents on the synthesis of nanoparticles and compare it with the suggested materials in this work.

2- Study the effect of the external electric and magnetic field on the thermo-plasmonic properties for the samples proposed in this work.

3- Study the synthesis of different nanostructures such as core/shell nanostar, and core/shell nanorod.

4- Study the effect of thermo-plasmonic in infrared region.

5- Studying the inhibiting ability of the proposed hybrid nanostructures in this work as antibacterial and antifungal on other pathogenic bacteria and fungi.

6- Investigate the means of core/shell nanoparticle delivery into the vivo body to be used as a treatment in medical field.

**List of Publications**

1- "Enhanced Thermoplasmonic Effect in Core/Multi Shell Hybrid Nanostructures", Accepted for Publication in Journal of Nanostructures, (2022).

2- "Antibacterial Photothermal Effect based on Core/Multi Shell Hybrid Nanostructures", Under Review, (2022).

3- "Enhanced Nonlinear Optical Properties of the Core/Multi Shell Hybrid Nanostructures", Under Review, (2022).

4- The Surface Electric-Feld Distribution on the Boundary between Interfaces of the Core/Multi Shell Hybrid Nanostructures", Under Review, (2022).

## References

**[1]** Kim, Minho, Jung-Hoon Lee, and Jwa-Min Nam. "Plasmonic Photothermal Nanoparticles for Biomedical Applications." *Advanced Science* 6, no. 17 (2019), 1900471. doi:10.1002/advs.201900471.

**[2]** Dai, Han, Ruiqiang Ding, Meicheng Li, Yingfeng Li, Ganghai Yang, Dandan Song, Yue Yu, and Mwenya Trevor. "Abnormal thermal effects on the surface plasmon resonance of Ag nanoparticles on the surface of silicon." *Thin Solid Films* 584 (2015), 378-381. doi:10.1016/j.tsf.2014.12.001.

**[3]** Li, Qiang, Weichun Zhang, Ding Zhao, and Min Qiu. "Photothermal Enhancement in Core-Shell Structured Plasmonic Nanoparticles." *Plasmonics* 9, no. 3 (2014), 623-630. doi:10.1007/s11468-014-9673-8.

**[4]** Unser, Sarah, Ian Bruzas, Jie He, and Laura Sagle. "Localized Surface Plasmon Resonance Biosensing: Current Challenges and Approaches." *Sensors* 15, no. 7 (2015), 15684-15716. doi:10.3390/s150715684.

**[5]** Anker, Jeffrey N., W. P. Hall, Olga Lyandres, Nilam C. Shah, Jing Zhao, and Richard P. Van Duyne. "Biosensing with plasmonic nanosensors." *Nature Materials* 7, no. 6 (2008), 442-453. doi:10.1038/nmat2162.

**[6]** Wang, Yanfei, Aoune Barhoumi, Rong Tong, Weiping Wang, Tianjiao Ji, Xiaoran Deng, Lele Li, et al. "BaTiO3-core Au-shell nanoparticles for photothermal therapy and bimodal imaging." *Acta Biomaterialia* 72 (2018), 287-294. doi:10.1016/j.actbio.2018.03.029.

**[7]** Bohara, Raghvendra A., and Nanasaheb D. Thorat. *Hybrid Nanostructures for Cancer Theranostics*. Amsterdam: Elsevier, 2018.

**[8]** Ricciardi, Loredana, Lucie Sancey, Giovanna Palermo, Roberto Termine, Antonio De Luca, Elisabeta I. Szerb, Iolinda Aiello, Mauro Ghedini, Giuseppe Strangi, and Massimo La Deda. "Plasmon-mediated cancer phototherapy: the combined effect of thermal and photodynamic processes." *Nanoscale* 9, no. 48 (2017), 19279-19289. doi:10.1039/c7nr05522f.

**[9]** De Sio, Luciano, Tiziana Placido, Roberto Comparelli, M. Lucia Curri, Marinella Striccoli, Nelson Tabiryan, and Timothy J. Bunning. "Next-generation thermo-plasmonic technologies and plasmonic nanoparticles in optoelectronics." *Progress in Quantum Electronics* 41 (2015), 23-70. doi:10.1016/j.pquantelec.2015.03.001.

**[10]** Baffou, Guillaume, Frank Cichos, and Romain Quidant. "Applications and challenges of thermoplasmonics." *Nature Materials* 19, no. 9 (2020), 946-958. doi:10.1038/s41563-020-0740-6.

**[11]** Ghobadi, Turkan G., Amir Ghobadi, Ekmel Ozbay, and Ferdi Karadas. "Strategies for Plasmonic Hot-Electron-Driven Photoelectrochemical Water Splitting." *ChemPhotoChem* 2, no. 3 (2018), 161-182. doi:10.1002/cptc.201700165.

**[12]** Wang, Lu, Morteza Hasanzadeh Kafshgari, and Michel Meunier. "Optical Properties and Applications of Plasmonic-Metal Nanoparticles." *Advanced Functional Materials* 30, no. 51 (2020), 2005400. doi:10.1002/adfm.202005400.

**[13]** Baffou, Guillaume. *Thermoplasmonics*. Cambridge: Cambridge University Press, 2017.

**[14]** Choi, Kyeong W., Do Y. Kim, Seong J. Ye, and O. O. Park. "Shape- and size-controlled synthesis of noble metal nanoparticles." *Advances in materials Research* 3, no. 4 (2014), 199-216. doi:10.12989/amr.2014.3.4.199.

**[15]** Zhang, YuJuan, Rao Huang, XianFang Zhu, LianZhou Wang, and ChenXu Wu. "Synthesis, properties, and optical applications of noble metal nanoparticle-biomolecule conjugates." *Chinese Science Bulletin* 57, no. 2-3 (2012), 238-246. doi:10.1007/s11434-011-4747-x.

**[16]** GEONMONOND, RAFAEL S., ANDERSON G. SILVA, and PEDRO H. CAMARGO. "Controlled synthesis of noble metal nanomaterials: motivation, principles, and opportunities in nanocatalysis." *Anais da Academia Brasileira de Ciências* 90, no. 1 suppl 1 (2018), 719-744. doi:10.1590/0001-3765201820170561.

**[17]** Yang, Zhe, Xuemei Han, Hiang K. Lee, Gia C. Phan-Quang, Charlynn S. Koh, Chee L. Lay, Yih H. Lee, et al. "Shape-dependent thermo-plasmonic effect of nanoporous gold at the nanoscale for ultrasensitive heat-mediated remote actuation." *Nanoscale* 10, no. 34 (2018), 16005-16012. doi:10.1039/c8nr04053b.

**[18]** Tan, Shu F. "Real-Time Imaging of Au–Ag Core-Shell Nanoparticles Formation." *Springer Theses*, 2018, 97-112. doi:10.1007/978-981-10-8803-2_7.

**[19]** Ghosh Chaudhuri, Rajib, and Santanu Paria. "Core/Shell Nanoparticles: Classes, Properties, Synthesis Mechanisms, Characterization, and Applications." *Chemical Reviews* 112, no. 4 (2011), 2373-2433. doi:10.1021/cr100449n.

**[20]** Ni, Weihai, Xiaoshan Kou, Zhi Yang, and Jianfang Wang. "Tailoring Longitudinal Surface Plasmon Wavelengths, Scattering and Absorption Cross Sections of Gold Nanorods." *ACS Nano* 2, no. 4 (2008): 677-686. doi:10.1021/nn7003603.

**[21]** Zakiah W, Ismail W, Vo TP, Goldys EM. Plasmonic enhancement of Rhodamine dye random lasers. doi:10.1088/1054-660X/25/8/085001.

**[22]** Majhi, Sanjit M., Prabhakar Rai, and Yeon-Tae Yu. "Facile Approach to Synthesize Au@ZnO Core–Shell Nanoparticles and Their Application for Highly Sensitive and Selective Gas Sensors." *ACS Applied Materials & Interfaces* 7, no. 18 (2015), 9462-9468. doi:10.1021/acsami.5b00055.

**[23]** Unser, Sarah, Ian Bruzas, Jie He, and Laura Sagle. "Localized Surface Plasmon Resonance Biosensing: Current Challenges and Approaches." *Sensors* 15, no. 7 (2015): 15684-15716. doi:10.3390/s150715684.

**[24]** Duque, Johan, Brayan Madrigal, Henry Riascos, and Yenny Avila. "Colloidal Metal Oxide Nanoparticles Prepared by Laser Ablation Technique and Their Antibacterial Test." *Colloids and Interfaces* 3, no. 1 (2019): 25. doi:10.3390/colloids3010025.

**[25]** Singh, Prashant, Kamlesh Kumari, Vijay K. Vishvakrma, Gopal K. Mehrotra, Ramesh Chandra, Durgesh Kumar, Rajan Patel, and Vaishali V. Shahare. "Metal NPs (Au, Ag, and Cu): Synthesis, Stabilization, and Their Role in Green Chemistry and Drug Delivery." *Green Technologies and Environmental Sustainability*, 2017, 309-337. doi:10.1007/978-3-319-50654-8_14.

**[26]** Nakamura, Shingo, Masahiro Sato, Yoko Sato, Naoko Ando, Tomohiro Takayama, Masanori Fujita, and Masayuki Ishihara. "Synthesis and Application of Silver Nanoparticles (Ag NPs) for the Prevention of Infection in Healthcare Workers." *International Journal of Molecular Sciences* 20, no. 15 (2019), 3620. doi:10.3390/ijms20153620.

**[27]** Loiseau, Alexis, Lu Zhang, David Hu, Michèle Salmain, Yacine Mazouzi, Raphaël Flack, Bo Liedberg, and Souhir Boujday. "Core–Shell Gold/Silver Nanoparticles for Localized Surface Plasmon Resonance-Based Naked-Eye Toxin Biosensing." *ACS Applied Materials & Interfaces* 11, no. 50 (2019), 46462-46471. doi:10.1021/acsami.9b14980.

**[28]** Lereu, A. L., R. H. Farahi, L. Tetard, S. Enoch, T. Thundat, and A. Passian. "Plasmon assisted thermal modulation in nanoparticles." *Optics Express* 21, no. 10 (2013), 12145. doi:10.1364/oe.21.012145.

**[29]** Dai, Han, Ruiqiang Ding, Meicheng Li, Yingfeng Li, Ganghai Yang, Dandan Song, Yue Yu, and Mwenya Trevor. "Abnormal thermal effects on the surface plasmon resonance of Ag nanoparticles on the surface of silicon." *Thin Solid Films* 584 (2015), 378-381. doi:10.1016/j.tsf.2014.12.001.

**[30]** Li, Qiang, Weichun Zhang, Ding Zhao, and Min Qiu. "Photothermal Enhancement in Core-Shell Structured Plasmonic Nanoparticles." *Plasmonics* 9, no. 3 (2014), 623-630. doi:10.1007/s11468-014-9673-8.

**[31]** Norton, Stephen J., and Tuan Vo-Dinh. "Photothermal effects of plasmonic metal nanoparticles in a fluid." *Journal of Applied Physics* 119, no. 8 (2016), 083105. doi:10.1063/1.4942623.

**[32]** Lijun Meng, "Plasmonic Nano-Oven by Concatenation of Multishell Photothermal Enhancement." (n.d.). doi:10.1021/acsnano.7b02426.s001.

**[33]** M. A.Gatea, H. A. Jawad, M. Mosleh, S. M. Hamidi. "Thermoplasmonic response of Au@SiO2 core–shell nanoparticles in deionized water and poly-vinylpyrrolidone matrix." *SYLWAN*, 162(9), (2018).

**[34]** Soomin Han, "Photothermal Cellulose-Patch with Gold-Spiked Silica Microrods Based on Escherichia coli." (n.d.). doi:10.1021/acsomega.8b00639.s002.

**[35]** Et al., Gatea. "Thermoplasmonic of Single Au@SiO2 and SiO2@Au Core Shell Nanoparticles in Deionized Water and Poly-vinylpyrrolidoneMatrix." *Baghdad Science Journal* 16, no. 2 (2019), 0376. doi:10.21123/bsj.16.2.0376.

**[36]** Quintanilla, Marta, Christian Kuttner, Joshua D. Smith, Andreas Seifert, Sara E. Skrabalak, and Luis M. Liz-Marzán. "Heat generation by branched Au/Pd nanocrystals: influence of morphology and composition." *Nanoscale* 11, no. 41 (2019), 19561-19570. doi:10.1039/c9nr05679c.

**[37]** Alkurdi, Ali, Julien Lombard, François Detcheverry, and Samy Merabia. "Enhanced Heat Transfer with Metal-Dielectric Core-Shell Nanoparticles." *Physical Review Applied* 13, no. 3 (2020). doi:10.1103/physrevapplied.13.034036.

**[38]** Kodeary, A. K., Gatea, M. A., Haddawi, S. F., & Hamidi, S. M. (2020). Tunable thermo-piezo-plasmonic effect on core/shell nanoparticles under laser irradiation and external electric field. *Optical and Quantum Electronics*, *52*(2). doi:10.1007/s11082-020-2232-y.

**[39]** Haitao Wang and Ming Li,"Near-Infrared II Thermoplasmonics of Cuprous Selenide Multilayer Nanoshells: The Role of the Plasmonic Core." (n.d.). doi:10.1021/acs.jpclett.1c01081.s001.

**[40]** Penelas, M. J., Gustavo F. Arenas, Fernando Trabadelo, Galo J. Soler-Illia, Sergio E. Moya, Paula C. Angelomé, and Cristina E. Hoppe. "Importance of the Structural and Physicochemical Properties of Silica Nanoshells in the Photothermal Effect of Silica-

Coated Au Nanoparticles Suspensions." *Langmuir* 38, no. 12 (2022), 3876-3886. doi:10.1021/acs.langmuir.2c00127.

**[41]** Prymak, Oleg, Jurij Jakobi, Christoph Rehbock, Matthias Epple, and Stephan Barcikowski. "Crystallographic characterization of laser-generated, polymer-stabilized 4 nm silver-gold alloyed nanoparticles." *Materials Chemistry and Physics 207* (2018), 442-450. doi:10.1016/j.matchemphys.2017.12.080.

**[42]** Nguyen, Thi, Fayna Mammeri, and Souad Ammar. "Iron Oxide and Gold Based Magneto-Plasmonic Nanostructures for Medical Applications: A Review." *Nanomaterials* 8, no. 3 (2018), 149. doi:10.3390/nano8030149.

**[43]** Yeshchenko, Oleg A., Viktor V. Kozachenko, Yuriy F. Liakhov, Anastasiya V. Tomchuk, Michael Haftel, and Anatoliy O. Pinchuk. "Surface plasmon resonance in electrodynamically coupled Au NPs monolayer/dielectric spacer/Al film nanostructure: tuning by variation of spacer thickness." *Materials Research Express* 4, no. 10 (2017), 106401. doi:10.1088/2053-1591/aa8c3a.

**[44]** Ringe, Emilie. "Shapes, Plasmonic Properties, and Reactivity of Magnesium Nanoparticles." *The Journal of Physical Chemistry C* 124, no. 29 (2020), 15665-15679. doi:10.1021/acs.jpcc.0c03871.

**[45]** Sruthi Prasood, U., Satyendra K. Mishra, and Banshi D. Gupta. "Surface Plasmon Resonance Based Fiber Optic Chlorine Gas Sensor Utilizing Ag/Zno Thin Film." *12th International Conference on Fiber Optics and Photonics*, 2014. doi:10.1364/photonics.2014.m4a.52.

**[46]** Khalil, Munawar, Gita Rahmaningsih, Jarnuzi Gunlazuardi, and Aminah Umar. "The Influence of Plasmonic Au Nanoparticle Integration on the Optical Bandgap of Anatase TiO2 Nanoparticles." *International Journal of Technology* 10, no. 4 (2019), 808. doi:10.14716/ijtech.v10i4.2605.

**[47]** Eisa, Wael H., Emad Al-Ashkar, S.M. El-Mossalamy, and Safaa S. Ali. "PVP induce self-seeding process for growth of Au@Ag core@shell nanocomposites." *Chemical Physics Letters* 651 (2016), 28-33. doi:10.1016/j.cplett.2016.03.009.

**[48]** Zhou, Hongjian, Fengming Zou, Kwangnak Koh, and Jaebeom Lee. "Multifunctional Magnetoplasmonic Nanomaterials and Their Biomedical Applications." *Journal of Biomedical Nanotechnology* 10, no. 10 (2014), 2921-2949. doi:10.1166/jbn.2014.1938.

**[49]** Contreras, J.E., E.A. Rodriguez, and J. Taha-Tijerina. "Nanotechnology applications for electrical transformers—A review." *Electric Power Systems Research* 143 (2017): 573-584. doi:10.1016/j.epsr.2016.10.058.

**[50]** Bowman, Diana M., Graeme A. Hodge, and Peter Binks. "Are We Really the Prey? Nanotechnology as Science and Science Fiction." *Bulletin of Science, Technology & Society* 27, no. 6 (2007): 435-445. doi:10.1177/0270467607308282.

**[51]** Korayem, A.H., N. Tourani, M. Zakertabrizi, A.M. Sabziparvar, and W.H. Duan. "A review of dispersion of nanoparticles in cementitious matrices: Nanoparticle geometry perspective." *Construction and Building Materials* 153 (2017): 346-357. doi:10.1016/j.conbuildmat.2017.06.164.

**[52]** Berube, David, Christopher Cummings, Michael Cacciatore, Dietram Scheufele, and Jason Kalin. "Characteristics and classification of nanoparticles: Expert Delphi survey." *Nanotoxicology* 5, no. 2 (2010): 236-243. doi:10.3109/17435390.2010.521633.

**[53]** Sargentelli, Vagner, and Antônio A. Ferreira. "Magnetic Nanoparticles: Co@SiO2, Co@Au and Co@Pt." *Eclética Química Journal* 36, no. 4 (2017): 01. doi:10.26850/1678-4618eqj.v36.4.2011.p01-13.

**[54]** Tiwari, Jitendra N., Rajanish N. Tiwari, and Kwang S. Kim. "Zero-dimensional, one-dimensional, two-dimensional and three-dimensional nanostructured materials for advanced electrochemical energy devices." *Progress in Materials Science* 57, no. 4 (2012): 724-803. doi:10.1016/j.pmatsci.2011.08.003.

**[55]** Piquemal, Jean-Yves, Emmanuel Briot, and Jean-Marie Brégeault. "Preparation of materials in the presence of hydrogen peroxide: from discrete or “zero-dimensional” objects to bulk materials." *Dalton Trans* 42, no. 1 (2013): 29-45. doi:10.1039/c2dt31660a.

**[56]** Yeap, Swee P. "Permanent agglomerates in powdered nanoparticles: Formation and future prospects." *Powder Technology* 323 (2018): 51-59. doi:10.1016/j.powtec.2017.09.042.

**[57]** Gubicza, Jenő. "Defect structure in bulk nanomaterials processed by severe plastic deformation." *Defect Structure in Nanomaterials*, 2012, 41-83. doi:10.1533/9780857096142.41.

**[58]** Zhang, Haijun, Naoki Toshima, Kanako Takasaki, and Mitsutaka Okumura. "Preparation of Agcore/Aushell bimetallic nanoparticles from physical mixtures of Au clusters and Ag ions under dark conditions and their catalytic activity for aerobic glucose oxidation." *Journal of Alloys and Compounds* 586 (2014): 462-468. doi:10.1016/j.jallcom.2013.10.048.

**[59]** Schmidt, Erik, Angelo Vargas, Tamas Mallat, and Alfons Baiker. "Shape-Selective Enantioselective Hydrogenation on Pt Nanoparticles." *Journal of the American Chemical Society* 131, no. 34 (2009): 12358-12367. doi:10.1021/ja9043328.

**[60]** Zhu, Jiahua, Shiyi Zhang, Ke Zhang, Xiaojun Wang, Jimmy W. Mays, Karen L. Wooley, and Darrin J. Pochan. "Disk-cylinder and disk-sphere nanoparticles via a block copolymer blend solution construction." *Nature Communications* 4, no. 1 (2013). doi:10.1038/ncomms3297.

**[61]** Luu, Quocanh N., Joshua M. Doorn, Mary T. Berry, Chaoyang Jiang, Cuikun Lin, and P. S. May. "Preparation and optical properties of silver nanowires and silver-nanowire thin films." *Journal of Colloid and Interface Science* 356, no. 1 (2011): 151-158. doi:10.1016/j.jcis.2010.12.077.

**[62]** Mahala, Pramila, Malkeshkumar Patel, Navneet Gupta, Joondong Kim, and Byung H. Lee. "Schottky junction interfacial properties at high temperature: A case of AgNWs embedded metal oxide/p-Si." *Physica B: Condensed Matter* 537 (2018): 228-235. doi:10.1016/j.physb.2018.02.010.

**[63]** Su, Xiao-Feng, Jian-Biao Chen, Ru-Mei He, Yan Li, Jian Wang, and Cheng-Wei Wang. "The preparation of oxygen-deficient ZnO nanorod arrays and their enhanced field emission." *Materials Science in Semiconductor Processing* 67 (2017): 55-61. doi:10.1016/j.mssp.2017.05.012.

**[64]** Chook, Soon W., Shun X. Yau, Chin H. Chia, Siew X. Chin, and Sarani Zakaria. "Carboxylated-nanoncellulose as a template for the synthesis of silver nanoprism." *Applied Surface Science* 422 (2017): 32-38. doi:10.1016/j.apsusc.2017.05.242.

**[65]** Cathcart, Nicole, Neil Coombs, Ilya Gourevich, and Vladimir Kitaev. "Synthesis and sensing properties of D5hpentagonal silver star nanoparticles." *Nanoscale* 8, no. 43 (2016): 18282-18290. doi:10.1039/c6nr07397b.

**[66]** Biener, Jürgen, Arne Wittstock, Theodore Baumann, Jörg Weissmüller, Marcus Bäumer, and Alex Hamza. "Surface Chemistry in Nanoscale Materials." *Materials* 2, no. 4 (2009): 2404-2428. doi:10.3390/ma2042404.

**[67]** Kumar, Prashant, Alan Robins, Sotiris Vardoulakis, and Rex Britter. "A review of the characteristics of nanoparticles in the urban atmosphere and the prospects for developing regulatory controls." *Atmospheric Environment* 44, no. 39 (2010): 5035-5052. doi:10.1016/j.atmosenv.2010.08.016.

**[68]** Paul, Subir. "Nanomaterials synthesis by electrodeposition techniques for high-energetic electrodes in fuel cell." *Nanomaterials and Energy* 4, no. 1 (2015): 80-89. doi:10.1680/nme.14.00031.

**[69]** Wei, Dacheng, Yunqi Liu, Yu Wang, Hongliang Zhang, Liping Huang, and Gui Yu. "Synthesis of N-Doped Graphene by Chemical Vapor Deposition and Its Electrical Properties." *Nano Letters* 9, no. 5 (2009): 1752-1758. doi:10.1021/nl803279t.

**[70]** Rahman, Ismail A., and Vejayakumaran Padavettan. "Synthesis of Silica Nanoparticles by Sol-Gel: Size-Dependent Properties, Surface Modification, and Applications in Silica-Polymer Nanocomposites—A Review." *Journal of Nanomaterials* 2012 (2012): 1-15. doi:10.1155/2012/132424.

**[71]** Liu, Fei, and Tae S. Seo. "A Controllable Self-Assembly Method for Large-Scale Synthesis of Graphene Sponges and Free-Standing Graphene Films." *Advanced Functional Materials* 20, no. 12 (2010): 1930-1936. doi:10.1002/adfm.201000287.

**[72]** Kim, Myungjoon, Saho Osone, Taesung Kim, Hidenori Higashi, and Takafumi Seto. "Synthesis of Nanoparticles by Laser Ablation: A Review." *KONA Powder and Particle Journal* 34, no. 0 (2017): 80-90. doi:10.14356/kona.2017009.

**[73]** Mélinon, Patrice, Sylvie Begin-Colin, Jean L. Duvail, Fabienne Gauffre, Nathalie H. Boime, Gilles Ledoux, Jérôme Plain, Peter Reiss, Fabien Silly, and Bénédicte Warot-Fonrose. "Engineered inorganic core/shell nanoparticles." *Physics Reports* 543, no. 3 (2014): 163-197. doi:10.1016/j.physrep.2014.05.003.

**[74]** Liu, Rui, and Rodney D. Priestley. "Rational design and fabrication of core–shell nanoparticles through a one-step/pot strategy." *Journal of Materials Chemistry A* 4, no. 18 (2016): 6680-6692. doi:10.1039/c5ta09607c.

**[75]** Hamidi-Asl, Ezat, Freddy Dardenne, Sanaz Pilehvar, Ronny Blust, and Karolien De Wael. "Unique Properties of Core Shell Ag@Au Nanoparticles for the Aptasensing of Bacterial Cells." *Chemosensors* 4, no. 3 (2016): 16. doi:10.3390/chemosensors4030016.

**[76]** Focarete, Maria L., and Anna Tampieri. "Introduction to “Core-shell nanostructures for drug delivery and theranostics: Challenges, strategies, and prospects for novel carrier systems”." *Core-Shell Nanostructures for Drug Delivery and Theranostics*, 2018, 3-5. doi:10.1016/b978-0-08-102198-9.00001-6.

**[77]** Riley, Rachel S., and Emily S. Day. "Gold nanoparticle-mediated photothermal therapy: applications and opportunities for multimodal cancer treatment." *Wiley Interdisciplinary Reviews: Nanomedicine and Nanobiotechnology* 9, no. 4 (2017): e1449. doi:10.1002/wnan.1449.

**[78]** Choe, Minhyeok, Chu-Young Cho, Jae-Phil Shim, Woojin Park, Sung K. Lim, Woong-Ki Hong, Byoung Hun Lee, Dong-Seon Lee, Seong-Ju Park, and Takhee Lee.

"Au nanoparticle-decorated graphene electrodes for GaN-based optoelectronic devices." *Applied Physics Letters* 101, no. 3 (2012): 031115. doi:10.1063/1.4737637.

**[79]** Favier, Isabelle, Daniel Pla, and Montserrat Gómez. "Metal-based nanoparticles dispersed in glycerol: An efficient approach for catalysis." *Catalysis Today* 310 (2018): 98-106. doi:10.1016/j.cattod.2017.06.026.

**[80]** Moos, Rafaela, Ismael L. Graff, Vinicius S. De Oliveira, Wido H. Schreiner, and Arandi G. Bezerra. "Influence of plasmon coupling on the photoluminescence of ZnS/Ag nanoparticles obtained by laser irradiation in liquid." *Optical Materials* 72 (2017): 98-105. doi:10.1016/j.optmat.2017.05.050.

**[81]** Zhang, Tao, Wei Zhang, Min Zheng, and Zhigang Xie. "Near-infrared BODIPY-paclitaxel conjugates assembling organic nanoparticles for chemotherapy and bioimaging." *Journal of Colloid and Interface Science* 514 (2018): 584-591. doi:10.1016/j.jcis.2017.12.074.

**[82]** Razeghi, Manijeh. "Semiconductor p-n and Metal-Semiconductor Junctions." *Technology of Quantum Devices*, 2009, 133-171. doi:10.1007/978-1-4419-1056-1_4.

**[83]** BRILLSON, L. "The structure and properties of metal-semiconductor interfaces." *Surface Science Reports* 2, no. 2 (1982): 123-326. doi:10.1016/0167-5729(82)90001-2.

**[84]** Pintilie, L., and M. Alexe. "Metal-ferroelectric-metal heterostructures with Schottky contacts. I. Influence of the ferroelectric properties." *Journal of Applied Physics* 98, no. 12 (2005): 124103. doi:10.1063/1.2148622.

**[85]** Pintilie, L., I. Boerasu, M. J. Gomes, T. Zhao, R. Ramesh, and M. Alexe. "Metal-ferroelectric-metal structures with Schottky contacts. II. Analysis of the experimental current-voltage and capacitance-voltage characteristics of Pb(Zr,Ti)O3 thin films." *Journal of Applied Physics* 98, no. 12 (2005): 124104. doi:10.1063/1.2148623.

**[86]** Bai, Yu, Zhan J. Wang, Bin He, Jian Z. Cui, and Zhi D. Zhang. "Enhancement of Polarization in Ferroelectric Films via the Incorporation of Gold Nanoparticles." *ACS Omega* 2, no. 12 (2017): 9067-9073. doi:10.1021/acsomega.7b01626.

**[87]** Mahala, Pramila, Malkeshkumar Patel, Navneet Gupta, Joondong Kim, and Byung H. Lee. "Schottky junction interfacial properties at high temperature: A case of AgNWs embedded metal oxide/p-Si." *Physica B: Condensed Matter* 537 (2018): 228-235. doi:10.1016/j.physb.2018.02.010.

**[88]** Tan, Zhengwei, Lanqing Hong, Zhen Fan, Junjiang Tian, Luyong Zhang, Yue Jiang, Zhipeng Hou, et al. "Thinning ferroelectric films for high-efficiency photovoltaics based on the Schottky barrier effect." *NPG Asia Materials* 11, no. 1 (2019). doi:10.1038/s41427-019-0120-3.

**[89]** Fernando Lloret Vieira. "Croissance latérale MPCVD de diamant en homoépitaxie pour dispositifs électroniques de puissance." Ph.D. Thesis, University of Grenoble Alpes, Feb (2018). https://hal.inria.fr/tel-01707012v1

**[90]** Di Bartolomeo, Antonio. "Graphene Schottky diodes: An experimental review of the rectifying graphene/semiconductor heterojunction." *Physics Reports* 606 (2016): 1-58. doi:10.1016/j.physrep.2015.10.003.

**[91]** Wang, Xingfu, Wenbo Peng, Caofeng Pan, and Zhong Lin Wang. "Piezotronics and piezo-phototronics based ona-axis nano/microwires: fundamentals and

applications." *Semiconductor Science and Technology* 32, no. 4 (2017): 043005. doi:10.1088/1361-6641/aa5fcd.

**[92]** Wang, Zhong L., Wenzhuo Wu, and Christian Falconi. "Piezotronics and piezo-phototronics with third-generation semiconductors." *MRS Bulletin* 43, no. 12 (2018): 922-927. doi:10.1557/mrs.2018.263.

**[93]** Zhu, Laipan, and Zhong L. Wang. "Recent Progress in Piezo-Phototronic Effect Enhanced Solar Cells." *Advanced Functional Materials* 29, no. 41 (2018): 1808214. doi:10.1002/adfm.201808214.

**[94]** Boardman, A.D., and A.V. Zayats. "Nonlinear Plasmonics." *Modern Plasmonics*, 2014, 329-347. doi:10.1016/b978-0-444-59526-3.00011-2.

**[95]** Lee, Byoungho, I-Min Lee, Seyoon Kim, Dong-Ho Oh, and Lambertus Hesselink. "Review on subwavelength confinement of light with plasmonics." *Journal of Modern Optics* 57, no. 16 (2010): 1479-1497. doi:10.1080/09500340.2010.506985.

**[96]** Li, Ming, Scott K. Cushing, and Nianqiang Wu. "Plasmon-enhanced optical sensors: a review." *The Analyst* 140, no. 2 (2015): 386-406. doi:10.1039/c4an01079e.

**[97]** Unser, Sarah, Ian Bruzas, Jie He, and Laura Sagle. "Localized Surface Plasmon Resonance Biosensing: Current Challenges and Approaches." *Sensors* 15, no. 7 (2015): 15684-15716. doi:10.3390/s150715684.

**[98]** Duque, Johan, Brayan Madrigal, Henry Riascos, and Yenny Avila. "Colloidal Metal Oxide Nanoparticles Prepared by Laser Ablation Technique and Their Antibacterial Test." *Colloids and Interfaces* 3, no. 1 (2019): 25. doi:10.3390/colloids3010025.

**[99]** Li, Wei, and Jason G. Valentine. "Harvesting the loss: surface plasmon-based hot electron photodetection." *Nanophotonics* 6, no. 1 (2017): 177-191. doi:10.1515/nanoph-2015-0154.

**[100]** Liang, Zhiqiang, Jun Sun, Yueyue Jiang, Lin Jiang, and Xiaodong Chen. "Plasmonic Enhanced Optoelectronic Devices." *Plasmonics* 9, no. 4 (2014): 859-866. doi:10.1007/s11468-014-9682-7.

**[101]** Dobson, Peter J. "Introduction to Metal-nanoparticle Plasmonics, by Matthew Pelton and Garnett W. Bryant." *Contemporary Physics* 55, no. 4 (2014): 352-353. doi:10.1080/00107514.2014.948921.

**[102]** Maier, Stefan A. "Concluding Remarks." *Plasmonics: Fundamentals and Applications*, 2007, 201-201. doi:10.1007/0-387-37825-1_12.

**[103]** Amendola, Vincenzo, Roberto Pilot, Marco Frasconi, Onofrio M. Maragò, and Maria A. Iatì. "Surface plasmon resonance in gold nanoparticles: a review." *Journal of Physics: Condensed Matter* 29, no. 20 (2017): 203002. doi:10.1088/1361-648x/aa60f3.

**[104]** Homola, Jiří. "Surface Plasmon Resonance Sensors for Detection of Chemical and Biological Species." *Chemical Reviews* 108, no. 2 (2008): 462-493. doi:10.1021/cr068107d.

**[105]** Ni, Weihai, Xiaoshan Kou, Zhi Yang, and Jianfang Wang. "Tailoring Longitudinal Surface Plasmon Wavelengths, Scattering and Absorption Cross Sections of Gold Nanorods." *ACS Nano* 2, no. 4 (2008): 677-686. doi:10.1021/nn7003603.

**[106]** Gatea, Maher A., Hussein A. Jawad, and S. M. Hamidi. "Detecting the thermoplasmonic effect using ellipsometry parameters for self-assembled gold nanoparticles within a polydimethylsiloxane matrix." *Applied Physics A* 125, no. 2 (2019). doi:10.1007/s00339-019-2401-7.

**[107]** Hasan, Dihan, Chong P. Ho, Prakash Pitchappa, Bin Yang, Chunsheng Yang, and Chengkuo Lee. "Thermoplasmonic Study of a Triple Band Optical Nanoantenna Strongly Coupled to Mid IR Molecular Mode." *Scientific Reports* 6, no. 1 (2016). doi:10.1038/srep22227.

**[108]** Bretos, Iñigo, Ricardo Jiménez, Monika Tomczyk, Enrique Rodríguez-Castellón, Paula M. Vilarinho, and M. L. Calzada. "Active layers of high-performance lead zirconate titanate at temperatures compatible with silicon nano- and microelectronic devices." *Scientific Reports* 6, no. 1 (2016). doi:10.1038/srep20143.

**[109]** Govorov, Alexander O., and Hugh H. Richardson. "Generating heat with metal nanoparticles." *Nano Today* 2, no. 1 (2007): 30-38. doi:10.1016/s1748-0132(07)70017-8.

**[110]** Wang, Xiandi, Lin Dong, Hanlu Zhang, Ruomeng Yu, Caofeng Pan, and Zhong L. Wang. "Recent Progress in Electronic Skin." *Advanced Science* 2, no. 10 (2015), 1500169. doi:10.1002/advs.201500169.

**[111]** Grua, P., J. P. Morreeuw, H. Bercegol, G. Jonusauskas, and F. Vallée. "Electron kinetics and emission for metal nanoparticles exposed to intense laser pulses." *Physical Review B* 68, no. 3 (2003). doi:10.1103/physrevb.68.035424.

**[112]** Inouye, Hideyuki, Koichiro Tanaka, Ichiro Tanahashi, and Kazuyuki Hirao. "Ultrafast dynamics of nonequilibrium electrons in a gold nanoparticle system." *Physical Review B* 57, no. 18 (1998): 11334-11340. doi:10.1103/physrevb.57.11334.

**[113]** Huang, Xiaohua, Ivan H. El-Sayed, Wei Qian, and Mostafa A. El-Sayed. "Cancer Cells Assemble and Align Gold Nanorods Conjugated to Antibodies to Produce Highly Enhanced, Sharp, and Polarized Surface Raman Spectra: A Potential Cancer Diagnostic Marker." *Nano Letters* 7, no. 6 (2007): 1591-1597. doi:10.1021/nl070472c.

**[114]** Baffou, Guillaume, and Romain Quidant. "Thermo-plasmonics: using metallic nanostructures as nano-sources of heat." *Laser & Photonics Reviews* 7, no. 2 (2012): 171-187. doi:10.1002/lpor.201200003.

**[115]** Baffou, Guillaume, Christian Girard, and Romain Quidant. "Mapping Heat Origin in Plasmonic Structures." *Physical Review Letters* 104, no. 13 (2010). doi:10.1103/physrevlett.104.136805.

**[116]** Donner, Jon S., Guillaume Baffou, David McCloskey, and Romain Quidant. "Plasmon-Assisted Optofluidics." *ACS Nano* 5, no. 7 (2011): 5457-5462. doi:10.1021/nn200590u.

**[117]** Qin, Zhenpeng, and John C. Bischof. "Thermophysical and biological responses of gold nanoparticle laser heating." *Chem. Soc. Rev* 41, no. 3 (2012), 1191-1217. doi:10.1039/c1cs15184c.

**[118]** Ghasemifard, M., S.M. Hosseini, A. Khorsand Zak, and Gh. H. Khorrami. "Microstructural and optical characterization of PZT nanopowder prepared at low temperature." *Physica E: Low-dimensional Systems and Nanostructures* 41, no. 3 (2009), 418-422. doi:10.1016/j.physe.2008.09.017.

**[119]** Palneedi, Haribabu, Jung H. Park, Deepam Maurya, Mahesh Peddigari, Geon-Tae Hwang, Venkateswarlu Annapureddy, Jong-Woo Kim, et al. "Laser Processing of Metal Oxides: Laser Irradiation of Metal Oxide Films and Nanostructures: Applications and Advances (Adv. Mater. 14/2018)." *Advanced Materials* 30, no. 14 (2018), 1870094. doi:10.1002/adma.201870094.

**[120]** Hu, A., P. Peng, H. Alarifi, X. Y. Zhang, J. Y. Guo, Y. Zhou, and W. W. Duley. "Femtosecond laser welded nanostructures and plasmonic devices." *Journal of Laser Applications* 24, no. 4 (2012): 042001. doi:10.2351/1.3695174.

**[121]** Suárez-Gómez, Amaury, and Vladimir Rodríguez-Iglesias. "A 'Universal' Bottom-up Sol-gel Based Synthesis of Pzt (1-x)/x Submicrometric Structures: 1. Dynamic Light Scattering Characterization of Precursor Stability and Aggregation Kinetics." *Materials Research* 18, no. 4 (2015): 798-805. doi:10.1590/1516-1439.004315.

**[122]** Scaramuzza, Stefano, Mirco Zerbetto, and Vincenzo Amendola. "Synthesis of Gold Nanoparticles in Liquid Environment by Laser Ablation with Geometrically Confined Configurations: Insights To Improve Size Control and Productivity." *The Journal of Physical Chemistry C* 120, no. 17 (2016), 9453-9463. doi:10.1021/acs.jpcc.6b00161.

**[123]** Saitow, Ken-ichi. "Nanoparticle Generation by Laser Ablation in Liquid and Supercritical Fluid."*Laser Ablation in Liquids*, 2012, 573-626. doi:10.1201/b11623-13.

**[124]** Amendola, Vincenzo, and Moreno Meneghetti. "Laser ablation synthesis in solution and size manipulation of noble metal nanoparticles." Physical Chemistry Chemical Physics 11, no. 20 (2009), 3805. doi:10.1039/b900654k.

**[125]** Verhoff, B., S. S. Harilal, J. R. Freeman, P. K. Diwakar, and A. Hassanein. "Dynamics of femto- and nanosecond laser ablation plumes investigated using optical emission spectroscopy." *Journal of Applied Physics* 112, no. 9 (2012): 093303. doi:10.1063/1.4764060.

**[126]** Hussein, A. E., P. K. Diwakar, S. S. Harilal, and A. Hassanein. "The role of laser wavelength on plasma generation and expansion of ablation plumes in air." *Journal of Applied Physics* 113, no. 14 (2013): 143305. doi:10.1063/1.4800925.

**[127]** Bashir, Shazia, M. S. Rafique, Chandra S. Nathala, and Wolfgang Husinsky. "Surface and structural modifications of titanium induced by various pulse energies of a femtosecond laser in liquid and dry environment." *Applied Physics A* 114, no. 1 (2013): 243-251. doi:10.1007/s00339-013-8116-2.

**[128]** Wiedwald, Ulf, Luyang Han, Johannes Biskupek, Ute Kaiser, and Paul Ziemann. "Preparation and characterization of supported magnetic nanoparticles prepared by reverse micelles." *Beilstein Journal of Nanotechnology* 1 (2010): 24-47. doi:10.3762/bjnano.1.5.

**[129]** Herbani, Y., Irmaniar, R. S. Nasution, F. Mujtahid, and S. Masse. "Pulse laser ablation of Au, Ag, and Cu metal targets in liquid for nanoparticle production." *Journal of Physics: Conference Series* 985 (2018): 012005. doi:10.1088/1742-6596/985/1/012005.

**[130]** Tan, Mas I., Ahmad F. Omar, Marzaini Rashid, and Uda Hashim. "VIS-NIR spectral and particles distribution of Au, Ag, Cu, Al and Ni nanoparticles synthesized in distilled water using laser ablation." *Results in Physics* 14 (2019): 102497. doi:10.1016/j.rinp.2019.102497.

**[131]** Werner, Daniel, Akihiro Furube, Toshihiro Okamoto, and Shuichi Hashimoto. "Femtosecond Laser-Induced Size Reduction of Aqueous Gold Nanoparticles: In Situ and Pump−Probe Spectroscopy Investigations Revealing Coulomb Explosion." *The Journal of Physical Chemistry C* 115, no. 17 (2011): 8503-8512. doi:10.1021/jp112262u.

**[132]** Wagener, Philipp, Jurij Jakobi, Christoph Rehbock, Venkata S. Chakravadhanula, Claas Thede, Ulf Wiedwald, Mathias Bartsch, Lorenz Kienle, and Stephan Barcikowski. "Solvent-surface interactions control the phase structure in laser-generated iron-gold core-shell nanoparticles." *Scientific Reports* 6, no. 1 (2016). doi:10.1038/srep23352.

**[133]** Reich, Stefan, Patrick Schönfeld, Alexander Letzel, Sebastian Kohsakowski, Margie Olbinado, Bilal Gökce, Stephan Barcikowski, and Anton Plech. "Fluence Threshold Behaviour on Ablation and Bubble Formation in Pulsed Laser Ablation in Liquids." *ChemPhysChem* 18, no. 9 (2017): 1084-1090. doi:10.1002/cphc.201601198.

**[134]** Dell'Aglio, M., R. Gaudiuso, O. De Pascale, and A. De Giacomo. "Mechanisms and processes of pulsed laser ablation in liquids during nanoparticle production." *Applied Surface Science* 348 (2015), 4-9. doi:10.1016/j.apsusc.2015.01.082.

**[135]** Bhatia, Pradeep, Suram S. Verma, and Murari M. Sinha. "Size-dependent Optical Response of Magneto-plasmonic Core-shell Nanoparticles." *Advanced Nano Research* 1, no. 1 (2017), 1-13. doi:10.21467/anr.1.1.1-13.

**[136]** J. H. Nahida, "Spectrophotometric analysis for the UV-irradiated (PMMA)," *Int. J. Basic Appl. Sci*, vol. 12, no. 02, pp. 58–67, 2012.

**[137]** AL Hussainey, Afrah M., Ruaa K. Mahmoud, and Talib M. ALShafie. "Study the Optical and Spectral Properties of the Acridine Dye As an Effective Medium in Dye Lasers." *JOURNAL OF UNIVERSITY OF BABYLON for Pure and Applied Sciences* 26, no. 10 (2018), 167-180. doi:10.29196/jubpas.v26i10.1852.

**[138]** De Sio, Luciano, Tiziana Placido, Roberto Comparelli, M. Lucia Curri, Marinella Striccoli, Nelson Tabiryan, and Timothy J. Bunning. "Next-generation thermo-plasmonic technologies and plasmonic nanoparticles in optoelectronics." *Progress in Quantum Electronics* 41 (2015), 23-70. doi:10.1016/j.pquantelec.2015.03.001.

**[139]** Gatea, et al. "Thermoplasmonic of Single Au@SiO2 and SiO2@Au Core Shell Nanoparticles in Deionized Water and Poly-vinylpyrrolidoneMatrix." *Baghdad Science Journal* 16, no. 2 (2019), 0376. doi:10.21123/bsj.16.2.0376.

**[140]** M. A.Gatea, H. A. Jawad, M. Mosleh, S. M. Hamidi. "Thermoplasmonic response of Au@SiO2 core–shell nanoparticles in deionized water and poly-vinylpyrrolidone matrix." *SYLWAN*, 162(9), (2018).

**[141]** Khlebtsov, N. G. "Optics and biophotonics of nanoparticles with a plasmon resonance." *Quantum Electronics* 38, no. 6 (2008): 504-529. doi:10.1070/qe2008v038n06abeh013829.

**[142]** Li, Er-Ping, and Hong-Son Chu. "Plasmonic Nanoelectronics and Sensing." 2009. doi:10.1017/cbo9781139208802.

**[143]** Hatef, Ali, and Michel Meunier. "Plasma-mediated photothermal effects in ultrafast laser irradiation of gold nanoparticle dimers in water." *Optics Express* 23, no. 3 (2015): 1967. doi:10.1364/oe.23.001967.

**[144]** Johnson, P. B., and R. W. Christy. "Optical Constants of the Noble Metals." *Physical Review B* 6, no. 12 (1972): 4370-4379. doi:10.1103/physrevb.6.4370.

**[145]** Simpson, Sarah, Austin Schelfhout, Chris Golden, and Saeid Vafaei. "Nanofluid Thermal Conductivity and Effective Parameters." *Applied Sciences* 9, no. 1 (2018), 87. doi:10.3390/app9010087.

**[146]** Singh Farwaha, Harnam, Dharmpal Deepak, and Gurinder Singh Brar. "Design and performance of ultrasonic assisted magnetic abrasive finishing combined with electrolytic process set up for machining and finishing of 316L stainless steel." *Materials Today: Proceedings* 33 (2020), 1626-1631. doi:10.1016/j.matpr.2020.06.143.

**[147]** Khosravi Khorashad, Larousse, Lucas V. Besteiro, Zhiming Wang, Jason Valentine, and Alexander O. Govorov. "Localization of Excess Temperature Using Plasmonic Hot Spots in Metal Nanostructures: Combining Nano-Optical Antennas with

the Fano Effect." *The Journal of Physical Chemistry C* 120, no. 24 (2016): 13215-13226. doi:10.1021/acs.jpcc.6b03644.

**[148]** König, Tobias A., Petr A. Ledin, Justin Kerszulis, Mahmoud. A. Mahmoud, Mostafa A. El-Sayed, John R. Reynolds, and Vladimir V. Tsukruk. "Electrically Tunable Plasmonic Behavior of Nanocube–Polymer Nanomaterials Induced by a Redox-Active Electrochromic Polymer." *ACS Nano* 8, no. 6 (2014): 6182-6192. doi:10.1021/nn501601e.

**[149]** Baffou, Guillaume, Romain Quidant, and F. J. García de Abajo. "Nanoscale Control of Optical Heating in Complex Plasmonic Systems." *ACS Nano* 4, no. 2 (2010): 709-716. doi:10.1021/nn901144d.

**[150]** Okkeh, Mohammad, Nora Bloise, Elisa Restivo, Lorenzo De Vita, Piersandro Pallavicini, and Livia Visai. "Gold Nanoparticles: Can They Be the Next Magic Bullet for Multidrug-Resistant Bacteria?" *Nanomaterials* 11, no. 2 (2021), 312. doi:10.3390/nano11020312.

**[151]** Boulais, E., R. Lachaine, A. Hatef, and M. Meunier. "Plasmonics for pulsed-laser cell nanosurgery: Fundamentals and applications." *Journal of Photochemistry and Photobiology C: Photochemistry Reviews* 17 (2013), 26-49. doi:10.1016/j.jphotochemrev.2013.06.001.

**[152]** Tortella, Gonzalo, Olga Rubilar, Paola Fincheira, Joana C. Pieretti, and et al. "Bactericidal and Virucidal Activities of Biogenic Metal-Based Nanoparticles: Advances and Perspectives." *Antibiotics* 10, no. 7 (2021), 783. doi:10.3390/antibiotics10070783.

**[153]** Annesi, Ferdinanda, Alfredo Pane, Maria A. Losso, Alexa Guglielmelli, Fabrizio Lucente, Francesca Petronella, Tiziana Placido, et al. "Thermo-Plasmonic Killing of Escherichia coli TG1 Bacteria." *Materials* 12, no. 9 (2019), 1530. doi:10.3390/ma12091530.

**[154]** Durán, Nelson, Gerson Nakazato, and Amedea B. Seabra. "Antimicrobial activity of biogenic silver nanoparticles, and silver chloride nanoparticles: an overview and comments." *Applied Microbiology and Biotechnology* 100, no. 15 (2016), 6555-6570. doi:10.1007/s00253-016-7657-7.

**[155]** Behera, M., and S. Ram. "Inquiring the mechanism of formation, encapsulation, and stabilization of gold nanoparticles by poly(vinyl pyrrolidone) molecules in 1-butanol." *Applied Nanoscience* 4, no. 2 (2013): 247-254. doi:10.1007/s13204-013-0198-9.

**[156]** Liu, Xiaoli, Yajun Xu, Zhaoqiang Wu, and Hong Chen. "Poly(N-vinylpyrrolidone)-Modified Surfaces for Biomedical Applications." *Macromolecular Bioscience* 13, no. 2 (2012): 147-154. doi:10.1002/mabi.201200269.

**[157]** Mondal, Dibyendu, Md. M. Mollick, Biplab Bhowmick, Dipanwita Maity, Mrinal K. Bain, Dipak Rana, Asis Mukhopadhyay, Kausik Dana, and Dipankar Chattopadhyay. "Effect of poly(vinyl pyrrolidone) on the morphology and physical properties of poly(vinyl alcohol)/sodium montmorillonite nanocomposite films." *Progress in Natural Science: Materials International* 23, no. 6 (2013): 579-587. doi:10.1016/j.pnsc.2013.11.009.

**[158]** Julinova, Marketa, Jan Kupec, Roman Slavik, and Maria Vaskova. "Initiating Biodegradation of Polyvinylpyrrolidone in an Aqueous Aerobic Environment: Technical Note /Zainicjowanie Biodegradacji Poliwinylopirolidonu W Środowisku Wodno-Tlenowym: Notatki Techniczne." *Ecological Chemistry and Engineering S* 20, no. 1 (2013): 199-208. doi:10.2478/eces-2013-0015.

**[159]** Mokhena, T. C., V. Jacobs, and A. S. Luyt. "A review on electrospun bio-based polymers for water treatment." *Express Polymer Letters* 9, no. 10 (2015): 839-880. doi:10.3144/expresspolymlett.2015.79.

**[160]** Hecold, Mateusz, Roma Buczkowska, Aleksandra Mucha, Jakub Grzesiak, Olga Rac-Rumijowska, Helena Teterycz, and Krzysztof Marycz. "The Effect of PEI and PVP-Stabilized Gold Nanoparticles on Equine Platelets Activation: Potential Application in Equine Regenerative Medicine." *Journal of Nanomaterials* 2017 (2017): 1-11. doi:10.1155/2017/8706921.

**[161]** Smith, Louise E., Stephen Rimmer, and Sheila MacNeil. "Examination of the effects of poly(N-vinylpyrrolidinone) hydrogels in direct and indirect contact with cells." *Biomaterials* 27, no. 14 (2006): 2806-2812. doi:10.1016/j.biomaterials.2005.12.018.

**[162]** Buhler, Volker. *Polyvinylpyrrolidone Excipients for Pharmaceuticals: Povidone, Crospovidone and*. Springer, (2010).125-178. doi:10.1007/3-540-27090-6_3.

**[163]** Liu, Xiaoli, Yajun Xu, Zhaoqiang Wu, and Hong Chen. "Poly (N-vinylpyrrolidone)-Modified Surfaces for Biomedical Applications." *Macromolecular Bioscience* 13, no. 2 (2012): 147-154. doi:10.1002/mabi.201200269.

**[164]** Hamidi, Mehrdad, Amir Azadi, and Pedram Rafiei. "Hydrogel nanoparticles in drug delivery." *Advanced Drug Delivery Reviews* 60, no. 15 (2008): 1638-1649. doi:10.1016/j.addr.2008.08.002.

**[165]** Norton, Stephen J., and Tuan Vo-Dinh. "Photothermal effects of plasmonic metal nanoparticles in a fluid." *Journal of Applied Physics* 119, no. 8 (2016), 083105. doi:10.1063/1.4942623.

**[166]** Mani, M., S. Pavithra, K. Mohanraj, and et al. "Studies on the spectrometric analysis of metallic silver nanoparticles (Ag NPs) using Basella alba leaf for the antibacterial activities." *Environmental Research* 199 (2021), 111274. doi:10.1016/j.envres.2021.111274.

**[167]** Folorunso, Aderonke, Sunday Akintelu, and et al. "Biosynthesis, characterization and antimicrobial activity of gold nanoparticles from leaf extracts of Annona muricata." *Journal of Nanostructure in Chemistry* 9, no. 2 (2019), 111-117. doi:10.1007/s40097-019-0301-1.

**[168]** Sathiyaraj, Sivaji, Gunasekaran Suriyakala, Arumugam Dhanesh Gandhi, and et al. "Biosynthesis, characterization, and antibacterial activity of gold nanoparticles." *Journal of Infection and Public Health* 14, no. 12 (2021), 1842-1847. doi:10.1016/j.jiph.2021.10.007.

**[169]** Mirshafieyan, Seyed S., Ting S. Luk, and Junpeng Guo. "Zeroth order Fabry-Perot resonance enabled ultra-thin perfect light absorber using percolation aluminum and silicon nanofilms." *Optical Materials Express* 6, no. 4 (2016), 1032. doi:10.1364/ome.6.001032.

**[170]** Et al., Gatea. "Thermoplasmonic of Single Au@SiO2 and SiO2@Au Core Shell Nanoparticles in Deionized Water and Poly-vinylpyrrolidoneMatrix." *Baghdad Science Journal* 16, no. 2 (2019), 0376. doi:10.21123/bsj.16.2.0376.

**[171]** Kodeary, A.K., S.M. Hamidi, and R. Moradlou. "Voltage controlled properties of piezo-magneto-plasmonic core/shell nanoparticles." *Nano-Structures & Nano-Objects* 21 (2020), 100415. doi:10.1016/j.nanoso.2019.100415.

**[172]** AL-Ibraheemi, S., Al-Ibraheemi, F. A., & Gatea, M. A. (2019). Nonlinear optical properties of gold-silica nano-particles. *2019 2nd International Conference on*

*Engineering Technology and its Applications (IICETA)*. doi:10.1109/iiceta47481.2019.9012989.

**[173]** Mbarak, H., Kodeary, A., Hamidi, S., Mohajarani, E., & Zaatar, Y. (2019). Control of nonlinear refractive index of AuNPs doped with nematic liquid crystal under external electric field. *Optik*, *198*, 163299. doi:10.1016/j.ijleo.2019.163299.

**[174]** Kodeary, A. K., and S. M. Hamidi. "Tunable Piezophotonic Effect on Core-Shell Nanoparticles Prepared by Laser Ablation in Liquids under External Voltage." *Journal of Nanotechnology* 2019 (2019), 1-11. doi:10.1155/2019/6046079.

**[175]** Kodeary, A.K., S.M. Hamidi, and R. Moradlou. "Voltage controlled properties of piezo-magneto-plasmonic core/shell nanoparticles." *Nano-Structures & Nano-Objects* 21 (2020), 100415. doi:10.1016/j.nanoso.2019.100415.

**[176]** Majhi, S. M., Rai, P., & Yu, Y. (2015). Facile approach to synthesize Au@ZnO core–shell nanoparticles and their application for highly sensitive and selective gas sensors. *ACS Applied Materials & Interfaces*, *7*(18), 9462-9468. doi:10.1021/acsami.5b00055.

**[177]** Baffou, Guillaume. *Thermoplasmonics*. Cambridge: Cambridge University Press, 2017.

**[178]** Kodeary, A. K., Gatea, M. A., Haddawi, S. F., & Hamidi, S. M. (2020). Tunable thermo-piezo-plasmonic effect on core/shell nanoparticles under laser irradiation and external electric field. *Optical and Quantum Electronics*, *52*(2). doi:10.1007/s11082-020-2232-y.

**[179]** Rashidi-Huyeh, M., & Palpant, B. (2004). Thermal response of nanocomposite materials under pulsed laser excitation. *Journal of Applied Physics*, *96*(8), 4475-4482. doi:10.1063/1.1794894.

**[180]** Chen, F., Wu, W., Li, S., & Klein, A. (2014). Energy band alignment at ferroelectric/electrode interface determined by photoelectron spectroscopy. *Chinese Physics B*, *23*(1), 017702. doi:10.1088/1674-1056/23/1/017702.

**[181]** Magnozzi, Michele, Yannic Brasse, Tobias A. König, Francesco Bisio, Eva Bittrich, Andreas Fery, and Maurizio Canepa. "Plasmonics of Au/Polymer Core/Shell Nanocomposites for Thermoresponsive Hybrid Metasurfaces." *ACS Applied Nano Materials* 3, no. 2 (2020): 1674-1682. doi:10.1021/acsanm.9b02403.

**[182]** Chen, Feng, Wen-Bin Wu, Shun-Yi Li, and Andreas Klein. "Energy band alignment at ferroelectric/electrode interface determined by photoelectron spectroscopy." *Chinese Physics B* 23, no. 1 (2014), 017702. doi:10.1088/1674-1056/23/1/017702.

**[183]** Carponcin, Delphine, Eric Dantras, Lydia Laffont, Jany Dandurand, Gwenaëlle Aridon, Franck Levallois, Laurent Cadiergues, and Colette Lacabanne. "Integrated piezoelectric function in a high thermostable thermoplastic PZT/PEEK composite." *Journal of Non-Crystalline Solids* 388 (2014): 32-36. doi:10.1016/j.jnoncrysol.2014.01.020.

**[184]** P, Gowdhaman, Antonyraj K, and Annamalai V. "An effective approach on physical and dielectric properties of PZT-PVDF composites." *International Journal of Advances in Scientific Research* 1, no. 8 (2015): 322. doi:10.7439/ijasr.v1i8.2511.

# الملخص

ركزت الدراسة التجريبية الحالية على توليف وتقييم الخصائص البلازمونية الحرارية للجسيمات النانوية القلب/الغلاف (Core/Shell NPs) والجسيمات النانوية القلب/متعدد الغلاف (Core/Multi-Shell NPs) المحضرة بطريقة الاستئصال بالليزر النبضي في السوائل ( ليزر النانوثانية يعمل بالطول الموجي 1064 نانومتر) ، لإدخال نوع جديد من الهياكل النانوية الهجينة القابلة للاستخدام في تطبيقات الطب الحيوي وتطبيقات الضوئيات البصرية.

بالنسبة للهياكل النانوية الهجينة ، تم استخدام الذهب (Au) والفضة (Ag) كشريك للسيليكون (Si) في الجزء البلازموني الحراري، تتكون الهياكل النانوية الهجينة متعددة الأصداف من شطيرة (ذهبيه - فضيه) و(فضيه - ذهبيه) مع غلاف من السيليكون في ما بينهما.

تم قياس الامتصاص البصري للعينات باستخدام مقياس (UV–Vis spectrophotometer) ، وتم رصد شدة وموضع البلازمون السطحي اعتمادًا على الخصائص العزلية للعينات. بالإضافة إلى ذلك ، تم دراسة الخصائص البلازمونيه الحرارية من خلال مراقبة زيادة درجة الحرارة الموضعيه للعينات بشكل تجريبي بأستخدام كاميرا حراريه عند اضاءة العينات بأشعة الليزر ذات الأطوال الموجية المختلفة (532 ، 405 نانومتر). وكذلك تم اختبار الجسيمات النانوية القلب/متعدد الغلاف لتثبيط نشاط بكتيريا الاشريكية القالونية (E-coli) تحت إشعاع الليزر.

بالإضافة إلى ذلك ، تم محاكاة الخواص البصرية والتأثيرات الحرارية البلازمية وتوزيع الشحنة الكهربائية الموضعية السطحية للعينات باستخدام برنامج محاكاه نظريًا كومسل متعدد الفيزياء (COMSOL- Multiphysics ) بأحجام قلب وسمك غلاف مختلف بواسطة طريقة العناصر المحدودة تحت إشعاع الليزر باطوال موجية مختلفة (532 ، 405 نانومتر).

كشفت النتائج عن خصائص بصرية بلازمونية حرارية قابلة للضبط و التعديل بشكل واضح من خلال التحكم في بنية الجسيمات النانوية القلب/الغلاف. بالإضافة إلى ذلك ، تُظهر النتائج أنه يمكن الحصول على سيطرة وضبط شديد في رنين البلازمون السطحي، وكذلك الحصول على تأثيرات بلازمونيه حراريه محسنه بشكل كبير من حيث ارتفاع درجة الحرارة بالاعتماد على تأثير الليزر.

تظهر النتائج أن الجسيمات النانوية القلب/متعدد الغلاف تنتج حرارة أكثر من الجسيمات القلب/الغلاف، وكذلك حرارة أكثر من الجسيمات النانوية الفردية. تم الحصول على ارتفاع درجة الحرارة $8.2C^{o}$ لـعينة Ag@Si@Au NPs و $7.4C^{o}$ لـعينة Au@Si@Ag NPs تحت اشعاع الليزر المستمر باطوال موجية (405 ، 532 نانومتر) على التوالي.

كذلك أثبتت التجارب أن النظام النانوي المقترح حقق كفاءة قتل عالية ضد بكتيريا الاشريكية القالونية تحت إضاءة الليزر المستمر (405،532 نانومتر) ، وكان قطر مناطق التثبيط 6-8 ملم لعينات الجسيمات النانوية القلب/متعدد الغلاف.

اثبتت نتائج المحاكاة النظرية وجود تطابق جيد مع النتائج التجريبية مما يساعد على فهم الظواهر الفيزيائية بشكل اوضح, ويمكن تحسين النتائج اعتمادًا على الحجم والشكل وتركيب الجسيمات النانوية وكذلك الوسائط المغمورة بها. يمكن ان نستنتج، ان برنامج المحاكاة يمكنه التنبؤ بالنتائج التجريبية بدقة عالية.

اظهرت النتائج إمكانية استخدام الجسيمات النانوية القلب/متعدد الغلاف كمصادر حرارة فعالة في العديد من التطبيقات، لا سيما في تطهير وتعقيم المعدات الطبية.

**جمهورية العراق**

**وزارة التعليم العالي والبحث العلمي**

**جامعة بابل / كلية العلوم للبنات**

**قسم فيزياء الليزر**

# الخصائص البلازمونية الحرارية لتراكيب نانوية هجينة

**رسالة مقدمة الى**

كلية العلوم للبنات - جامعة بابل

وهي كجزء من متطلبات نيل درجة الماجستير في العلوم - فيزياء الليزر

من قبل

**ندى عباس محمد**

اشراف

**أ.د. وجيهة عبد الدايم زوبع**

**م.د. أحمد كاظم خضيري**

2022 م

1444 هـ